# Doctoral Dissertation

## Studies on Photocatalytic Activities and Charge Transfer Dynamics of Solar-Driven Photocatalysts for Hydrogen Production

**RUAN DAMING**

**January 2020**

**Division of Applied Chemistry,**
**Graduate School of Engineering,**
**Osaka University**

# Preface

The studies presented in this thesis were carried out under the direction of Professor Tetsuro Majima and Associate Professor Mamoru Fujitsuka, the Institute of Scientific and Industrial Research (SANKEN), Osaka University from October, 2016 to March, 2020.

The object of this thesis is the development of visible (Vis) and near infrared (NIR) light driven photocatalysts for photocatalytic $H_2$ production and study on photogenerated charge carrier dynamics in photocatalysis. The aim of this research is to resolve the problems about low photocatalytic efficiency of g-$C_3N_4$ for $H_2$ production by increasing the surface area and introduction of defects, application of plasmonic Au nanostructure-based photocatalyst under NIR light irradiation, and exploration of earth-abundant high-performance cocatalyst instead of noble metals.

The author hopes that the results and conclusions presented in this thesis contribute to in-depth understanding of the relation between charge carrier dynamics and photocatalytic activities in photocatalysis and further improvement of quantum efficiency of photocatalysts for practical application.

RUAN DAMING

Department of Applied Chemistry
Graduate School of Engineering
Osaka University
January 2020

# Contents

# General Introduction

Over the past few decades, rapid industrialization accompanied by excessive consumption of fossil fuels causes energy depletion and serious environmental pollutions. Reflecting the energy demand, an exploration of renewable and environmentally friendly energy sources is highly imperative. Hydrogen ($H_2$) is considered as an ideal and clean energy due to its high energy density and the no harmful combustion product, $H_2O$. Since the first report of $H_2$ production from photoelectrochemical water splitting on n-type $TiO_2$ electrode by Fujishima and Honda in 1972,[1] photocatalysis using semiconductors has attracted great interest as a promising technology for conversion of solar energy into chemical energy like hydrogen or hydrocarbon,[2] $CO_2$ reduction to energy fuels,[3] pollutants degradation,[4] organic transformation,[5] disinfection of bacteria,[6] etc. So far, great progress has been achieved in the research of water splitting into $H_2$ and $O_2$.[7-10] As shown in equation 1, water splitting is well known as an uphill chemical reaction accompanied by a large change in the Gibbs free energy.

$$2H_2O \longrightarrow 2H_2 + O_2 \qquad \Delta G^0 = 237 \text{ kJ mol}^{-1} \tag{1}$$

Fig.1 illustrates the main processes of photocatalytic water splitting on a semiconductor photocatalyst. Under irradiation of light with energy greater than the band gap ($E_g$) of the semiconductor, the electrons ($e^-$) of the valance band (VB) are excited into the conduction band (CB) whereas the holes ($h^+$) remain in VB. Then, the photogenerated electrons and holes migrate toward the surface of the semiconductor and subsequently reduce and oxidize the water molecules adsorbed on the semiconductor surface to generate $H_2$ and $O_2$, respectively. Meanwhile, the electrons and holes can also recombine, resulting in low photocatalytic activities. Notably, to overcome the thermodynamic barriers required for these two redox reactions, the bottom of CB for the semiconductor must be located at a more negative potential than $H^+/H_2$ (0-0.059 pH, V vs. NHE) and the top of VB should be more positive than $O_2/H_2O$ (1.23-0.059 pH, V vs. NHE).[11] The recombination rate of photogenerated electrons and holes is very fast ($10^{-12}$ to $10^{-11}$ s), while the trapping rate of charge carriers to the surface is relatively slow ($10^{-7}$ to $10^{-9}$ s).[12] In order to suppress the charge recombination and promote the charge transfer to the surface active sites to increase the photocatalytic efficiency for water splitting, cocatalyts are generally employed. A cocatalyst may play

two major roles in photocatalytic reactions: 1) extracting the photogenerated charge carriers to suppress the recombination of electrons and holes; 2) providing reaction active sites.[13]

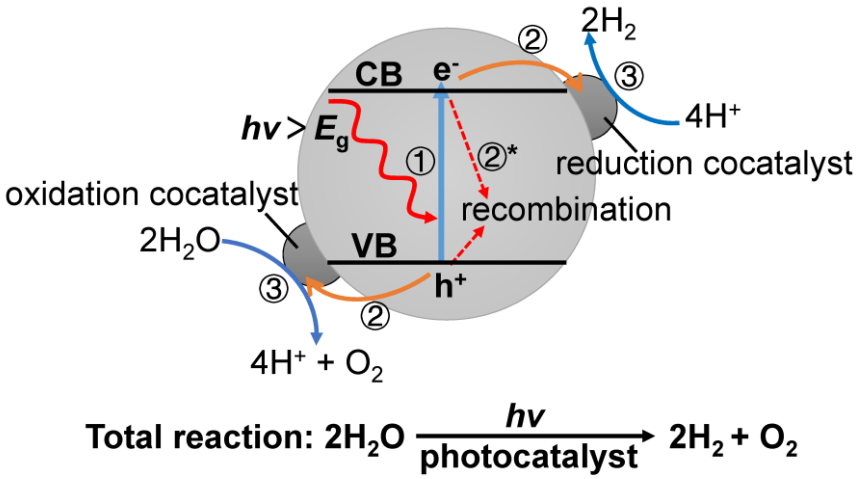


**Figure 1.** Schematic diagram for the main processes of water splitting on a semiconductor photocatalyst.

Because $TiO_2$ has the merits of high chemical stability, low-cost, nontoxicity, and commercial availability, $TiO_2$-based materials have been widely studied.[14-17] However, $TiO_2$ can only absorb UV light which accounts for ca. 5% in solar spectrum because of the large bandgap ($E_g$ = 3.2 eV). Up to now, various kinds of Vis-light-driven semiconductors have been investigated as photocatalysts, such as graphitic carbon nitride (g-$C_3N_4$).[18-21] Since the first report on g-$C_3N_4$ in photocatalytic $H_2$ production in 2009,[22] it has been widely studied due to photocatalytic activities in $H_2$ production,[23] water oxidation,[24] $CO_2$ reduction,[25] pollutants degradation,[26] and organic synthesis.[27] However, the photocatalytic performance of g-$C_3N_4$ is not sufficient because of low surface area and fast recombination of charge carriers.

In majority of photocatalytic reactions, near-infrared (NIR) light, which accounts for ca. 44% of the solar spectrum, remains unutilized. Many efforts have been invested to develop NIR-light-driven materials in recent years.[28] Plasmonic Au nanosturctures are receiving increasing attention as photocatalysts due to their large absorption in Vis and NIR region, resulting from surface plasmon resonance (SPR). Surface plasmons decay either radiatively or non-radiatively through transferring the energy to generate hot electrons which can be used to drive energetically demanding chemcial reactions.[29, 30] The SPR effect is greatly influenced by their size and nanostructures, such as nanospheres, nanorods, and nanoprisms. The research for Au nanosturctures that can

harvest NIR light is still full of challenge.

Bare photocatalysts often suffer from poor activity due to rapid charge recombination and a small amount of active sites. Therefore, semiconductor photocatalysts are usually combined with cocatalysts, such as Pt-group (e.g., Pt, Pd, and Rh, etc.) noble metals with high work function and low overpotential for proton reduction. For practical applications, an exploration of low-cost and high-performance cocatalysts to replace expensive and rare noble metals for photocatalytic $H_2$ production is highly desirable. Many efforts have been made to develop nobal-metal-free cocatalysts for $H_2$ production.[31]

In this dissertation, a series of Vis-NIR-driven photocatalysts for $H_2$ production were investigated by focusing on the charge carrier dynamics.

Contents of each chapter are shown as below.

In Chapter 1, defects rich g-$C_3N_4$ nanosheets with mesoporous structure and high surface area were prepared by using a mixture of melamine (M) and urea (U) as precursors for photocatalytic $H_2$ production. The use of urea increased the surface area and introduced the defects of nitrogen vacancies acting as electron trapping states in g-$C_3N_4$. The obtained g-$C_3N_4$-$M_1U_2$ (1 and 2 denote the weight ratio of M and U, respectively) exhibited the photocatalytic $H_2$ production rate of 3.1 mmol $g^{-1}$ $h^{-1}$ under $\lambda \geq 400$ nm light irradiation and apparent quantum efficiency (AQE) of 74% at $\lambda = 400$ nm. Single-particle photoluminescence (PL) showed longer lifetime of charge carriers in g-$C_3N_4$-$M_1U_2$ than that in g-$C_3N_4$-M. Femtosecond time-resolved diffuse reflectance measurement was performed to reveal trapping processes of photogenerated electrons in g-$C_3N_4$-$M_xU_y$.

In Chapter 2, Au triangular nanoprisms (TNPs) loaded on g-$C_3N_4$ nanosheets were synthesized to show photocatalytic $H_2$ production under NIR light ($\lambda \geq 780$ nm) irradiation. 2.0 wt% Au TNP/g-$C_3N_4$ exhibited apparent photocatalytic $H_2$ production activity up to 53.4 mmol $g^{-1}$ $h^{-1}$. Finite-difference time-domain (FDTD) simulations confirm a stronger electromagnetic field in Au TNP/g-$C_3N_4$ than in Au TNPs which would increase the density of plasmon-induced hot electrons and facilitate interfacial electron transfer (ET) from Au TNPs to g-$C_3N_4$. Time-resolved transient absorption measurements reveal the dynamics of plasmon-induced hot electrons in Au TNP/g-$C_3N_4$ hybrid which showed longer lifetimes of charge carriers than that of Au TNPs.

In Chapter 3, highly exfoliated 2D $Mo_2C$ nanosheets with a thickness of 20 nm

($Mo_2C$) were prepared by liquid-phase ultrasonic exfoliation for the first time. $Mo_2C$ was hybridized on CdS nanoparticles with a diameter of 10 nm (CdS) to be the composite $Mo_2C$/CdS for photocatalytic $H_2$ production under Vis light irradiation. Under optimized experimental conditions, $Mo_2C$/CdS exhibited a remarkable $H_2$ production rate of 7.7 mmol $g^{-1}$ $h^{-1}$ which is 6-, 16-, and 4-folds as high as those for bulk $Mo_2C$/CdS, pure CdS, and Pt/CdS, respectively. The AQE of 3 wt% $Mo_2C$/CdS is 86% at 460 nm. The enhanced activity is attributed to the rapid transfer of photogenerated electrons from CdS to $Mo_2C$ at the heterointerface and shortened migration distance of the electrons to the active sites in $Mo_2C$ as well as the presence of more active sites of $Mo_2C$ than bulk $Mo_2C$. Photoluminescence, photoelectrochemical measurements, and femtosecond time-resolved diffuse reflectance spectroscopy results demonstrated the efficient charge separation and injection in $Mo_2C$/CdS.

# References


1. A. Fujishima and K. Honda, *Nature*, 1972, **238**, 37.
2. T. Hisatomi, J. Kubota and K. Domen, *Chem. Soc. Rev.*, 2014, **43**, 7520-7535.
3. K. Li, B. Peng and T. Peng, *ACS Catal.*, 2016, **6**, 7485-7527.
4. R. Das, C. D. Vecitis, A. Schulze, B. Cao, A. F. Ismail, X. Lu, J. Chen and S. Ramakrishna, *Chem. Soc. Rev.*, 2017, **46**, 6946-7020.
5. J. Kou, C. Lu, J. Wang, Y. Chen, Z. Xu and R. S. Varma, *Chem. Rev.*, 2017, **117**, 1445-1514.
6. S. Kang, W. Huang, L. Zhang, M. He, S. Xu, D. Sun and X. Jiang, *ACS Appl. Mater. Interfaces*, 2018, **10**, 13796-13804.
7. Z. Wang, C. Li and K. Domen, *Chem. Soc. Rev.*, 2019, **48**, 2109-2125.
8. Y. Yan, B. Y. Xia, B. Zhao and X. Wang, *J. Mater. Chem. A*, 2016, **4**, 17587-17603.
9. T. Takata and K. Domen, *ACS Energy Lett.*, 2019, **4**, 542-549.
10. K. Maeda, *ACS Catal.*, 2013, **3**, 1486-1503.
11. S. Chen, T. Takata and K. Domen, *Nat. Rev. Mater.*, 2017, **2**.
12. J. Schneider, M. Matsuoka, M. Takeuchi, J. Zhang, Y. Horiuchi, M. Anpo and D.

W. Bahnemann, *Chem. Rev.*, 2014, **114**, 9919-9986.

13. A. Meng, L. Zhang, B. Cheng and J. Yu, *Adv. Mater.*, 2019, **31**, 1807660.
14. H. Xu, S. Ouyang, L. Liu, P. Reunchan, N. Umezawa and J. Ye, *J. Mater. Chem. A*, 2014, **2**, 12642-12661.
15. Y. Ma, X. Wang, Y. Jia, X. Chen, H. Han and C. Li, *Chem. Rev.*, 2014, **114**, 9987-10043.
16. J. B. Joo, M. Dahl, N. Li, F. Zaera and Y. Yin, *Energy Environ. Sci.*, 2013, **6**, 2082-2092.
17. C. Luo, X. Ren, Z. Dai, Y. Zhang, X. Qi and C. Pan, *ACS Appl. Mater. Interfaces*, 2017, **9**, 23265-23286.
18. S. J. A. Moniz, S. A. Shevlin, D. J. Martin, Z. X. Guo and J. Tang, *Energy Environ. Sci.*, 2015, **8**, 731-759.
19. W. J. Ong, L. L. Tan, Y. H. Ng, S. T. Yong and S. P. Chai, *Chem. Rev.*, 2016, **116**, 7159-7329.
20. X. Wang, S. Blechert and M. Antonietti, *ACS Catal.*, 2012, **2**, 1596-1606.
21. G. Liao, Y. Gong, L. Zhang, H. Gao, G.-J. Yang and B. Fang, *Energy Environ. Sci.*, 2019, **12**, 2080-2147.
22. X. Wang, K. Maeda, A. Thomas, K. Takanabe, G. Xin, J. M. Carlsson, K. Domen and M. Antonietti, *Nat. Mater.*, 2009, **8**, 76-80.
23. Q. Han, B. Wang, J. Gao, Z. Cheng, Y. Zhao, Z. Zhang and L. Qu, *ACS Nano*, 2016, **10**, 2745-2751.
24. M. Tahir, N. Mahmood, L. Pan, Z. F. Huang, Z. Lv, J. Zhang, F. K. Butt, G. Shen, X. Zhang, S. X. Dou and J. J. Zou, *J. Mater. Chem. A*, 2016, **4**, 12940-12946.
25. P. Huang, J. Huang, S. A. Pantovich, A. D. Carl, T. G. Fenton, C. A. Caputo, R. L. Grimm, A. I. Frenkel and G. Li, *J. Am. Chem. Soc.*, 2018, **140**, 16042-16047.
26. G. Dong and L. Zhang, *J. Phys. Chem. C*, 2013, **117**, 4062-4068.
27. S. Tian, Z. Wang, W. Gong, W. Chen, Q. Feng, Q. Xu, C. Chen, C. Chen, Q. Peng, L. Gu, H. Zhao, P. Hu, D. Wang and Y. Li, *J. Am. Chem. Soc.*, 2018, **140**, 11161-11164.

28. L. Wang, X. Xu, Q. Cheng, S. X. Dou and Y. Du, *Small*, 2019, 1904107.
29. C. Clavero, *Nat. Photonics*, 2014, **8**, 95-103.
30. R. Sundararaman, P. Narang, A. S. Jermyn, W. A. Goddard III and H. A. Atwater, *Nat. Commun.*, 2014, **5**, 5788.
31. X. Zou and Y. Zhang, *Chem. Soc. Rev.* 2015, **44**, 5148-5180.

# Chapter 1. Defects Rich g-$C_3N_4$ with Mesoporous Structure for Efficient Photocatalytic $H_2$ Production under Visible Light Irradiation

## 1. Introduction

Since the discovery of Fujishima-Honda effect in 1970s,[1] water splitting using solar energy has been considered as a promising strategy for converting solar energy into chemical energy in the form of clean and renewable hydrogen fuel. In particular, semiconductors which can be excited by Vis light for photocatalytic $H_2$ production have attracted much attention. Among the various Vis-light-response photocatalysts, graphitic carbon nitride (g-$C_3N_4$), composed of carbon and nitrogen, the earth abundant elements, is one of the suitable candidates as a photocatalyst because of the low cost, good stability, and excellent optical and electronic properties.[2-8] g-$C_3N_4$ possesses a bandgap around 2.7 eV corresponding to the absorption threshold at 460 nm, and conduction band potential at -1.1 V vs NHE which is enough for water reduction. So far, many efforts have been done for g-$C_3N_4$ to improve the photocatalytic activity of $H_2$ production.[9-12]

However, the fast recombination of charge carriers and low surface area results in low photocatalytic efficiency, which restricts the practical applications of g-$C_3N_4$. Up to now, numerous approaches have been employed to improve the photocatalytic performance of g-$C_3N_4$.[7, 13-16] Various preparation methods have been used to introduce the defects for trapping photogenerated electrons and decreasing the charge recombination.[17, 18] For example, Chen's group synthesized defects rich g-$C_3N_4$ by introducing $H_2$ gas in the thermal condensation process.[18] In general, g-$C_3N_4$ is prepared by thermal condensation of thiourea, melamine (M), urea (U), and dicyandiamide. However, the condensation of the precursors gives rise to the samples with a low surface area (~10 $m^2$ $g^{-1}$) and lack of mesoporous strucure.[19] It is well known that large surface area is important in photocatalytic reactions by exposing more active sites. To date, widely used technique for the preparation of mesoporous g-$C_3N_4$ with a large surface area is based on template methods, such as soft template (self-assembly)[20] and hard template (nanocasting).[21] However, the preparation of mesoporous g-$C_3N_4$ with a large surface area is not established.

On the other hand, previous works showed that several kinds of g-$C_3N_4$ have been

prepared by using a mixture of precursors.[22-24] For example, Ho's group synthesized g-$C_3N_4$/g-$C_3N_4$ isotype heterojunction by using U and thiourea as precursors.[25] Herein, we report efficient photocatalytic $H_2$ production using g-$C_3N_4$ with defects of nitrogen vacancies, high surface, area and mesoporous structure. g-$C_3N_4$-$M_xU_y$ (*x* and *y* denote the mass ratios of M to U, respectively) with large surface area and defects were synthesized from mixture precursors of M and U. The synthesis conditions were optimized by adjusting the ratios of M and U and the calcination temperatures. We found that increasing the amount of U increased the number of defects and surface area (Scheme 1). U disappeared during the formation of g-$C_3N_4$-$M_xU_y$. The optimum $H_2$ production rate of g-$C_3N_4$-$M_1U_2$ was 3.1 mmol $g^{-1}$ $h^{-1}$ under $\lambda \geq 400$ nm light irradiation, and the AQE was 74% at $\lambda$ = 400 nm. The enhancement of photocatalytic activity is due to increased content of defects which facilitate trapping photogenerated electrons and high surface area in g-$C_3N_4$-$M_1U_2$. The single-particle PL measurement and time-resolved diffuse reflectance spectroscopic measurement were carried out to clarify the charge separation efficiency and charge dynamics in photoexcited g-$C_3N_4$-$M_xU_y$.

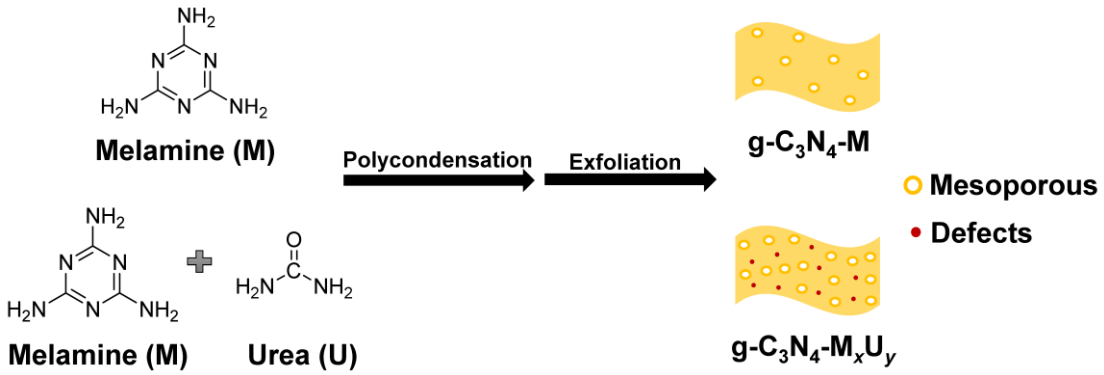


**Scheme 1.** Preparation of g-$C_3N_4$-M and g-$C_3N_4$-$M_xU_y$ using melamine (M) or a mixture of M and U as the precursors.

## 2. Experimental Section

**Materials.** The bulk g-$C_3N_4$-$M_xU_y$, *x* and *y* mean the mass ratios of M to U, were prepared by thermal condensation as follows: 2 g of mixture of precursors including M and U with *x*:*y* from 2:1 to 1:3 were added into 20 mL ethanol. The suspension was kept stirring at ambient temperature for 0.5 h, then the ethanol was removed by a rotary evaporation apparatus. Subsequently, the mixture powder was put into an alumina crucible with a cover and heated to 773 K for 2 h at a heating rate of 2 K $min^{-1}$ in a muffle furnace, then rising the temperature to 793 K at the same heating rate for another

2 h. The obtained product was collected and grounded into powder for further use.

The exfoliation of g-$C_3N_4$-$M_xU_y$ from bulk into nanosheet structure were carried out as follows: 0.45 g of bulk g-$C_3N_4$-$M_xU_y$ was uniformly dispersed into an alumina ark with dimension of 50×30×10 mm to make sufficient contact between bulk g-$C_3N_4$-$M_xU_y$ and air, and then was heated to 773 K in an open system at a heating rate of 2 K $min^{-1}$ for 3 h in a muffle furnace to form g-$C_3N_4$-$M_xU_y$ with nanosheet structure

For comparison, g-$C_3N_4$-M and g-$C_3N_4$-U were also prepared by using 2 g of M and 2 g of U under the same calcination conditions, respectively. The alumina crucible loaded with 2 g of U was found to be empty after the first step calcination. No g-$C_3N_4$-U was obtained from the same preparation method.

**Characterization of materials.** The samples were characterized by X-ray diffraction (XRD, Rigaku, Rint-2500, Cu Kα source), SEM (JEOL JSM-6330FT), and TEM (JEOL JEM-2100, operated at 120 kV). UV-Vis diffuse reflectance spectra (DRS) were obtained on a JASCO V-770 UV-Vis-NIR spectrophotometer. X-ray photoelectron spectroscopy (XPS) was carried out on a JEOL JPS-9010 MC spectrometer. The Brunauer–Emmett–Teller (BET) surface areas were measured by means of nitrogen adsorption-desorption isotherms (BEL Japan, BELSORP max). The pore volumes and pore diameter distributions derived from the adsorption isotherms using the Barrett–Joyner–Halenda (BJH) model.

**Photocatalytic $H_2$ production.** The photocatalytic $H_2$ production experiments were carried out in a tube with a rubber stopper. Typically, 50 mg of samples were dispersed in 50 mL of aqueous solution containing 20 vol% TEOA as the sacrificial electron donor. $H_2PtCl_6·6H_2O$ aqueous solution was added as the precursor for the cocatalyst Pt. Then, the suspension was thoroughly degassed under Ar gas flow and irradiated by a Xenon lamp (Asahi Spectra, LAX-C100) with magnetic stirring at room temperature. A 400-nm cutoff filter was used to remove the UV light. After 30 min photodeposition of Pt on g-$C_3N_4$-$M_xU_y$, the suspension was degassed again. $H_2$ production was measured by using a Shimadzu GC-8A gas chromatograph equipped with an MS-5A column and a thermal conductivity detector. The AQE for $H_2$ production at different wavelengths of the monochromatic light was calculated via the following equation: AQE = (2 × number of $H_2$ molecules/number of incident photons) × 100%. The light intensity at λ= 400, 420, 440, and 460 nm were 0.680, 1.72, 1.44 and 1.77

mW $cm^{-2}$, respectively. The light intensity was measured by Optical Power Meter (1916-R, Newport). The irradiation area was 0.785 $cm^2$.

**Photoelectrochemical measurements.** Photoelectrochemical measurements were carried out in a standard three-electrode quartz cell with a platinum wire as the counter electrode, Ag/AgCl electrodes as the reference electrode, g-$C_3N_4$-$M_xU_y$ modified glass carbon electrode as the working electrode, and 0.5 M $Na_2SO_4$ aqueous solution as the electrolyte. The photocurrent responses and electrochemical impedance spectroscopy (EIS) spectra were recorded at an electrode potential of 0.3 V with a scan rate of 25 mV $s^{-1}$. The working electrode was irradiated by a Xenon lamp (Asahi Spectra, HAL-320W) with a 400 nm cutoff filter. All measurements were carried out at room temperature.

**Single-particle PL measurement by confocal microscopy.** Samples for single-particle photoluminescence (PL) experiments were prepared as follows. The cover glasses (DAICO MFG CO., Ltd.) were cleaned by sonication in a 20% detergent solution (As One, Cleanace) for 7 h, followed by washing with warm water 5 times. g-$C_3N_4$-$M_xU_y$ were well dispersed in ethanol solution and then were spin-coated on the cleaned cover glasses. The cover glasses were annealed at 100 °C for 1 h to immobilize the particles on the surface.

Single-particle PL images and spectra of samples were recorded by using an objective scanning confocal microscope system (PicoQuant, MicroTime 200) coupled with an Olympus IX71 inverted fluorescence microscope. The samples were excited through an oil-immersion objective lens (Olympus, UplanSApochromat, 100×, 1.4 NA) with a circular-polarized 405 nm picoseconds pulsed laser controlled by a PDL-800B driver (PicoQuant). Typical excitation power for the PL measurements was 120 μW at the sample. The emission from the sample was collected by the same objective and detected by a single photon avalanche photodiode (Micro Photon Devices, PDM 50 CT) through a dichroic beam splitter (Chroma, 405rdc) and long pass filter (Chroma, HQ430CP). For the spectroscopy, only the emission that passed through a slit of the imaging spectrograph (Acton Research, SP-2356) was detected with an electron-multiplying charge-coupled device (EMCCD) camera (Princeton Instruments, ProEM). All experimental data were obtained at room temperature.

**Time-resolved diffuse reflectance measurements.** The femtosecond time-resolved diffuse reflectance (TDR) were measured by the pump and probe method

using a regeneratively amplified titanium sapphire laser (SpectraPhysics, Spitfire Pro F, 1 kHz) pumped by a Nd:YLF laser (Spectra-Physics, Empower 15). The second harmonic oscillation of the amplifier (400 nm, 3 μJ per pulse) was used as the excitation pulse. A white light continuum pulse, generated by focusing the residual of the fundamental light on a sapphire crystal, was directed to the sample powder coated on the glass substrate, and the reflected lights were detected by using a linear InGaAs array detector equipped with a polychromator (Solar, MS3504). The pump pulse was chopped by the mechanical chopper synchronized to one-half of the laser repetition rate, resulting in a pair of spectra with and without the pump, from which the absorption change (% absorption) induced by the pump pulse was estimated. All measurements were carried out at room temperature.

## 3. Results and Discussion

The XRD patterns of all samples reveal the formation of g-$C_3N_4$ as shown in Fig. 1a. The peak observed around 13.0 ° correspond to the in-plane tri-s-trizine units. The strongest peak around 27.5 ° is indexed to the (002) plane, demonstrating the graphite-like stacking of the conjugated aromatic units.[22] Compared with g-$C_3N_4$-M, g-$C_3N_4$-$M_xU_y$ showed no XRD peak shift, indicating that U as one of precursors disappeared during the formation of g-$C_3N_4$-$M_xU_y$. It is reported that van der Waals force between layers exists in g-$C_3N_4$. The intensities of the (002) diffraction peaks of g-$C_3N_4$-$M_xU_y$ were found to decrease gradually with increasing the mass ratio of U, suggesting the effective exfoliation of bulk g-$C_3N_4$ into nanosheets through overcoming the weak van der Waals force between layers during the further thermal treatment.[26] In order to confirm the molecular structure of g-$C_3N_4$-$M_xU_y$, FT-IR spectra were measured. All samples showed a peak at 810 $cm^{-1}$ which can be assigned to the out-of-plane bending mode of heptazine rings, while peaks in the range of 900 and 1800 $cm^{-1}$ correspond to N-C=N heterorings in the “melon” framework. The broad band in the range of 3000–3500 $cm^{-1}$ is assigned to uncondensed amine groups resulting from the photocatalysts synthesis as well as water molecules adsorbed on the surface.[27] Using the mixture precursors promotes the planarization of g-$C_3N_4$ layers as shown in Fig. 2, decreasing the interaction between two neighboring atoms separately located in two adjacent tri-s-triazine rings. Therefore, these atoms vibrate more vigorously because of less restraint resulting from increased distances between layers, leading to better distinguished

vibration bands as shown in Fig. 1b.[23] There is neither new peak nor shifted peak, suggesting that U does not influence on the molecular structure of g-$C_3N_4$-$M_xU_y$.

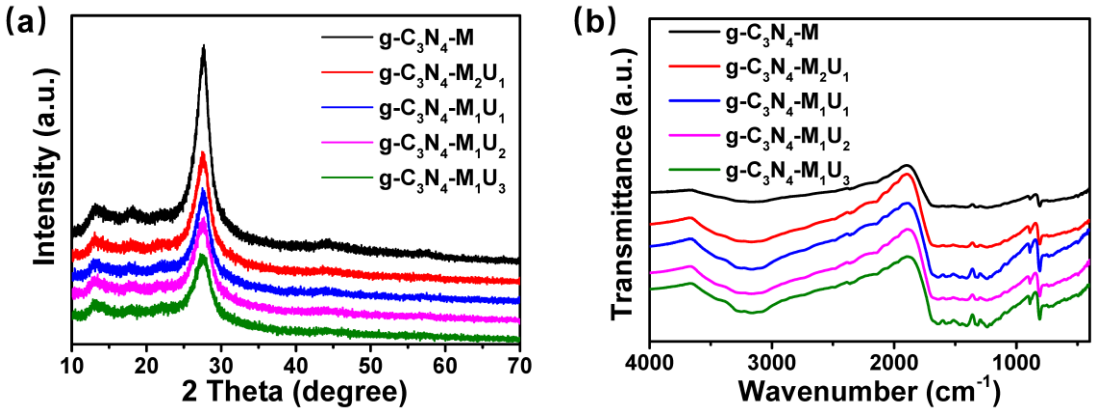


**Figure 1.** XRD patterns (a) and FT-IR spectra (b) of g-$C_3N_4$-M and g-$C_3N_4$-$M_xU_y$.

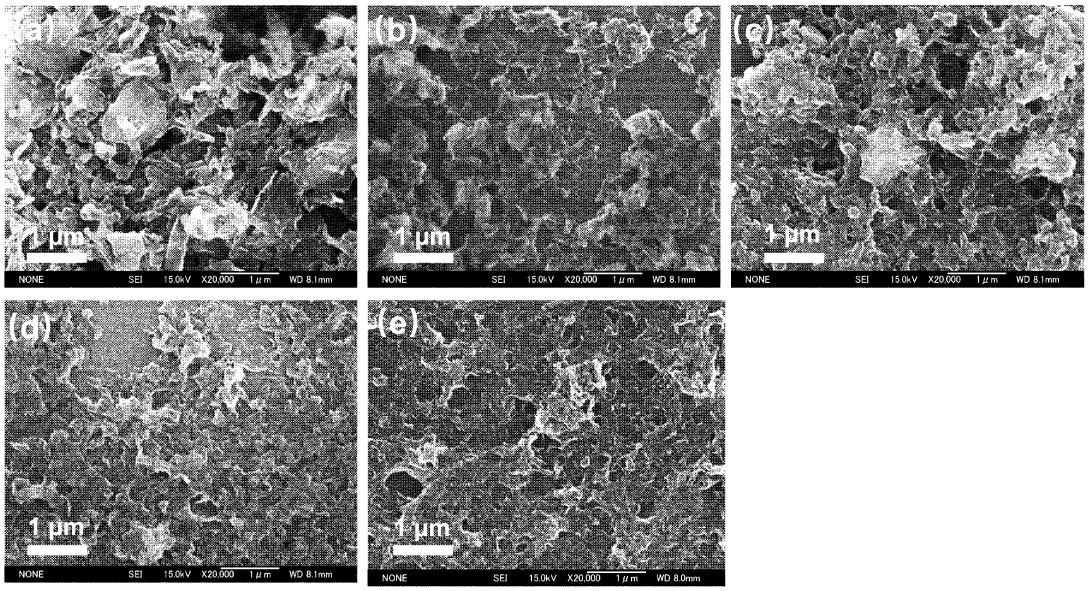


**Figure 2.** SEM images of g-$C_3N_4$-M (a), g-$C_3N_4$-$M_2U_1$ (b), g-$C_3N_4$-$M_1U_1$ (c), g-$C_3N_4$-$M_1U_2$ (d), and g-$C_3N_4$-$M_1U_3$ (e).

The morphology and microstructure of all samples were characterized by SEM and TEM. g-$C_3N_4$-M possesses a thick 2D sheet-like structure, while g-$C_3N_4$-$M_xU_y$ with nanosheet structure are smoother and thinner as shown in SEM and TEM images. All g-$C_3N_4$-$M_xU_y$ possess a large number of in-plane mesoporous distributed in the entire g-$C_3N_4$-$M_xU_y$ layers to offer new exposed active sites as shown in Fig. 3. The surface areas and pore structures of all samples were measured by $N_2$ adsorption-desorption measurements. As shown in Fig. 4, all curves exhibit a typical IV isotherm, assigned to the presence of mesopores (2-50 nm). The hysteresis loops are classified as a type of

H3, indicating the slit-shaped pores in nanosheet materials. The surface areas and pore parameters are summarized in Table 1. Compared with g-$C_3N_4$-M, the surface areas of g-$C_3N_4$-$M_xU_y$ increased gradually with increasing the mass ratio of U mainly due to the presence of oxygen in U precursor, inducing the formation of $CO_2$ during the polymerization.[28] It is well known that high surface area is preferable for photocatalytic efficiency by affording more active sites. The surface area of g-$C_3N_4$-$M_1U_2$ is 233 $m^2$ $g^{-1}$, that is 2 times higher than that of g-$C_3N_4$-M. g-$C_3N_4$-$M_1U_2$ shows the highest efficiency of the photocatalytic $H_2$ production. Except g-$C_3N_4$-$M_1U_3$, the pore size distribution curves of g-$C_3N_4$-$M_xU_y$ have a sharp peak at 2.4-3.0 nm. Although g-$C_3N_4$-$M_1U_3$ shows the largest surface area of 299 $m^2$ $g^{-1}$, the pore diameter (37.9 nm) indicates that excessive U leads to the collapse of the nanosheet structure. The disappeared mesopores results in the low efficiency of the photocatalytic $H_2$ production because of less active sites.

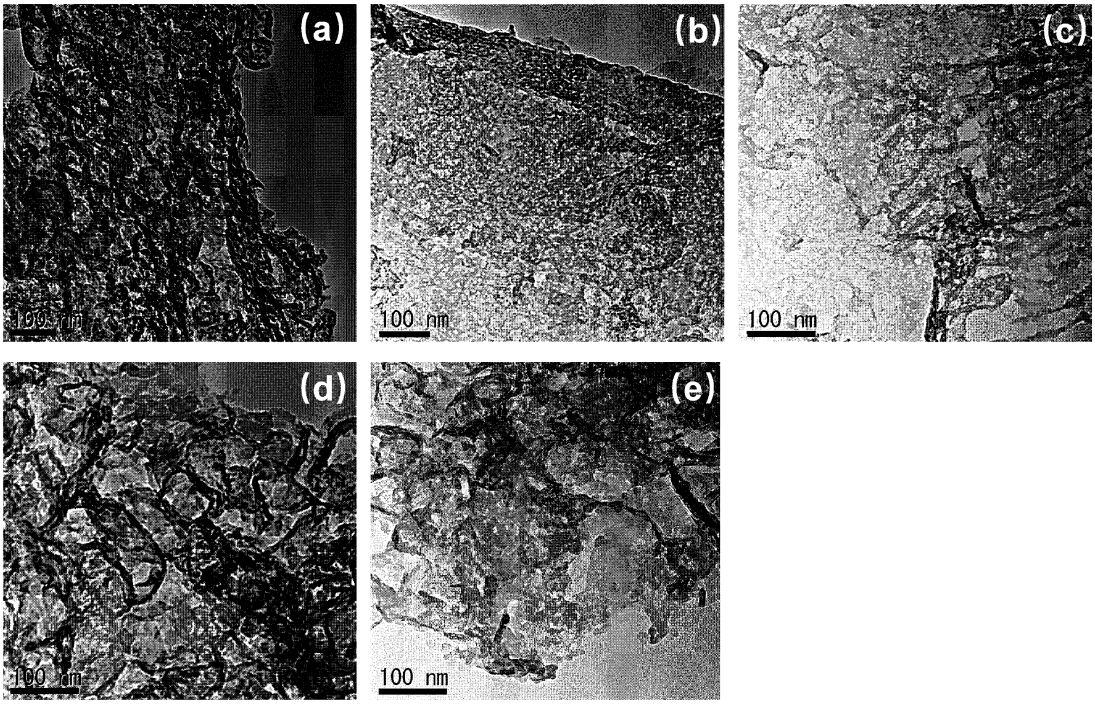


**Figure 3.** TEM images of g-$C_3N_4$-M (a), g-$C_3N_4$-$M_2U_1$ (b), g-$C_3N_4$-$M_1U_1$ (c), g-$C_3N_4$-$M_1U_2$ (d), and g-$C_3N_4$-$M_1U_3$ (e).

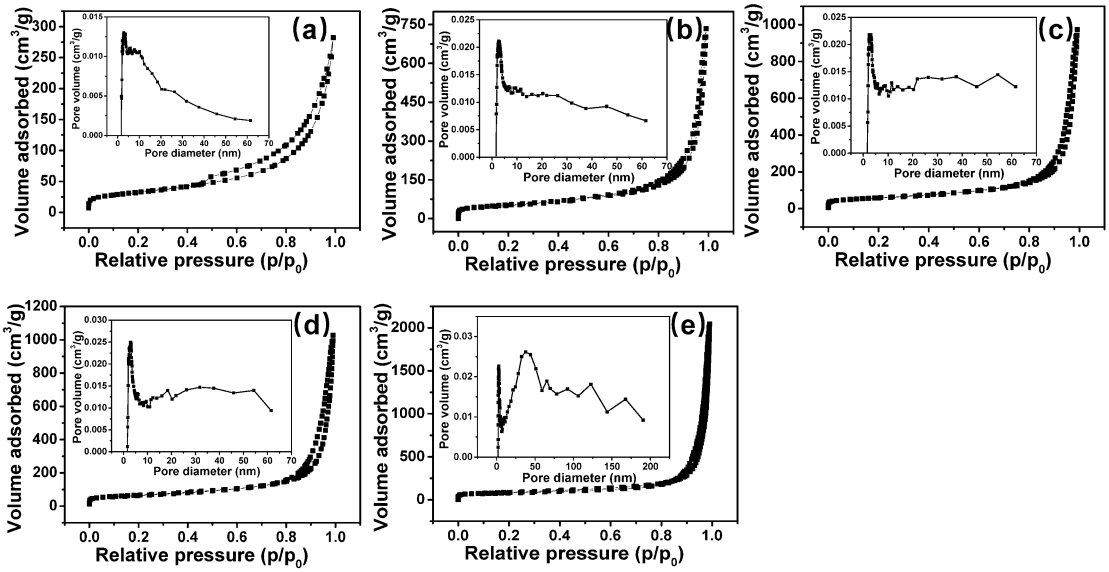


**Figure 4.** $N_2$ adsorption-desorption isotherms and the corresponding pore size distribution curves (inset) of g-$C_3N_4$-M (a), g-$C_3N_4$-$M_2U_1$ (b), g-$C_3N_4$-$M_1U_1$ (c), g-$C_3N_4$-$M_1U_2$ (d), and g-$C_3N_4$-$M_1U_3$ (e).

**Table 1.** Surface areas and pore parameters of g-$C_3N_4$-M and g-$C_3N_4$-$M_xU_y$.

| Sample | Surface area ($m^2\ g^{-1}$) | Pore volume ($cm^3\ g^{-1}$) | Pore diameter[a] (nm) |
|---|---|---|---|
| g-$C_3N_4$-M | 116 | 0.424 | 2.8/14.6 |
| g-$C_3N_4$-$M_2U_1$ | 189 | 1.12 | 2.7/23.7 |
| g-$C_3N_4$-$M_1U_1$ | 211 | 1.46 | 2.4/27.8 |
| g-$C_3N_4$-$M_1U_2$ | 233 | 1.57 | 3.0/27.0 |
| g-$C_3N_4$-$M_1U_3$ | 299 | 3.15 | 37.9/42.1 |

[a]The small and large mesopore diameters are ascribed to the pores within the layer and stacking layers, respectively.[24]

The UV-Vis DRS of g-$C_3N_4$-$M_xU_y$ are presented in Fig. 5a. The bandgap energy ($E_g$) estimated from the plots of $(\alpha h\upsilon)^{1/2}$ *vs* photon energy are 2.64, 2.60, 2.60, 2.60, and 2.61 eV for g-$C_3N_4$-M, g-$C_3N_4$-$M_2U_1$, g-$C_3N_4$-$M_1U_1$, g-$C_3N_4$-$M_1U_2$, and g-$C_3N_4$-$M_1U_3$, respectively, as shown in Figs 5b-f. g-$C_3N_4$-$M_xU_y$ have intense absorption in the Vis light region compared with g-$C_3N_4$-M, primarily resulting from multiple scattering effect associated with their porous structure.[29] Elemental analysis was employed to investigate the defect type in g-$C_3N_4$-$M_xU_y$ as shown in Table 2. The C/N atomic ratio gradually increased from 0.650 in g-$C_3N_4$-M to 0.659 in g-$C_3N_4$-$M_1U_3$, suggesting that

the defects derived from the nitrogen vacancies in g-$C_3N_4$-$M_xU_y$.[30] This indicates that the slightly narrow bandgap and enhanced Vis light absorption are due tonitrogen vacancies.[31] It is reported that nitrogen vacancies in the g-$C_3N_4$ potentially induces additional electron states below the CB.[18]

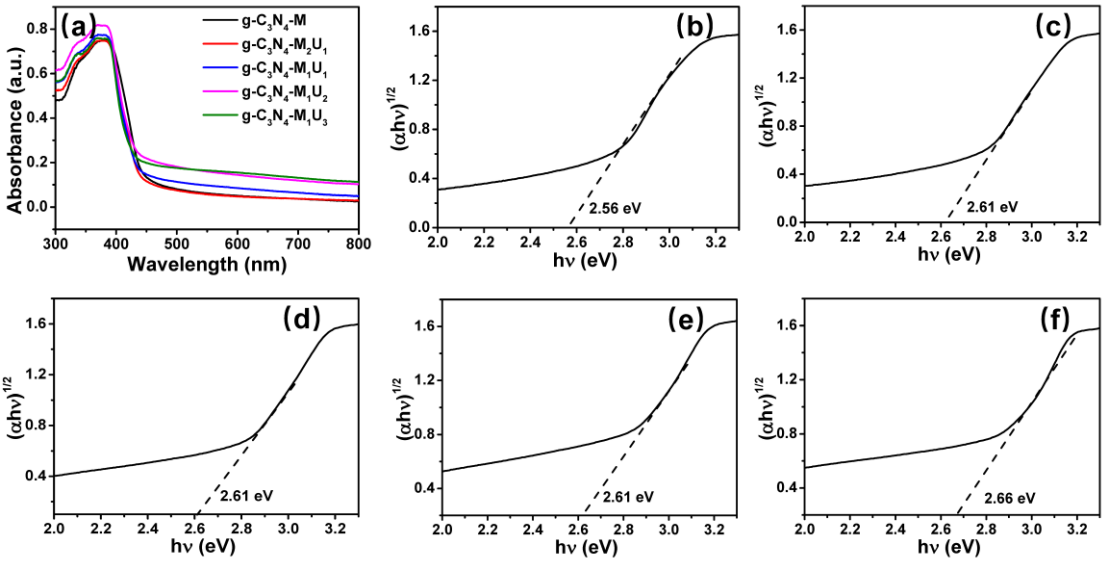


**Figure 5.** UV-Vis DRS (a) and plots of $(\alpha h\upsilon)^{1/2}$ vs photo energy of g-$C_3N_4$-M (b), g-$C_3N_4$-$M_2U_1$ (c), g-$C_3N_4$-$M_1U_1$ (d), g-$C_3N_4$-$M_1U_2$ (e), and g-$C_3N_4$-$M_1U_3$ (f).

Table 2. C/N atomic ratio of g-$C_3N_4$-M and g-$C_3N_4$-$M_xU_y$.

| Sample | C (wt %) | N (wt %) | H (wt %) | C/N atomic ratio |
|---|---|---|---|---|
| g-$C_3N_4$-M | 32.64 | 58.49 | 2.22 | 0.650 |
| g-$C_3N_4$-$M_2U_1$ | 31.23 | 55.66 | 2.16 | 0.654 |
| g-$C_3N_4$-$M_1U_1$ | 32.53 | 57.87 | 2.09 | 0.655 |
| g-$C_3N_4$-$M_1U_2$ | 32.55 | 57.85 | 1.97 | 0.656 |
| g-$C_3N_4$-$M_1U_3$ | 32.66 | 57.88 | 1.92 | 0.658 |

The XPS measurements were carried out to clarify the chemical state of the surface elements of the samples as shown in Fig. 6. The C 1s spectra of g-$C_3N_4$-M and g-$C_3N_4$-$M_1U_2$ exhibit two peaks at the binding energy of 288.5 and 286.1 eV identified to N–C=N coordination in the framework and C–$NH_2$ on the edges of heptazine units, respectively.[32, 33] The N 1s signal was deconvoluted into three peaks with the binding energies at 398.8, 399.5, and 401.2 eV, assigned to $sp^2$ N atoms in triazine ring (C–N=C), bridging N atoms (N($C_3$)), and N–H groups, respectively.[24, 34]

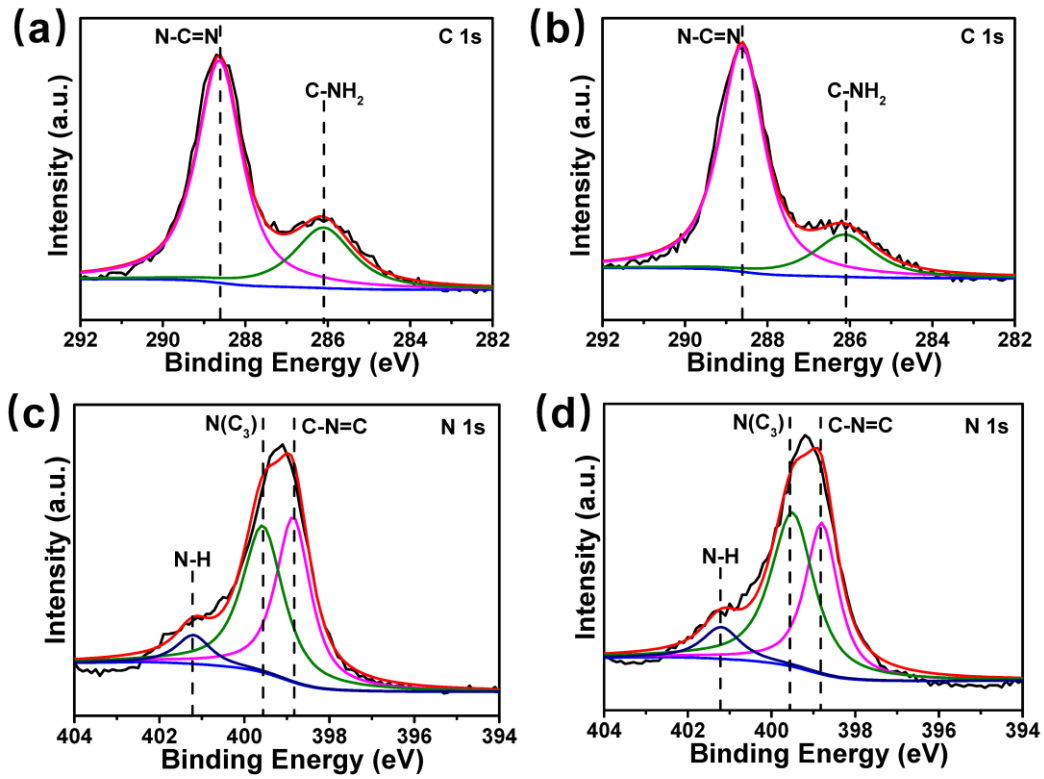


**Figure 6.** XPS spectra of C 1s and N 1s of g-$C_3N_4$-M (a and c) and g-$C_3N_4$-$M_1U_2$ (b and d).

The photocatalytic activities of all samples were evaluated by $H_2$ production rate under Vis light irradiation ($\lambda \geq 400$ nm). As shown in Fig. 7a-b, time-dependent photocatalytic $H_2$ production over photocatalysts with 3.0 wt% Pt as cocatalyst showed that the photocatalytic activity increased gradually with increasing the mass ratio of M to U from 2:1 to 1:2. The $H_2$ production rate of g-$C_3N_4$-$M_1U_2$ was calculated to be 3.1 mmol $g^{-1}$ $h^{-1}$, which is 3.7 times higher than that of g-$C_3N_4$-M (0.8 mmol $g^{-1}$ $h^{-1}$). The enhanced activity can be attributed to the facts that g-$C_3N_4$-$M_1U_2$ has larger surface area and more mesopores to enhance the ET and offer more active sites compared with g-$C_3N_4$-M. Besides, the U induces the formation of defects acting as the trap states for photogenerated electrons, leading to high separation efficiency of the photogenerated charge carriers. Obviously, U plays an important role in increasing the activities of g-$C_3N_4$-$M_xU_y$. Although g-$C_3N_4$-$M_1U_3$ possesses the largest surface area up to 299 $m^2$ $g^{-1}$, the photocatalytic activity decreased resulting from that the excessive U induced collapse of the nanosheet structure and less active sites due to the disappeared mesopores as observed in Table 1. Cycling experiments were carried out to evaluate the stability of g-$C_3N_4$-$M_1U_2$ photocatalyst as shown in Fig. 7c. The $H_2$ production rate

of g-$C_3N_4$-$M_1U_2$ after four cycles was sustained and no significant degradation was confirmed, indicating the stability of g-$C_3N_4$-$M_1U_2$ photocatalyst. The AQE of g-$C_3N_4$-$M_1U_2$ was estimated to be 74 % at λ= 400 nm and 28 % at λ= 420 nm (Fig. 7d).

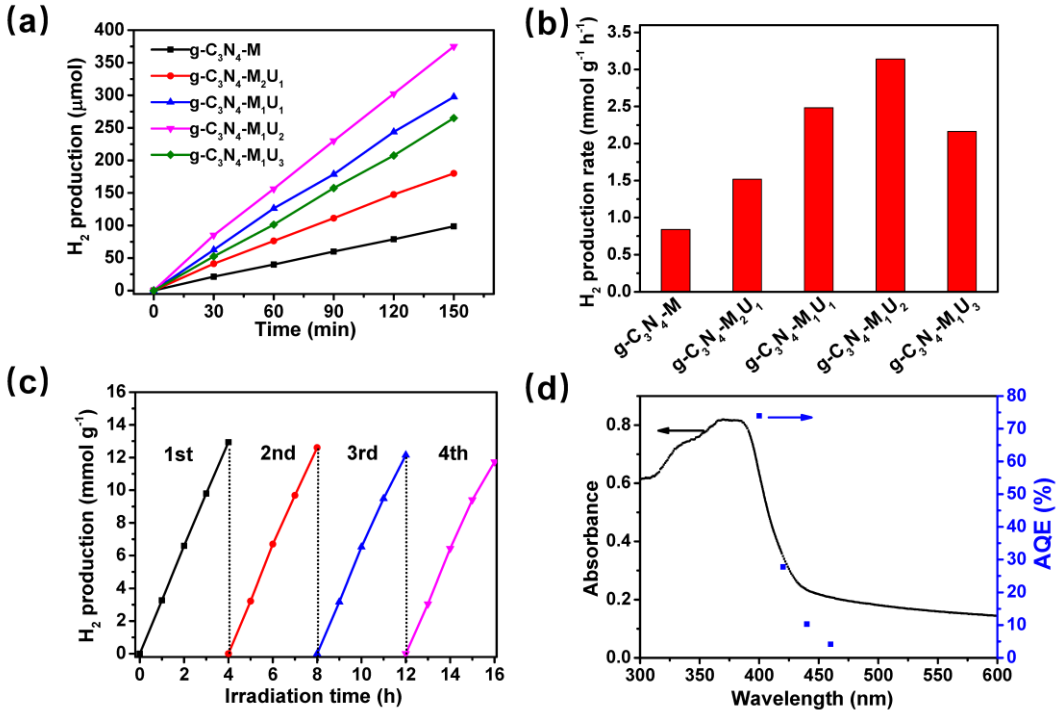


**Figure 7.** Time-dependent (a) and photocatalytic rate (b) of $H_2$ production for g-$C_3N_4$-M and g-$C_3N_4$-$M_xU_y$. Cycling tests (c) and AQE of photocatalytic $H_2$ production for g-$C_3N_4$-$M_1U_2$.

The photocurrent responses of all samples were measured via several on-off cycles of intermittent Vis light irradiation, directly correlating with the separation efficiency of the photogenerated charge carriers. As shown in Fig. 8a, the photocurrent responses of all samples were stable and reproducible in the time scale of 30-240 s. The photocurrent density of g-$C_3N_4$-$M_1U_2$ was higher than that of other samples due to efficient charge separation and transfer resulting from larger surface area, mesopores, and defects. Furthermore, EIS was measured to clarify the electrical conductivity of all samples. As shown in Fig. 8b, a smaller arc radius of the EIS Nyquist plot indicates smaller resistance and faster charge transfer. The enhanced photoelectric properties of g-$C_3N_4$-$M_1U_2$ are attributable to the effective exfoliation from bulk into nanosheets to improve charge mobility.

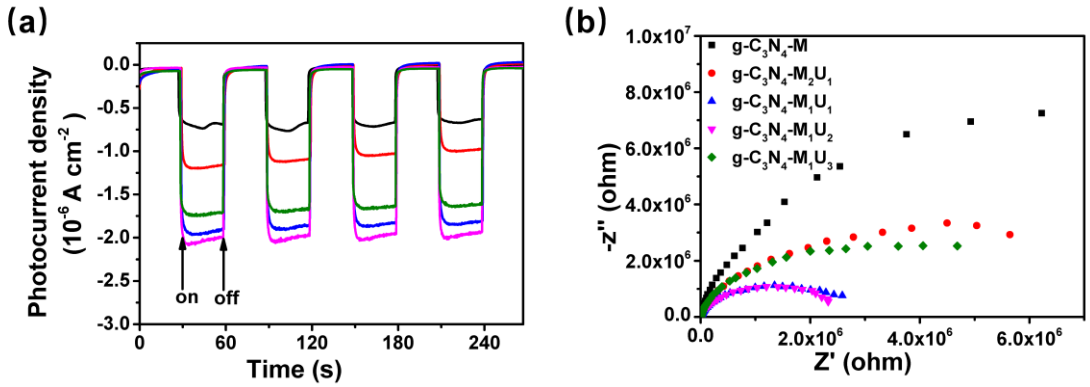


**Figure 8.** Photocurrent response (a) and EIS (b) for g-$C_3N_4$-M and g-$C_3N_4$-$M_xU_y$.

Single-particle PL was used to disucss the separation and transfer mechanism of charge carriers[35, 36] in g-$C_3N_4$-$M_xU_y$. PL images of all samples are shown in Fig. 9a-e. Five locations were randomly chosen for each sample as marked with Arabic numbers in the images. Representatively, PL spectra of g-$C_3N_4$-$M_xU_y$ at the position numbered "1" are shown in Fig. 9f, while the PL intensities of other four locations as numbered from "2" to "5" are shown in Fig. 10. The PL intensity gradually decreased with increasing the mass ratio of M to U from 2:1 to 1:2, indicating a slower recombination rate of the charge carriers in g-$C_3N_4$-$M_1U_2$. The average PL lifetimes of g-$C_3N_4$-$M_xU_y$ represent the recombination of charge carriers. Fig.11 shows that the PL lifetime was 3.5 ns for g-$C_3N_4$-$M_1U_2$, which is1.42 times longer than that of g-$C_3N_4$-M, indicating that g-$C_3N_4$-$M_xU_y$ possesses the slower recombination process of photogenerated electrons than g-$C_3N_4$-M. Similar to the discussion on the photocatalytic activity for foam-like holey ultrathin g-$C_3N_4$,[37] more electrons transfer to Pt nanoparticles in g-$C_3N_4$-$M_1U_2$ to give a higher yield of $H_2$ production than in g-$C_3N_4$-M. For g-$C_3N_4$-$M_1U_3$, the decreased lifetime is probably due to the excessive defects derived from disappeared U could serve as recombination centers for the electrons and holes. The PL lifetime of g-$C_3N_4$-$M_1U_3$ is short than that of g-$C_3N_4$-$M_1U_2$, which indicates that charge carriers recombine faster in g-$C_3N_4$-$M_1U_3$ than that in g-$C_3N_4$-$M_1U_2$. It is reported that overintroduction of nitrogen vacancies could generate the deeper midgap states that act as recombination sites.[46]

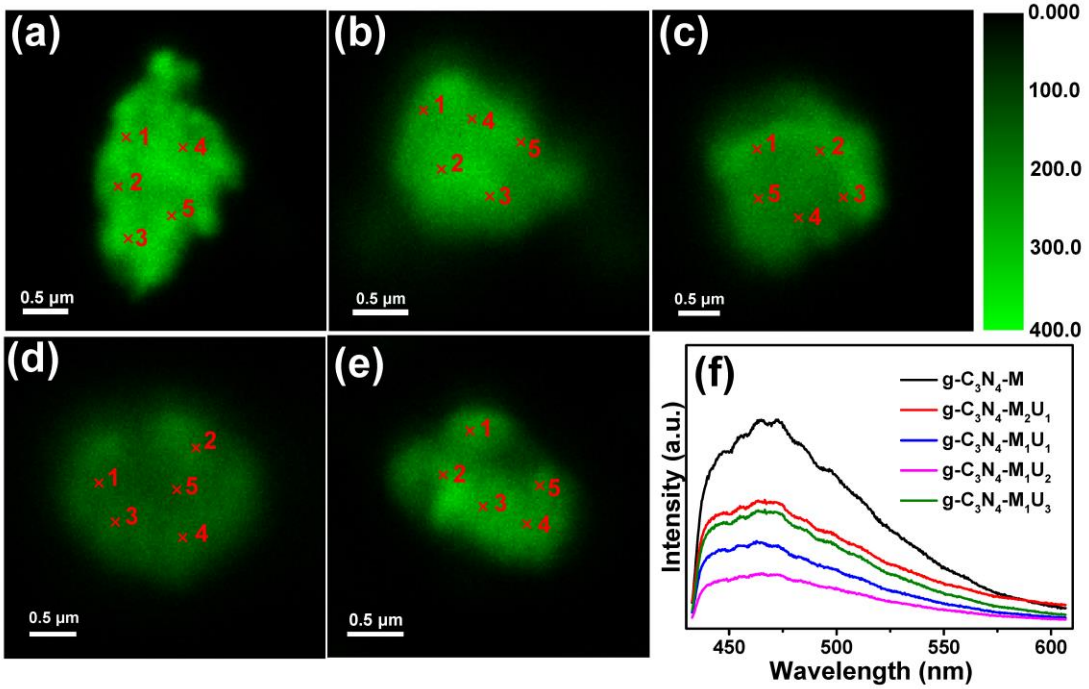


**Figure 9.** PL images of g-$C_3N_4$-$M_xU_y$ on a quartz cover glass. g-$C_3N_4$-M (a), g-$C_3N_4$-$M_2U_1$ (b), g-$C_3N_4$-$M_1U_1$ (c), g-$C_3N_4$-$M_1U_2$ (d), and g-$C_3N_4$-$M_1U_3$ (e). Representative PL spectra of g-$C_3N_4$-$M_xU_y$ as numbered "1" in (a)-(e).

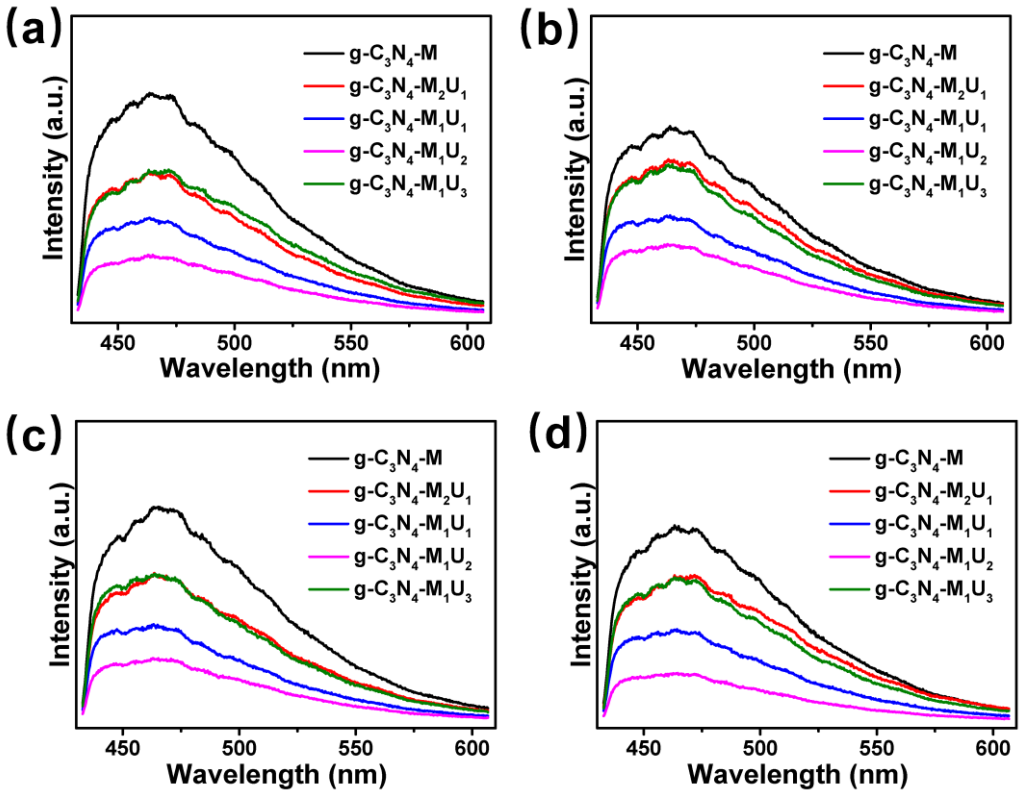


**Figure 10.** PL spectra of g-$C_3N_4$-$M_xU_y$ as numbered from "2" to "5" corresponding to the PL images in Figure 9.

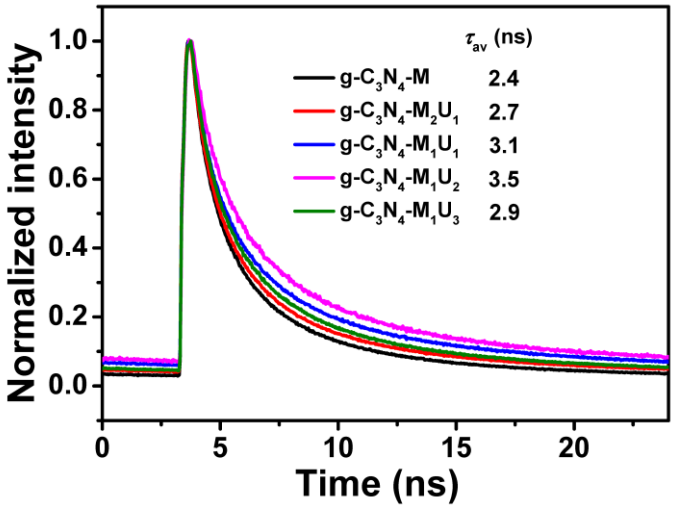


**Figure 11.** PL decay profiles of g-$C_3N_4$-M and g-$C_3N_4$-$M_xU_y$.

TDR measurement was carried out to obtain the information of charge lifetimes and charge transfer processes[38-40] of g-$C_3N_4$-$M_xU_y$ under Vis light irradiation. Upon the 400 nm laser light irradiation to g-$C_3N_4$-$M_xU_y$, electrons and holes are generated in CB and VB, respectively. A broad transient absorption signal in the range of 850-1150 nm which can be assigned to the trapped and free electrons in the semiconductors,[7] was observed for all samples as shown in Fig.12. For all samples, the transient absorption signals reached the highest intensities immediately after a 400-nm laser irradiation, and then gradually decayed. To elucidate the decay kinetics, the time profiles of the transient absorption at 950 nm for all samples were fitted by two-exponential functions as shown in Fig. 13a, and their lifetimes are summarized in Table 3. It is known that successive pathways of exciton relaxation to two trap states with different trap depths are analyzed by two decay time constants.[41] The decay profiles of g-$C_3N_4$-$M_xU_y$ were fitted by a two-exponential decay function with short and long lifetimes $\tau_1$ and $\tau_2$, corresponding to the trapping of electrons by shallow trap state and deep trap state, respectively.[42] The decay profile of transient absorption for g-$C_3N_4$-M was fitted with a short lifetime $\tau_1$ (52 ps, 27%) and long lifetime $\tau_2$ (1229 ps, 73%). For g-$C_3N_4$-$M_xU_y$ sample, $\tau_1$ and $\tau_2$ decrease gradually with increasing the density of defects by increasing the mass ratio of U. Recently, several studies have indicated that charge trapping derived from defects plays a crucial role in photocatalytic activity of $C_3N_4$ materials.[31, 43, 44] In our experiments, an increase in U leads an increase in defects acting as the electron trap states of photogenerated electrons, resulting in a shorter $\tau_1$ and $\tau_2$, indicating that the photogenerated electrons in CB and shallow trap states of g-$C_3N_4$-

$M_xU_y$ are fast trapped by the defects. Therefore, the trapping by deep trap states, which is not active for $H_2$ evolution, could be retarded. It has been reported that ET from $C_3N_4$ to cocatalyst Pt in the ns timescale which competes with electron trapping in $C_3N_4$.[45] Therefore, more electrons transfer from g-$C_3N_4$-$M_xU_y$ to Pt nanoparticles compared with g-$C_3N_4$-M, leading to efficient production of $H_2$.

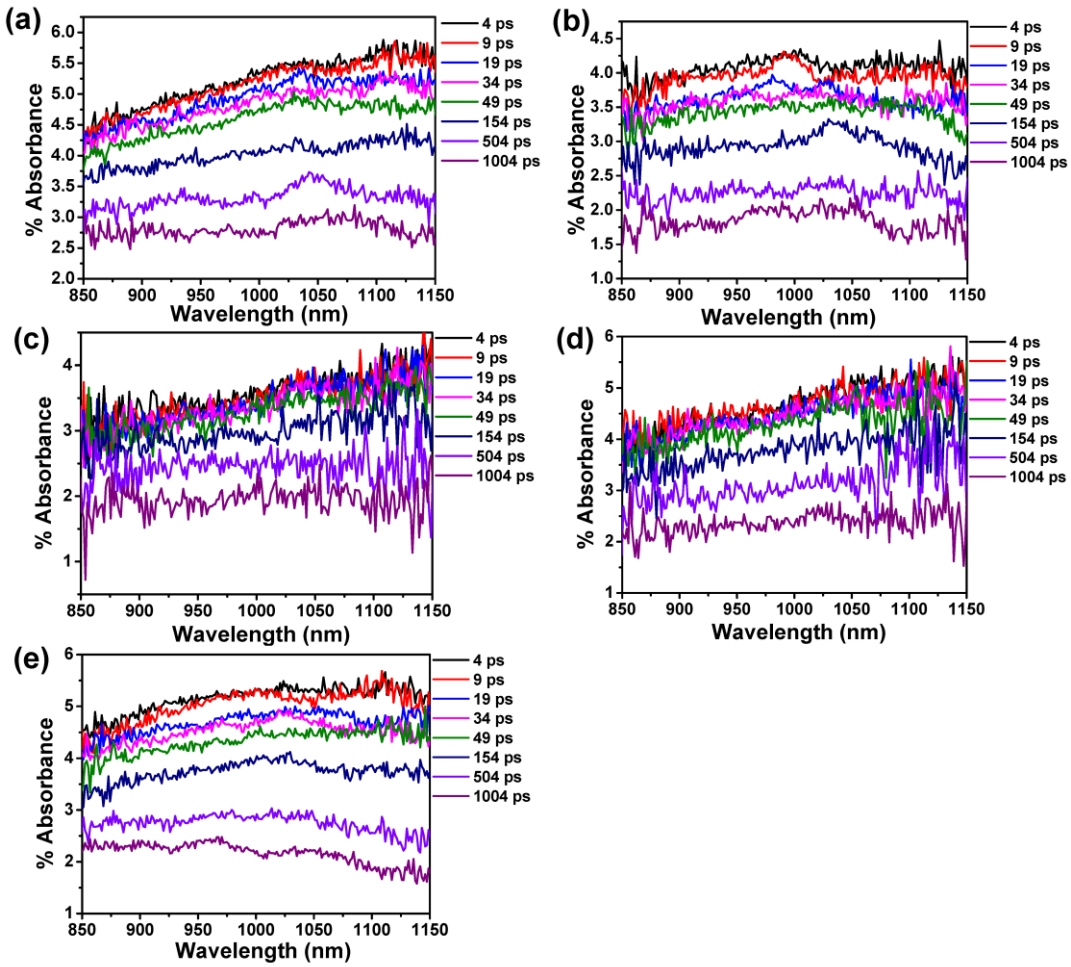


**Figure 12.** Time-resolved diffuse reflectance spectra of g-$C_3N_4$-M (a), g-$C_3N_4$-$M_2U_1$ (b), g-$C_3N_4$-$M_1U_1$ (c), g-$C_3N_4$-$M_1U_2$ (d), and g-$C_3N_4$-$M_1U_3$ (e).

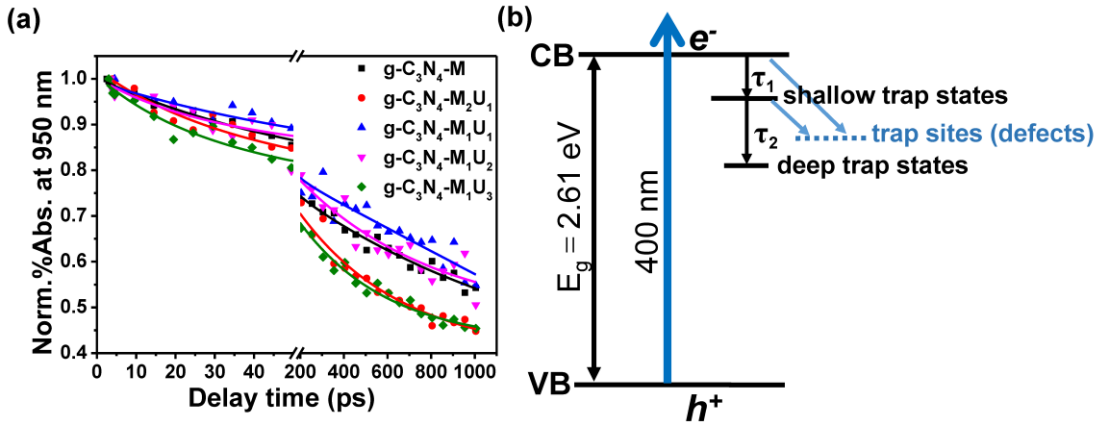


**Figure 13.** Time profiles of normalized transient absorption at 950 nm for all samples after 400-nm laser irradiation (a) and schematic illustration of photogenerated electron trapping by the trap states in g-$C_3N_4$-$M_xU_y$ (b).

**Table 3.** Lifetimes of TDR decays for all samples under 400-nm irradiation.

| Sample | $\tau_1$ (ps) | $\tau_2$ (ps) | $\tau_{av}$ (ps) |
|---|---|---|---|
| g-$C_3N_4$-M | 52±9 (27%) | 1229±258 (73%) | 911 |
| g-$C_3N_4$-$M_2U_1$ | 29±10 (25%) | 476±94 (75%) | 364 |
| g-$C_3N_4$-$M_1U_1$ | 41±13 (24%) | 712±81 (76%) | 551 |
| g-$C_3N_4$-$M_1U_2$ | 24±10 (28%) | 628±87 (72%) | 459 |
| g-$C_3N_4$-$M_1U_3$ | 24±7 (30%) | 409±56 (70%) | 294 |

# 4. Conclusion

Defects rich g-$C_3N_4$-$M_xU_y$ with high surface area and mesoporous and nanosheet structure were synthesized by using a mixture of M and U as the precursors. Femtosecond TDR measurements revealed that photogenerated electrons in CB of g-$C_3N_4$-$M_xU_y$ are efficiently trapped by the defects. g-$C_3N_4$-$M_1U_2$ exhibited $H_2$ production rate of 3.1 mmol $g^{-1}$ $h^{-1}$ under Vis light irradiation and AQE was estimated to be 74% at λ = 400 nm. U plays a crucial role in enhancement of photocatalytic performance by improving surface area and efficient photogenerated electron trapping. The present work provides a simple method for synthesis of defects rich carbon nitride with high surface area to exhibit efficient photocatalytic activity.

# 5. References


1. A. Fujishima and K. Honda, *Nature*, 1972, **238**, 37.
2. X. Wang, K. Maeda, A. Thomas, K. Takanabe, G. Xin, J. M. Carlsson, K. Domen and M. Antonietti, *Nat. Mater.*, 2009, **8**, 76-80.
3. G-h. Moon, M. Fujitsuka, S. Kim, T. Majima, X. Wang and W. Choi, *ACS Catal.*, 2017, **7**, 2886-2895.
4. C. Pan, J. Xu, Y. Wang, D. Li and Y. Zhu, *Adv. Funct.Mater.*, 2012, **22**, 1518-1524.
5. X. Bai, L. Wang, R. Zong and Y. Zhu, *J. Phys. Chem. C*, 2013, **117**, 9952-9961.
6. L. Lin, W. Ren, C. Wang, A. M. Asiri, J. Zhang and X. Wang, *Appl. Catal. B: Environ.*, 2018, **231**, 234-241.
7. M. Zhu, S. Kim, L. Mao, M. Fujitsuka, J. Zhang, X. Wang and T. Majima, *J. Am. Chem. Soc.*, 2017, **139**, 13234-13242.
8. M. Q. Wen, T. Xiong, Z. G. Zang, W. Wei, X. S. Tang and F. Dong, *Opt. Express*, 2016, **24**, 10205-10212.
9. P. Niu, L. Zhang, G. Liu and H.-M. Cheng, *Adv. Funct. Mater.*, 2012, **22**, 4763-4770.
10. H. Ou, L. Lin, Y. Zheng, P. Yang, Y. Fang and X. Wang, *Adv. Mater.*, 2017, **29**, 170008.
11. P. Yang, H. Ou, Y. Fang and X. Wang, *Angew. Chem. Int. Ed.*, 2017, **56**, 3992-3996.
12. Z. Lin and X. Wang, *Angew. Chem. Int. Ed.*, 2013, **52**, 1735-1738.
13. G. Liu, T. Wang, H. Zhang, X. Meng, D. Hao, K. Chang, P. Li, T. Kako and J. Ye, *Angew. Chem. Int. Ed.*,2015, **54**, 13561-13565.
14. W. Liu, L. Cao, W. Cheng, Y. Cao, X. Liu, W. Zhang, X. Mou, L. Jin, X. Zheng, W. Che, Q. Liu, T. Yao and S. Wei, *Angew. Chem. Int. Ed.*, 2017, **56**, 9312-9317.
15. X. Shi, M. Fujitsuka, Z. Lou, P. Zhang and T. Majima, *J. Mater. Chem. A*, 2017, **5**, 9671-9681.
16. D. Zheng, X. N. Cao and X. Wang, *Angew. Chem. Int. Ed.*, 2016, **55**, 11512-11516.
17. B. W. Sun, H. J. Li, H. Y. Yu, D. J. Qian and M. Chen, *Carbon*, 2017, **117**, 1-11.
18. Q. Tay, P. Kanhere, C. F. Ng, S. Chen, S. Chakraborty, A. C. H. Huan, T. C. Sum, R. Ahuja and Z. Chen, *Chem. Mater.*, 2015, **27**, 4930-4933.

19. S. Patnaik, S. Martha and K. M. Parida, *RSC Adv.*, 2016, **6**, 46929-46951.
20. Y. Wang, X. Wang and M. Antonietti, *Angew. Chem. Int. Ed.*, 2012, **51**, 68-89.
21. M. Groenewolt and M. Antonietti, *Adv. Mater.*, 2005, **17**, 1789-1792.
22. S. Martha, A. Nashim and K. M. Parida, *J. Mater. Chem. A*, 2013, **1**, 7816-7824.
23. X. Fan, Z. Xing, Z. Shu, L. Zhang, L. Wang and J. Shi, *RSC Adv.*, 2015, **5**, 8323-8328.
24. F. Dong, Z. Ni, P. Li and Z. Wu, *New J. Chem.*, 2015, **39**, 4737-4744.
25. F. Dong, Z. Zhao, T. Xiong, Z. Ni, W. Zhang, Y. Sun and W. K. Ho, *ACS Appl. Mater. Interfaces*, 2013, **5**, 11392-11401.
26. J. Xu, L. Zhang, R. Shi and Y. Zhu, *J. Mater. Chem. A*, 2013, **1**, 14766-14772.
27. H. Yu, R. Shi, Y. Zhao, T. Bian, Y. Zhao, C. Zhou, G. I. N. Waterhouse, L. Z. Wu, C. H. Tung and T. Zhang, *Adv. Mater.*, 2017, **29**, 1605148.
28. G. Zhang, J. Zhang, M. Zhang and X. Wang, *J. Mater. Chem.*, 2012, **22**, 8083-8091.
29. Z. Tong, D. Yang, Y. Sun, Y. Nan and Z. Jiang, *Small*, 2016, **12**, 4093-4101.
30. P. Niu, G. Liu and H.-M. Cheng, *J. Phys. Chem.C*, 2012, **116**, 11013-11018.
31. J. Ding, W. Xu, H. Wan, D. Yuan, C. Chen, L. Wang, G. Guan and W. L. Dai, *Appl. Catal. B: Environ.*, 2018, **221**, 626-634.
32. X. Wang, J. Cheng, H. Yu and J. Yu, *Dalton Trans.*, 2017, **46**, 6417-6424.
33. M. Wu, J. M. Yan, X. N. Tang, M. Zhao and Q. Jiang, *ChemSusChem*, 2014, **7**, 2654-2658.
34. Y. Li, H. Zhang, P. Liu, D. Wang, Y. Li and H. Zhao, *Small*, 2013, **9**, 3336-3344.
35. Z. Lou, M. Fujitsuka and T. Majima, *ACS Nano*, 2016, **10**, 6299-6305.
36. Z. Zheng, T. Tachikawa and T. Majima, *J. Am. Chem. Soc.*, 2014, **136**, 6870-6873.
37. Y. Li, R. Jin, Y. Xing, J. Li, S. Song, X. Liu, M. Li and R. Jin, *Adv. Energy Mater.*, 2016, **6**, 1601273.
38. P. Zhang, M. Fujitsuka and T. Majima, *Nanoscale*, 2017, **9**, 1520-1526.
39. Z. Bian, T. Tachikawa, P. Zhang, M. Fujitsuka and T. Majima, *J. Am. Chem. Soc.*, 2014, **136**, 458-465.
40. I. Grigioni, K. G. Stamplecoskie, E. Selli and P. V. Kamat, *J. Phys. Chem. C*, 2015, **119**, 20792-20800.
41. D. A. Wheeler and J. Z. Zhang, *Adv. Mater.*, 2013, **25**, 2878-2896.
42. H. Y. Zhang, Y. P. Chen, R. Lu, R. Y. Li, A. C. Yu. *Phys. Chem. Chem. Phys.*, 2016, **18**, 14904-14910.

43. V. W. Lau, I. Moudrakovski, T. Botari, S. Weinberger, M. B. Mesch, V. Duppel, J. Senker, V. Blum and B. V. Lotsch, *Nat. Commun.*, 2016, **7**, 12165.
44. L. Shi, L. Yang, W. Zhou, Y. Liu, L. Yin, X. Hai, H. Song and J. Ye, *Small*, 2018, 1703142.
45 R. Godin, Y. Wang, M. A. Zwijnenburg, J. Tang and J. R. Durrant, *J. Am. Chem. Soc.*, 2017, **139**, 5216-5224.
46. W. Tu, Y. Xu, J. Wang, B. Zhang, T. Zhou, S. Yin, S. Wu, C. Li, Y. Huang, Y. Zhou, Z. Zou, J. Robertson, M. Kraft and R. Xu, *ACS Sustain. Chem. Eng.*, 2017, **5**, 7260-7268.

# Chapter 2. Ultrafast Spectroscopic Study of Plasmon-induced Hot Electron Transfer under NIR Excitation in Au Triangular Nanoprisms/g-$C_3N_4$ for Photocatalytic $H_2$ Production

## 1. Introduction

Solar-light-driven $H_2$ production using photocatalysts has emerged as a promising strategy to deal with imminent energy crisis.[1, 2] Among various photocatalysts, $TiO_2$ has been extensively studied in the last several decades for various photocatalytic reaction.[3, 4] However, $TiO_2$ possesses a wide band gap of 3.2 eV that only can be excited by UV light, which restrict its widespread application. Vis-light-responsive semiconductor photocatalysts have been developed in recent decade since sunlight consists of ca. 48% Vis light.[5] Particularly, g-$C_3N_4$is regarded as one of the most promising candidates for photocatalytic solar energy conversion.[6-8] Nevertheless, the NIR light, which accounts for ca. 44% of the solar spectrum, remains unutilized. The search for photocatalysts that can harvest NIR light is still a challenging mission. Recently, the surface plasmon resonance (SPR) effect of nanostructure noble metals has been exploited to realize variety photocatalytic reactions in the Vis and NIR regions,[9] such as first report about methanol and ethanol oxidation by plasmon-induced photoelectrochemistry[10] and organic compounds photodeposition[11] in visible region using plasmonic hybrid Au/$TiO_2$.The SPR effect is greatly influenced by their size and Au nanosturctures, such as nanospheres,[12] nanorods,[13] and nanoprisms,[14] and is found to show SPR bands in the Vis and NIR regions. Different from Au nanospheres and Au nanorods, two-dimensional Au triangular nanoprisms (TNPs) exhibit various modes of SPR effect containing in-plane dipole surface plasmon resonance (DSPR), multipole in-plane dipole surface plasmon resonance (MSPR), and out-of-plane SPR in the visible and NIR regions.[15] Single-particle PL spectra of Pt-modified Au TNPs demonstrated that DSPR of Au TNPs enhanced the hot ET from Au TNPs to Pt leading to $H_2$ generation.[16] Plasmonic photocatalysts consist of noble metal nanoparticles and semiconductors, in which the noble metal nanoparticles serve as a photosensitizer that generates high energy electrons upon SPR excitation and injects them into the CB of semiconductor.[17]

In this work, we found that Au TNPs/g-$C_3N_4$, prepared by successfully loading Au TNPs on the surface of g-$C_3N_4$ nanosheet as shown in scheme 1, shows photocatalytic

$H_2$ production under NIR light ($\lambda \geq 780$ nm) irradiation. We unveil the plasmon-induced hot ET from Au TNPs to g-$C_3N_4$ for the $H_2$ production. Finite-difference time-domain (FDTD) simulations confirm a stronger electromagnetic field in Au TNPs/g-$C_3N_4$ than that of Au TNPs. Time-resolved transient absorption measurements reveal the dynamics of plasmon-induced hot electrons in Au TNPs/g-$C_3N_4$ hybrid which is different from that in Au TNPs.

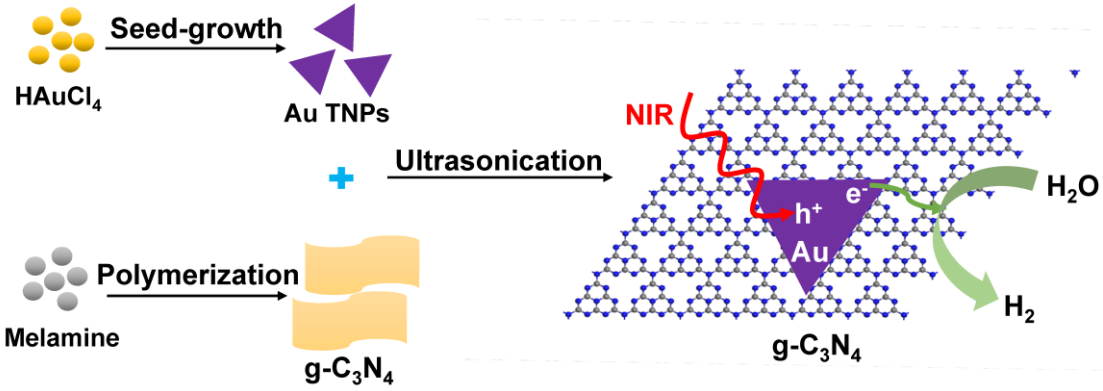


**Scheme 1.** Illustration for synthesizing Au TNPs/g-$C_3N_4$.

## 2. Experimental Section

**Materials.** Materials used were melamine (≥99.0%, Wako), hexadecyltrimethylammonium chloride (CTAC, ≥95%, Wako), hydrogen tetrachloroaurate(III) trihydrate ($HAuCl_4 \cdot H_2O$, ≥99.999%, Aldrich), hydrogen hexachloroplatinate- (IV) hydrate ($H_2PtCl_6 \cdot nH_2O$, ≥99.9%, Aldrich), L-ascorbic acid (≥99.5%, Wako), potassium iodide (≥99.5%, Nacalai), sodium borohydride ($NaBH_4$, ≥99%, Aldrich ), and silver nitrate (≥99%, Nacalai). All chemicals were used after purchased without further purification.

**Synthesis of g-$C_3N_4$.** The g-$C_3N_4$ nanosheets was prepared from 5g melamine by thermal condensation as shown in Chapter 1.

**Synthesis of Gold Triangular Nanoprisms (Au TNPs).** Au TNPs were synthesized by seed-growth method, following previous publications from our group.[16] Typically, Au seed was prepared firstly as follows: 25 μL 50 mM $HAuCl_4$ solution was added into 4.7 mL 0.1 M CTAC solution and then 300 μL 10 mM $NaBH_4$ solution was added under vigorous stirring. The mixture solution was kept for stirring for 2 h at room temperature.

The Au seed solution was diluted 10 times in 0.1 M CTAC solution for further use.

Next, two kinds of growth solutions were prepared. 1.6 mL of 0.1 M CTAC solution, 80 μL of 10 mM $KI_3$, 40 μL of 50 mM $HAuCl_4$ and 40 μL of 0.1 M L-ascorbic acid were added step by step into 8 mL of Milli-Q water which was labeled as A solution. 400 μL of 10 mM $KI_3$, 500 μL of 50 mM $HAuCl_4$ and 400 μL of 0.1 M L-ascorbic acid were added step by step into 40 mL of 50 mM of solution which was labeled as B solution. Then, 200 μL diluted Au seed solution was added into A solution with shaking and 3.2 mL of A solution was added into B solution quickly. The mixture solution was shaked for several seconds and then left undisturbed at room temperature for 1 h for complete growth of Au TNPs. Purification of Au TNPs was done as follows: 200 μL of 25 wt% CTAC was added into above-mentioned solution and then the solution was left alone for overnight. After that, suspension liquid of solution was removed and precipitate was left on the bottom. 10 mL of 20 mM CTAC was added into the bottle and green solution was obtained after ultrasonic treatment. 0.33 mg $Au^0$ was obtained (calculated by the results of ICP measurement).

**Synthesis of Au TNPs/g-$C_3N_4$.** 50 mg of g-$C_3N_4$ was dispersed in 10 mL of aqueous solution containing 100 μL of $NH_3 \cdot H_2O$ and 200 μL of 3-mercaptopropionic acid (3-MPA), and then was kept for stirring for 12 h. Au TNPs solution was washed with $H_2O$ thoroughly to remove the CTAC and then dispersed in aqueous solution for the further use. A calculated volume of Au TNPs solution was added into above g-$C_3N_4$ solution. After ultrasonic treatment for 30 min and stirring for 12 h, the mixture was centrifuged, washed with water and ethanol, freeze dried to obtain the final product.

**Characterizations.** The samples were characterized by XRD, XPS, TEM, and UV-Vis DRS as in Chapter 1. Energy dispersive Spectroscopy (EDS). High Resolution Transmission Electron Microscope(HRTEM).

**Photocatalytic $H_2$ production tests.** Typically, 50 mg of samples were dispersed in 50 mL of aqueous solution containing 20 vol% methanol as the sacrificial electron donor. The suspension was thoroughly degassed under Ar gas flow and irradiated by a Xenon lamp (Asahi Spectra, LAX-C100) with magnetic stirring at room temperature. A 780-nm cutoff filter was used to remove the UV-Vis light. The volume of $H_2$ was measured as in Chapter 1

**Finite-difference-time-domain (FDTD) calculations.** The computational simulations were performed by using the method of finite-difference-time-domain

(FDTD), a software package, FDTD Solutions 8.19 (Lumerical Solutions, Inc.). The override mesh cell size was 1×1×0. 1 $nm^3$. The optical constant of Au was adopted from tabulated values for bulk gold measured by Johnson and Christy. During the calculation, an electromagnetic pulse in the wavelength range from 780 to 1600 nm was launched into a box containing a target nanostructure. The size of TNPs was modeled as a triangular nanoplate with length of 129 nm and thickness of 6 nm. The refractive index of the medium (water) was set to be 1.33.

**Time-resolved transient absorption measurements.** The femtosecond transient absorption (TA) spectra were measured by the pump and probe method using a regenerative amplified titanium sapphire laser. In this chapter the samples were excited using 1100 nm laser light generated by an optical parametric amplifier (Spectra Physics, OPA-800CF-1).

## 3. Results and Discussion

The morphology and microstructures of g-$C_3N_4$, Au TNPs, and Au TNPs/g-$C_3N_4$ were characterized by TEM. Au TNPs with uniform morphology were prepared as shown in Fig.1a-b and the length of Au TNPs was estimated to be 129 nm. The thickness of Au TNPs is found to be 6.2 nm from the side view as shown in Fig. 1c. Fig. 1d presents that g-$C_3N_4$ possesses a 2D flat nanosheet structure which is considered to be a good charge carrier for loaded Au TNPs. Fig. 1e shows that Au TNPs are successfully dispersed on the g-$C_3N_4$ nanosheet. The high resolution TEM (HRTEM) image shows the lattice spacing of 0.24 nm, corresponding to Au (111) lattice plane (Fig. 1f).[18] Elemental mapping further confirms that Au TNPs are loaded on the surface of g-$C_3N_4$ nanosheet uniformly as shown in Fig. 2.

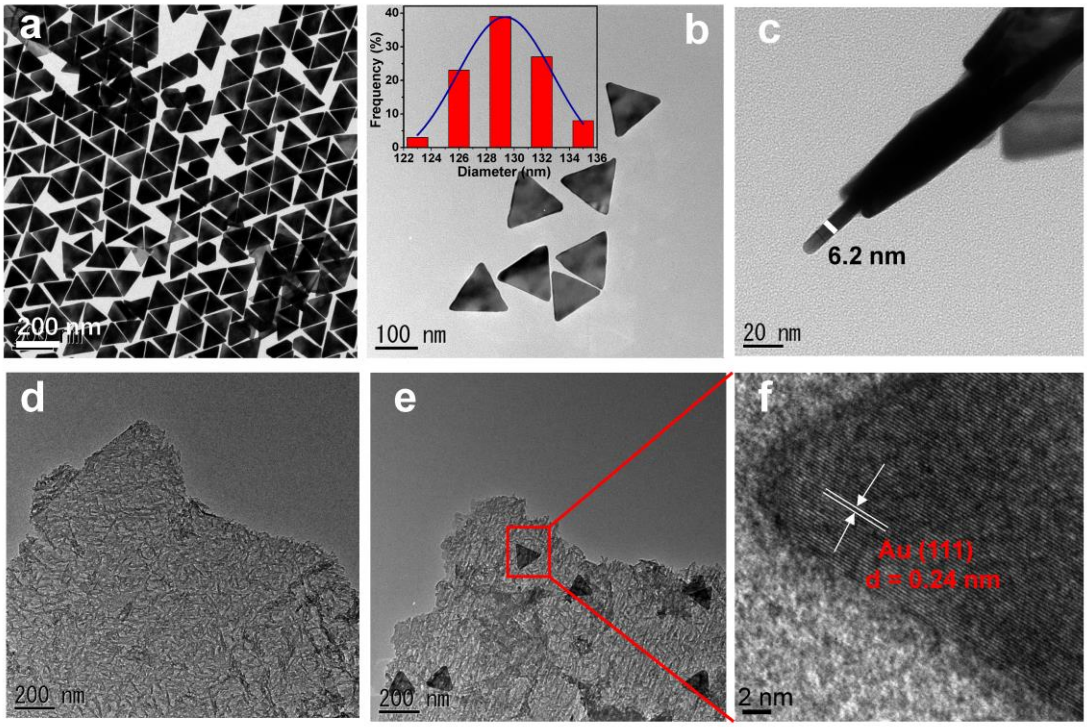


**Figure 1.** TEM image of Au TNPs (a-b) and g-$C_3N_4$ (d). The inset is size distribution of Au TNPs. TEM image of Au TNPs with vertical view (c). TEM and HRTEM images of Au TNPs/g-$C_3N_4$ (e-f).

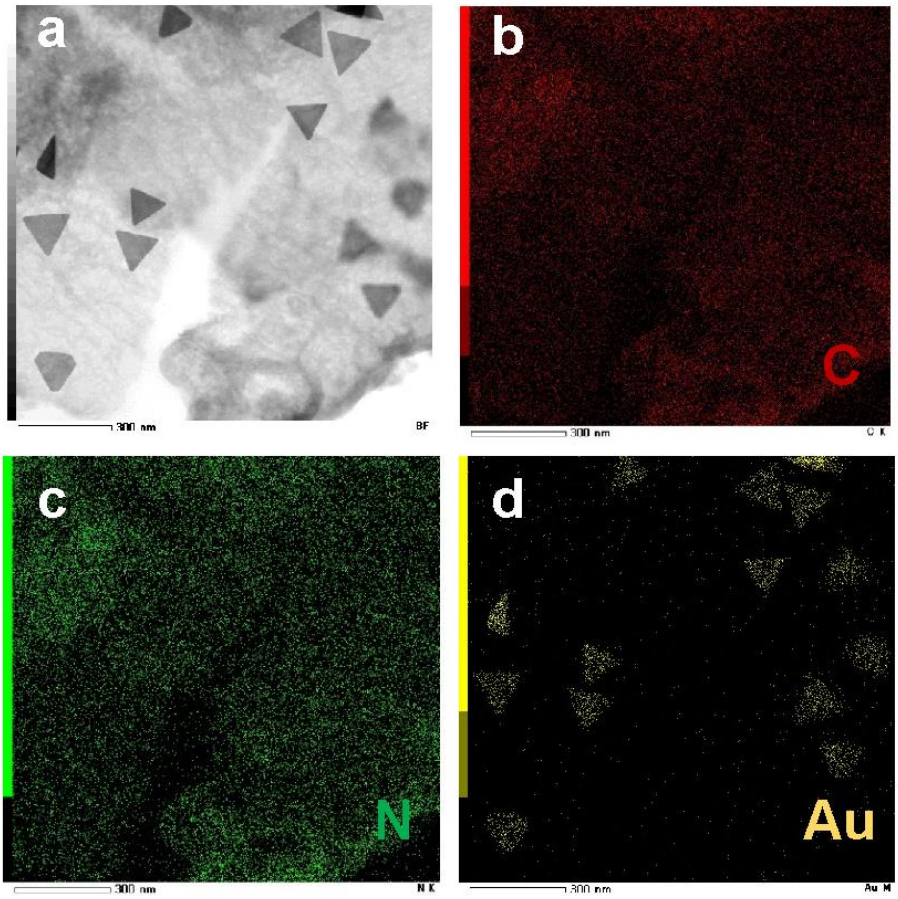


**Figure 2.** TEM image of Au TNPs/g-$C_3N_4$ (a). Elemental mappings of C (b), N (c) and Au (d). Scale bar: 300 nm.

The composition of the prepared g-$C_3N_4$ and all Au TNPs/g-$C_3N_4$ samples was confirmed by XRD patterns (Fig. 3a). The two distinct peaks of pure g-$C_3N_4$ observed around 13.0° and 27.5° are ascribed to the in-plane tri-s-triazine units and graphite-like stacking of the conjugated aromatic units, respectively, and can be indexed to (100) and (002) planes, respectively.[19] Compared with g-$C_3N_4$, Au TNPs/g-$C_3N_4$ samples represent diffraction peaks at 38.2°,44.3°,64.5°, and 77.5°, which can be assigned to the (111), (200), (220), and (311) planes of Au phase, respectively.[20] The XPS measurements were carried out to clarify the chemical state of surface elements of all samples as shown in Fig 3b-d. The C 1s spectrum exhibits two peaks at the binding energies of 288.5 and 286.1 eV, which are ascribed to N–C=N coordination in the framework and C–$NH_2$ on the edges of heptazine units, respectively.[21] The spectrum of N 1s can be deconvoluted into three peaks with the binding energies of 398.8, 399.5, and 401.2 eV, assigned to $sp^2$ N atoms in triazine ring (C–N=C), bridging N atoms (N($C_3$)), and N–H groups, respectively.[22] Two peaks at binding energies of 84.0 and

87.7 eV, corresponding to Au $4f_{7/2}$ and Au $4f_{5/2}$, respectively, are attributed to metallic gold $Au^0$.[23]

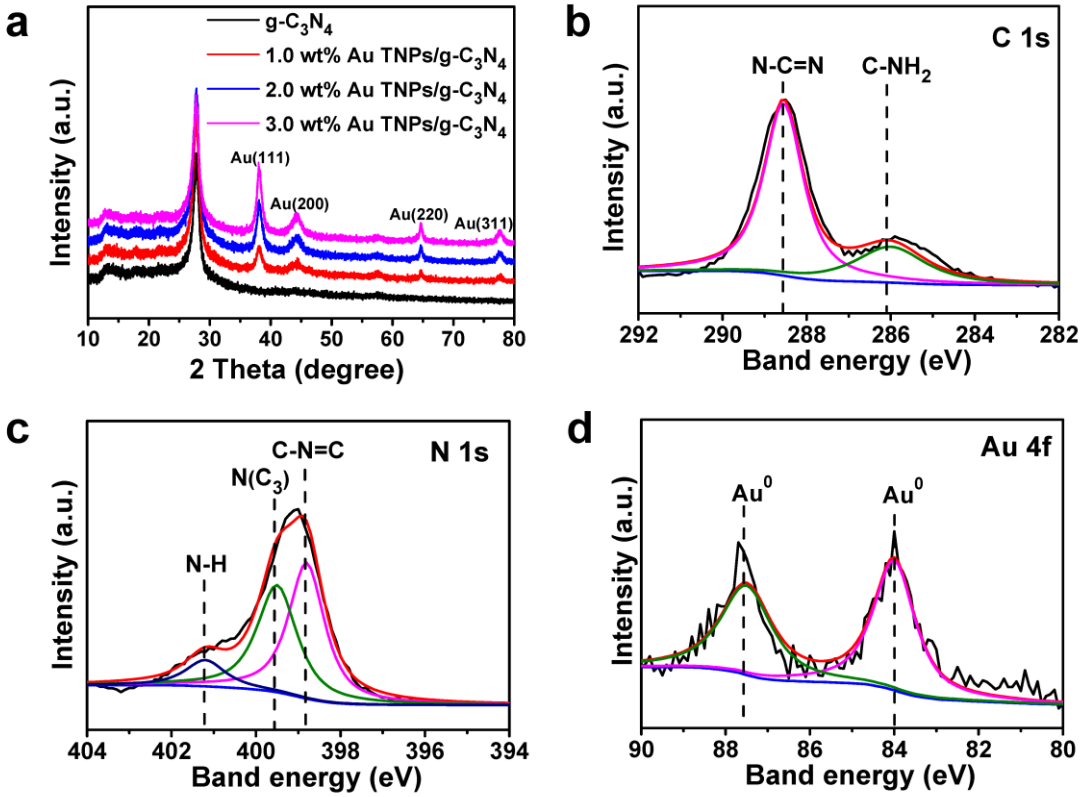


**Figure 3.** XRD patterns of g-$C_3N_4$ and Au TNPs/g-$C_3N_4$ (a). XPS spectra of C 1s (b), N 1s (c) and Au 4f (d) of Au TNPs/g-$C_3N_4$.

Fig. 4a shows the UV-Vis-NIR absorption spectra of Au TNPs. There are two SPR bands: the strong band at 1200 nm is assigned to the in-plane DSPR, while the other one at 700 nm is originated from in-plane MSPR. The DRS of g-$C_3N_4$ and Au TNPs/g-$C_3N_4$ were measured in the range from 300 to 1900 nm, as shown in Fig. 4b. The pure g-$C_3N_4$ only absorbs UV and Vis light with wavelengths $\lambda < 459$ nm due to the bandgap of 2.7 eV. After loading Au TNPs, all Au TNPs/g-$C_3N_4$ samples exhibit similar absorption thresholds owing to the band gap of g-$C_3N_4$. Further, a very broad Vis-NIR absorption centered at ca. 1200 nm is due to the in-plane DSPR of Au TNPs. With increasing the ratio of Au TNPs to g-$C_3N_4$ from 1.0 to 3.0 wt%, the absorption intensity in the Vis-NIR region increased gradually. The broad absorption in the NIR region provides a new opportunity for the utilization of long-wavelength solar spectrum.

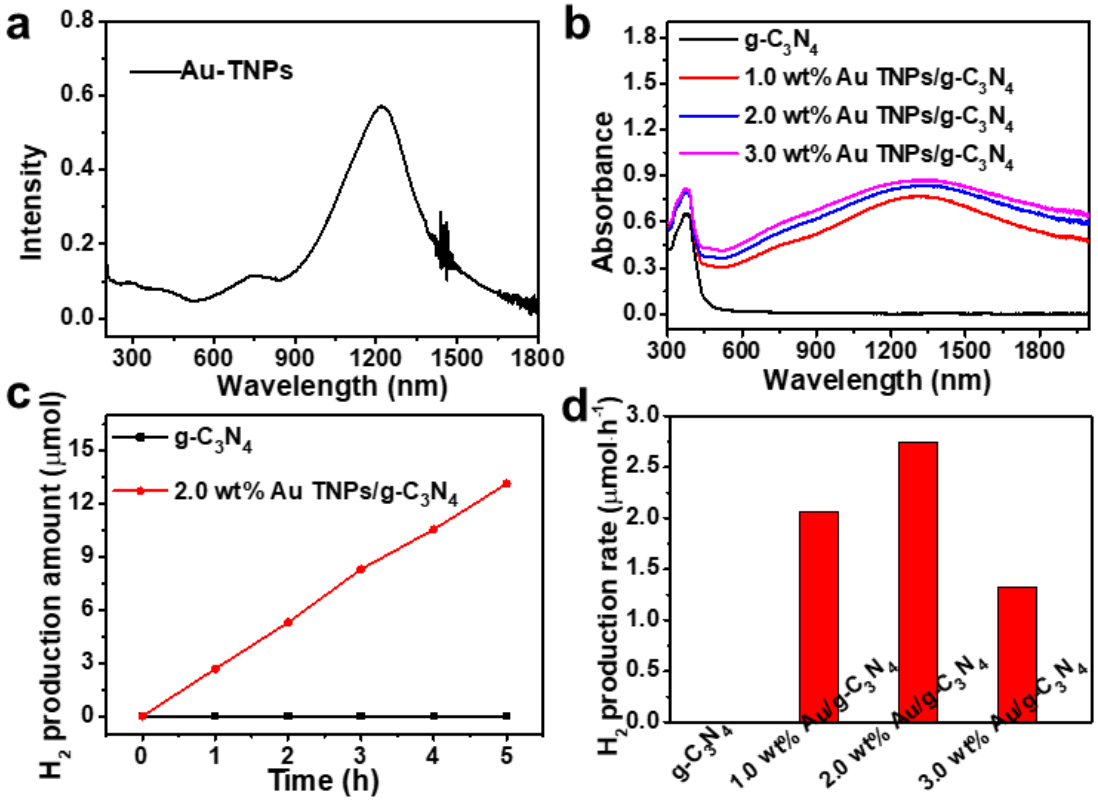


**Figure 4.** UV-Vis-NIR excitation spectrum of Au TNPs (a). UV-Vis-NIR diffuse reflectance spectra of g-$C_3N_4$ and Au TNPs/g-$C_3N_4$ (b). Time courses of photocatalytic $H_2$ production over g-$C_3N_4$ and Au TNPs/g-$C_3N_4$ under NIR light irradiation ($\lambda \geq 780$ nm) (c). Photocatalytic activities of Au TNPs/g-$C_3N_4$ with different loading amount of Au TNPs (d). Methanol was used as the sacrificial reagent to consume the plasmon-induced holes in TNPs.

The activity of Au TNPs/g-$C_3N_4$ was estimated by the photocatalytic $H_2$ production reaction under NIR light irradiation by using a 300 W Xenon lamp with a 780 nm cutoff filter. Methanol was used as the sacrificial reagent to consume the plasmon-induced holes in TNPs. As shown in Fig. 4c, pure g-$C_3N_4$ shows no photocatalytic $H_2$ production activity under NIR light irradiation which is in accordance with the DRS results, i.e., pure g-$C_3N_4$ cannot harvest light in the NIR region. However, once g-$C_3N_4$ is hybridized with Au TNPs, Au TNPs/g-$C_3N_4$ exhibits apparent photocatalytic $H_2$ production activity up to 53.4 μmol $g^{-1}$ $h^{-1}$. Obviously, the photocatalytic $H_2$ production activity of Au TNPs/g-$C_3N_4$ is derived from the Au TNPs. Fig. 4d shows the effect of the loading amount of Au TNPs on the photocatalytic activity of Au TNPs/g-$C_3N_4$ under NIR light irradiation. As can be seen, the optimum amount of Au TNPs in the present system is found to be 2.0 wt%. The decreased photocatalytic activity in overloaded 3.0

wt% Au TNPs/g-$C_3N_4$ can be ascribed to the aggregation of Au TNPs as in the TEM (Fig. 5), resulting in low efficiency in light harvesting.

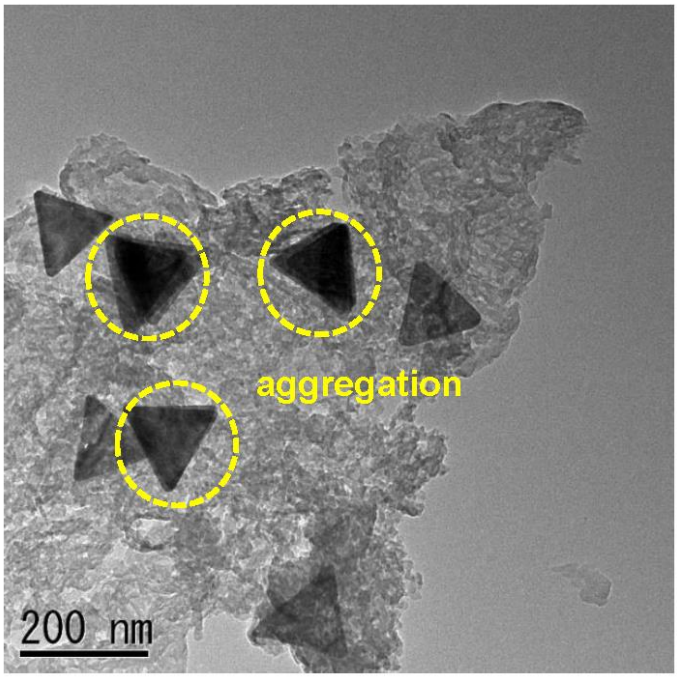


**Figure 5.** TEM image of 3.0 wt% Au TNPs/g-$C_3N_4$.

The surface of g-$C_3N_4$ for loading Au TNPs was also investigated (Fig. 6). The g-$C_3N_4$ in Fig. 6b was synthesized by the method developed in the present work which provides more flat surface than that of g-$C_3N_4$ prepared by a traditional method (Fig. 6a a).[24-26] It is clear that Au TNPs/g-$C_3N_4$ with flat surface of g-$C_3N_4$ showed better activity for photocatalytic $H_2$ production as in Fig. 6c, owing to the hot ET from Au TNPs to g-$C_3N_4$. After consecutive cycle experiments of Au TNPs/g-$C_3N_4$ (Fig. 7), the slight decrease in activity was confirmed. This decrease can be attributed to the decreased concentration of methanol and lack of fresh methanol since we evaluated every four hours without renewing the sacrificial agent.

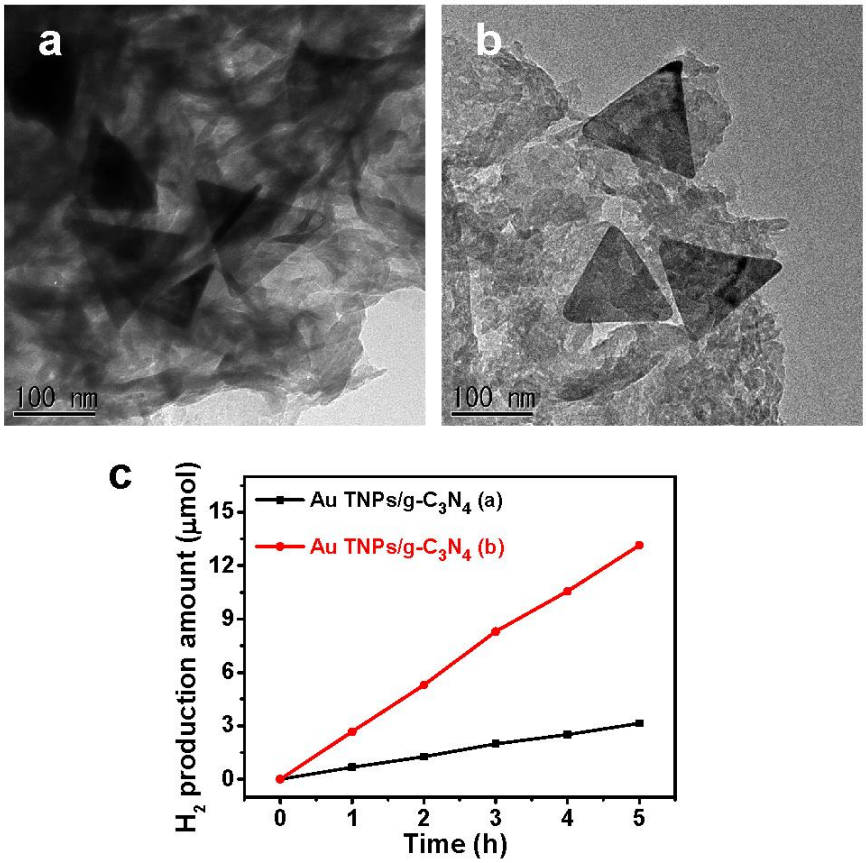


**Figure 6.** TEM images of Au TNPs loaded on g-$C_3N_4$ synthesized by a traditional method (a) and g-$C_3N_4$ prepared with better exfoliation (b). Time courses photocatalytic $H_2$ production over two samples under NIR light irradiation.

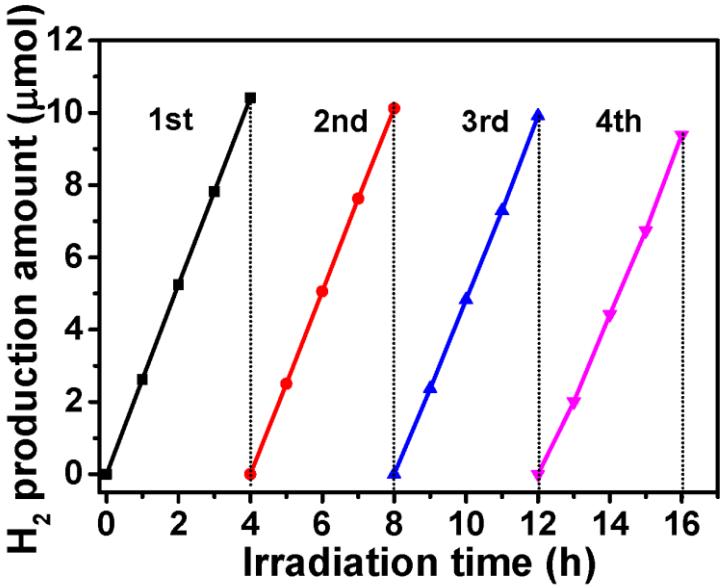


**Figure 7.** Recyclability of Au TNPs/g-$C_3N_4$ for photocatalytic $H_2$ production under NIR light irradiation.

The FDTD simulations were carried out to prove the enhancement of the electromagnetic field in the Au TNPs/g-$C_3N_4$ hybrid system.[27] The simulations results are shown in Fig. 8. During the calculation, the excitation laser beam was set to be perpendicular incidence (z-axis) and the electromagnetic filed was parallel (y-axis) to Au TNPs. Under perpendicular polarization, the Au TNPs/g-$C_3N_4$ shows stronger plasmon-induced electromagnetic field around the tip areas in NIR region than that of pure Au TNPs. Therefore, we can conclude that the relatively stronger hot spots around tips of Au TNPs/g-$C_3N_4$ would increase the density of plasmon-induced hot electrons and facilitate interfacial ET from Au TNPs to g-$C_3N_4$ which are responsible for efficient plasmon-induced photocatalytic $H_2$ generation.

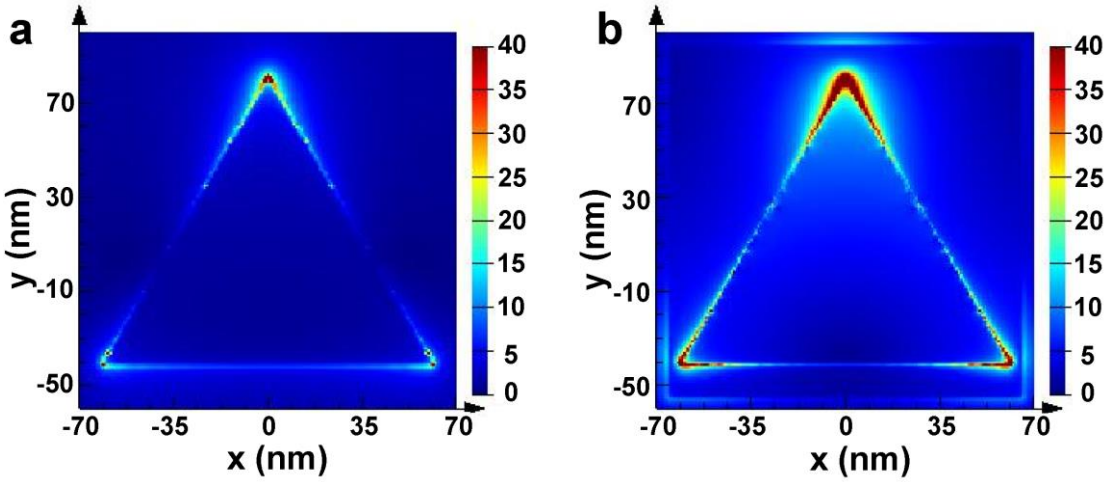


**Figure 8.** Electromagnetic field of Au TNPs (a) and Au TNPs/g-$C_3N_4$ (b). The color scale bar shows the relative increase in field enhancement $|E|/|E_0|$.

The plasmon-induced hot ET from Au TNPs to g-$C_3N_4$ after SPR excitation was examined by the femtosecond TA spectroscopy, a robust technique to analyze real time electron dynamics.[28-32] Fig. 9a-b show the TA spectra of bare Au TNPs and Au TNPs/g-$C_3N_4$ which were recorded from 850 to 1400 nm at several time delays after exciting Au TNPs with a 1100 nm laser pulse. For the bare Au TNPs, pulse laser excitation leads to the bleach of surface plasmon band in the range from 1030 to 1200 nm. The recovery of the plasmon bleach reflects the energy dissipation of the plasmon-induced hot electrons.[33] Two positive TA around the bleach were also observed, simultaneously.[34, 35] One positive TA in the range of 850-1030 nm is due to thermal redistribution of electrons below the Fermi level.[36] These electrons cannot be associated with plasmon-induced hot electrons. The other positive TA in the range of 1200-1400 nm is attributed to the absorption of hot electrons of the plasmon band.[36] For the Au TNPs/g-$C_3N_4$, only

the bleach of surface plasmon band is observed and no positive TA can be detected, indicating that hot electrons of the plasmon band transfer from Au TNPs to g-$C_3N_4$ after the SPR excitation within 1 ps.[31] It is known that the hot electrons of gold nanoparticles after SPR excitation with a non-Fermi distribution relax through electron–electron (<100 fs), electron-phonon (1-10 ps), and phonon-phonon scatterings (~100 ps).[37] Note that the phonon-phonon scattering cannot be separately analyzed since it appears to be superimposed on the overall TA signal.[38] The dynamics of the plasmon band bleach recovery is biexponential with two time constants of $\tau_1$ and $\tau_2$ as shown in Fig. 9c.[39] The fast relaxation on a time scale of a few picoseconds $\tau_1$ is attributed to the electron-phonon scattering as indicated above.[36] The recovery on a longer time scale of hundreds of picoseconds $\tau_2$ is attributed to the charge recombination process.[38] The recovery profiles of TA bleach (1030-1200 nm) were fitted with the lifetimes $\tau_1$ = 4.6 ps and $\tau_2$ = 214 ps for Au TNPs, while $\tau_1$ = 5.1 ps and $\tau_2$ = 497 ps for the Au TNPs/g-$C_3N_4$. The almost equivalent $\tau_1$ means that the electron-phonon scattering is dominant in both Au TNPs and Au TNPs/g-$C_3N_4$. The longer $\tau_2$ of Au TNPs/g-$C_3N_4$ indicates that the plasmon-induced electrons and holes separately located in g-$C_3N_4$ and Au TNPs, respectively, after hot ET from Au TNPs to g-$C_3N_4$ which overcomes the interfacial Schottky barrier, leading to separation of charge carriers with a longer lifetime. The slow recombination of electrons and holes give rise to photocatalytic activity for $H_2$ production in Au TNPs/g-$C_3N_4$.

The proposed mechanism of the plasmon-induced hot electron generation and charge separation (CS) over Au TNPs/g-$C_3N_4$ is illustrated in Fig. 9d. Upon NIR excitation, the electrons in Au TNPs are promoted to the excited states, heating up the electrons. The increase in electron temperature causes a TA bleach of the broadened plasmonic band, generating the hot electrons and holes. g-$C_3N_4$ cannot be excited to generate charge carriers since it has no absorption in NIR region as shown in Fig. 4b. For the Au TNPs, PL of Au TNPs is mainly due to the radiative decay from DSPR. While Au TNPs are combined with g-$C_3N_4$, the plasmon-induced hot ET from Au TNPs to g-$C_3N_4$ competes with the DSPR radiative decay. Plasmon-induced electromagnetic field is formed to increase the yield of hot electrons with higher potential energy than $\varphi_{SB}$, leading to efficient ET to the CB of g-$C_3N_4$ and the Schottky barrier at the interface can also help the electrons to be accumulated in the CB of g-$C_3N_4$. Subsequently, the injected electrons move to the active sites of g-$C_3N_4$ and the holes remained in the Au

TNPs are consumed by methanol, leading to long lifetimes of electrons in g-$C_3N_4$, which reduce $H^+$ to generate $H_2$ efficiently. Therefore, hot ET benefits the slow recombination of electrons and holes, prolonging the lifetime of electrons and playing a crucial role in photocatalytic $H_2$ production.

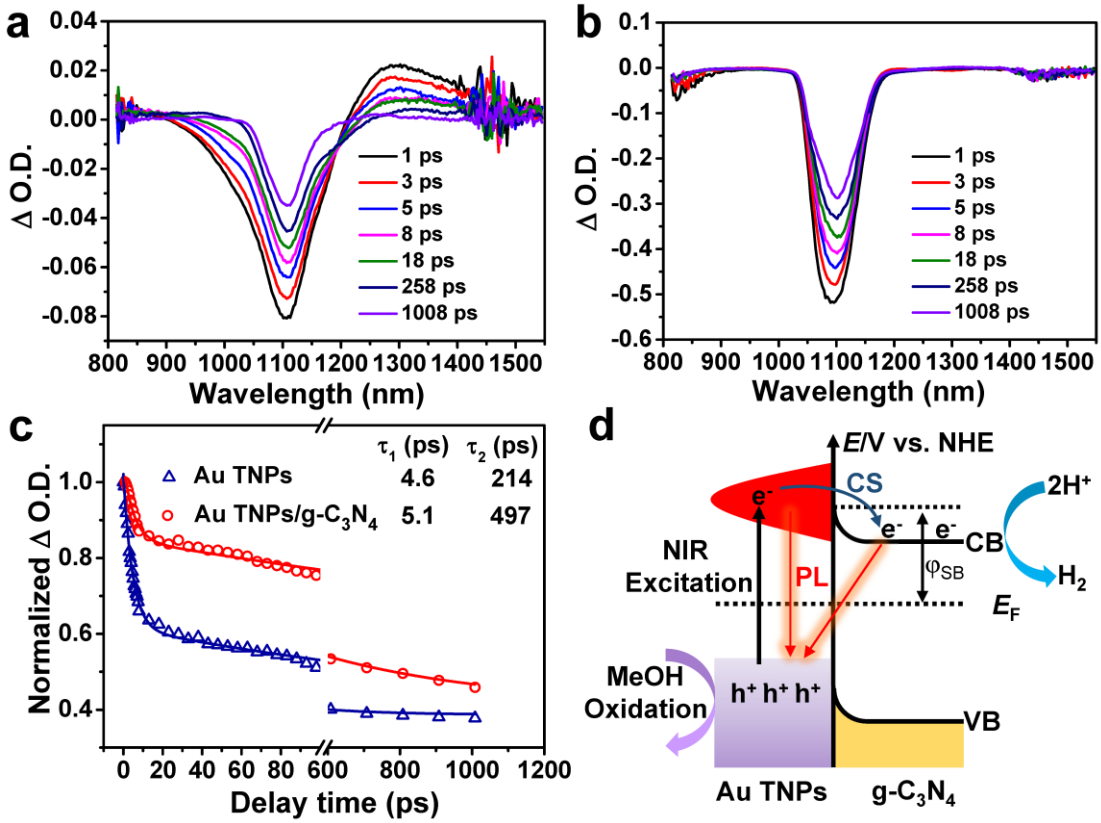


**Figure 9.** Transient absorption (TA) spectra of Au TNPs (a) and Au TNPs/g-$C_3N_4$ (b). Normalized time profiles of transient absorption at 1100 nm for Au TNPs and Au TNPs/g-$C_3N_4$ (c). Bold lines were fitting curves obtained by two exponential decays. Schematic illustration of the plasmon-induced hot ET from Au TNPs to g-$C_3N_4$ (d). The photoluminescence (PL), charge separation (CS), Fermi level ($E_F$), and Schottky barrier ($\varphi_{SB}$).

## 4. Conclusion

In summary, Au TNPs/g-$C_3N_4$ were prepared for photocatalytic $H_2$ production under NIR light irradiation. The FDTD results show that the enhanced electromagnetic field in Au TNPs/g-$C_3N_4$ increases the density of plasmon-induced hot electrons and facilitates the interfacial ET from Au TNPs to g-$C_3N_4$. Time-resolved TA measurements revealed that plasmon-induced hot ET from Au TNPs to g-$C_3N_4$. The CS in Au TNPs/g-$C_3N_4$ retarded the recombination of hot electrons and holes and prolonged the lifetime

of electrons. This work gives a noteworthy example for the utilization of NIR energy and provides a strategy to study the plasmon-induced hot ET in noble metal/semiconductor hybrid.

## 5. References


1. A. Fujishima and K. Honda, *Nature*, 1972, **238**, 37.
2. Y. Wang, H. Suzuki, J. Xie, O. Tomita, D. J. Martin, M. Higashi, D. Kong, R. Abe and J. Tang, *Chem. Rev.*, 2018, **118**, 5201-5241.
3. W. Li, A. Elzatahry, D. Aldhayan and D. Zhao, *Chem. Soc. Rev.*, 2018, **47**, 8203-8237.
4. Y. Ma, X. Wang, Y. Jia, X. Chen, H. Han and C. Li, *Chem. Rev.*, 2014, **114**, 9987-10043.
5. S. J. A. Moniz, S. A. Shevlin, D. J. Martin, Z.-X. Guo and J. Tang, *Energy Environ. Sci.*, 2015, **8**, 731-759.
6. X. Wang, K. Maeda, A. Thomas, K. Takanabe, G. Xin, J. M. Carlsson, K. Domen and M. Antonietti, *Nat. Mater.*, 2009, **8**, 76-80.
7. Y. Wang, X. Wang and M. Antonietti, *Angew. Chem. Int. Ed.*, 2012, **51**, 68-89.
8. J. Zhang, Y. Chen and X. Wang, *Energy Environ. Sci.*, 2015, **8**, 3092-3108.
9. S. Linic, P. Christopher and D. B. Ingram, *Nat. Mater.*, 2011, **10**, 911-921.
10. Y. Tian and T. Tatsuma, *J. Am. Chem. Soc.*, 2005, **127**, 7632-7637.
11. E. Kowalska, O. O. Mahaney, R. Abe and B. Ohtani, *Phys. Chem. Chem. Phys.*, 2010, **12**, 2344-2355.
12. K. Qian, B. C. Sweeny, A. C. Johnston-Peck, W. Niu, J. O. Graham, J. S. DuChene, J. Qiu, Y. C. Wang, M. H. Engelhard, D. Su, E. A. Stach and W. D. Wei, *J. Am. Chem. Soc.*, 2014, **136**, 9842-9845.
13. X. Ye, L. Jin, H. Caglayan, J. Chen, G. Xing, C. Zheng, V. Doan-Nguyen, Y. Kang, N. Engheta, C. R. Kagan and C. B. Murray, *ACS Nano*, 2012, **6**, 2804-2817.
14. T. H. Ha, H. J. Koo and B. H. Chung, *J. Phys. Chem. C*, 2007, **111**, 1123-1130.
15. L. Scarabelli, M. Coronado-Puchau, J. J. Giner-Casares, J. Langer and L. M. Liz-Marzán, *ACS Nano*, 2014, **8**, 5833-5842.
16. Z. Lou, M. Fujitsuka and T. Majima, *ACS Nano*, 2016, **10**, 6299-6305.
17. Y. C. Pu, G. Wang, K. D. Chang, Y. Ling, Y. K. Lin, B. C. Fitzmorris, C. M. Liu, X. Lu, Y. Tong, J. Z. Zhang, Y. J. Hsu and Y. Li, *Nano Lett.*, 2013, **13**, 3817-3823.

18. X. Cai, M. Zhu, O. A. Elbanna, M. Fujitsuka, S. Kim, L. Mao, J. Zhang and T. Majima, *ACS Catal.*, 2018, **8**, 122-131.
19. S. Martha, A. Nashim and K. M. Parida, *J. Mater. Chem. A*, 2013, **1**, 7816-7824.
20. Z. Li, Y. Xin, Z. Zhang, H. Wu and P. Wang, *Sci. Rep.*, 2015, **5**, 10617.
21. X. Wang, J. Cheng, H. Yu and J. Yu, *Dalton Trans.*, 2017, **46**, 6417-6424.
22. Y. Li, H. Zhang, P. Liu, D. Wang, Y. Li and H. Zhao, *Small*, 2013, **9**, 3336-3344.
23. L. Wang, X. Zhou, N. T. Nguyen and P. Schmuki, *ChemSusChem*, 2015, **8**, 618-622.
24. J. Chen, S. Shen, P. Guo, M. Wang, P. Wu, X. Wang and L. Guo, *Appl. Catal. B: Environ.*, 2014, **152-153**, 335-341.
25. M. Y. Xing, B. X. Yang, H. Yu, B. Z. Tian, S. Bagwasi, J. L. Zhang and X. Q. Gong, *J. Phys. Chem. Lett.*, 2013, **4**, 3910-3917.
26. Y. Li, R. Jin, X. Fang, Y. Yang, M. Yang, X. Liu, Y. Xing and S. Song, *J Hazard. Mater.*, 2016, **313**, 219-228.
27. P. Zhang, M. Fujitsuka and T. Majima, *Nanoscale*, 2017, **9**, 1520-1526.
28. R. Godin, Y. Wang, M. A. Zwijnenburg, J. Tang and J. R. Durrant, *J. Am. Chem. Soc.*, 2017, **139**, 5216-5224.
29. K. L. Corp and C. W. Schlenker, *J. Am. Chem. Soc.*, 2017, **139**, 7904-7912.
30. M. Zhu, S. Kim, L. Mao, M. Fujitsuka, J. Zhang, X. Wang and T. Majima, *J. Am. Chem. Soc.*, 2017, **139**, 13234-13242.
31. A. Furube, L. Du, K. Hara, R. Katoh and M. Tachiya, *J. Am. Chem. Soc.*, 2007, **129**, 14852-14853.
32. P. K. Jain, W. Qian and M. A. El-Sayed, *J. Am. Chem. Soc.*, 2006, **128**, 2426-2433.
33. S. K. Eah, H. M. Jaeger, N. F. Scherer, X. M. Lin and G. P. Wiederrecht, *Chem. Phys. Lett.*, 2004, **386**, 390-395.
34. S. Link, C. Burda, Z. L. Wang and M. A. El-Sayed, *J. Chem. Phys.*, 1999, **111**, 1255-1264.
35. T. S. Ahmadi, S. L. Logunov and M. A. El-Sayed, *J. Phys. Chem.*, 1996, **100**, 8053-8056.
36. S. L. Logunov, T. S. Ahmadi, M. A. El-Sayed, J. T. Khoury and R. L. Whetten, *J. Phys. Chem. B*, 1997, **101**, 3713-3719.
37. C. Clavero, *Nat. Photonics*, 2014, **8**, 95-103.
38. H. Huang, L. Zhang, Z. Lv, R. Long, C. Zhang, Y. Lin, K. Wei, C. Wang, L. Chen,

Z. Y. Li, Q. Zhang, Y. Luo and Y. Xiong, *J. Am. Chem. Soc.*, 2016, **138**, 6822-6828.

39. P. V. Kamat and B. Shanghavi, *J. Phys.Chem. B*, 1997, **101**, 7675-7679.

# Chapter 3. Exfoliated $Mo_2C$ Nanosheets Hybridized on CdS with Fast Electron Transfer for Efficient Photocatalytic $H_2$ Production under Visible Light Irradiation

## 1. Introduction

Hydrogen evolution reaction (HER) by water splitting is a potential method as a sustainable strategy to overcome the global energy crisis of the past few decades, because $H_2$ fuel is clean and renewable with high energy density.[1] Semiconductor photocatalysts harvesting solar light to promote energy conversion have been extensively studied for photocatalytic HER. In particular, photocatalysts with a Vis-light-response are desirable since solar light consists of approximately 48% Vis light. [2, 3] Among such photocatalysts, CdS is one of the promising photocatalytic materials for Vis-light-driven HER, because it can be easily synthesized with low cost and has a conduction band edge more negative than the reduction potential of $H_2O/H_2$.[4] However, bare CdS shows poor photocatalytic efficiency resulting from the rapid recombination of photogenerated electron-hole pairs. Various methods have been exploited to realize higher photocatalytic activity from CdS-based photocatalysts.[5] Noble metals, such as Pt with the highest work function, have been primarily used as a cocatalyst for photocatalytic HER, because Pt not only reduces the recombination of photogenerated charge carriers but also has low overpotential toward the reaction of protons generating $H_2$.[6] Nevertheless, high cost and scarcity restrict its widespread applications. Therefore, an investigation of high-performance cocatalysts based on earth-abundant elements is highly imperative.[7]

Nowadays, materials such as carbides,[8] sulphides,[9] and phosphides[10] of nonprecious transition metals (Fe, Co, Ni, Mo, and W) have been extensively investigated to replace Pt as cocatalysts for the HER. In particular, MXenes (refer to transition metal carbides, carbonitrides, and nitrides), a novel family of two-dimensional (2D) materials which have unusual electronic, thermoelectric, mechanical, and optical properties, have attracted much attention since their discovery in 2011.[11-13] The versatile chemical and physical properties of MXenes allow for their applications including energy storage, electromagnetic interference shielding, reinforcement for composites, water purification, gas- and biosensors, and catalysis.[14, 15] Molybdenum nitride acting as cocatalysts has been studied to show good performance for hydrogen

production.[16-18] Among them, transition metal carbides (TMCs), such as molybdenum carbide ($Mo_2C$), have been reported to be active in noble metal-catalyzed reactions and electrocatalytic HER on account of their d-band electronic structure and catalytic properties similar to those of Pt-group metals.[19-21]

Nevertheless, uncontrollable sintering/aggregation or excessive growth of carbon on the surface of $Mo_2C$ is often inevitable during the thermolysis process at ultrahigh temperatures (>1000 K) to overcome thermodynamic and kinetic barriers when carbon atoms are incorporated into the metal lattice, resulting in a low density of exposed active sites and poor activity. It is recognized that large planar area and low thickness lead to high specific surface area that facilitates charge transfer in a shorter distance and offers more active sites for surface reactions. Many efforts have been devoted to increase the number of active sites by optimizing various morphologies of $Mo_2C$, such as nanoparticles,[22] nanotubes,[23] nanowires,[24] and 2D MXenes.[25] Except for the pyrolysis method, chemical vapor deposition (CVD) is a well-known technique to synthesize nanosheets structure materials.[26] However, the above synthesis method for $Mo_2C$ nanosheets is always complicated, high energy consuming, and a low yield rate, which imply difficulty in wide use. Recently, exfoliation has been recognized as an efficient method to prepare materials with a monolayer or few-layers structure that provides more edge sites that in turn release more active sites for reactions,[27, 28] Although chemical exfoliation,[29, 30] a selective chemical etching method, can be used in liquids, this method is time-consuming, extremely sensitive to the environment, and incompatible with most of solvents. On the other hand, liquid-phase ultrasonic exfoliation, a practical and efficient method to form layered structures, is insensitive to the environment and can be potentially scaled up to provide large quantities of exfoliated nanosheets.[31, 32]

In the present work, exfoliated $Mo_2C$ nanosheets ($Mo_2C$) with a thickness of 20 nm were obtained by liquid-phase ultrasonic exfoliation in isopropanol solvent for the first time. CdS nanoparticles with a diameter of 10 nm (CdS) were hybridized with $Mo_2C$ (1-5 wt%) as a cocatalyst to form the composite $Mo_2C$/CdS as shown in scheme 1, which showed efficient photocatalytic HER under Vis light irradiation. The activity is 6-, 16-, and 4-folds as high as those for bulk $Mo_2C$/CdS, bare CdS, and Pt/CdS, respectively. Such high activity can be ascribed to nanosheet structure of $Mo_2C$ with more exposed active sites, since the photogenerated electrons transfer rapidly from CdS

to $Mo_2C$ and to the active sites with shortened migration distance, leading to efficient charge separation. Various measurements including femtosecond TDR measurements supported efficient charge separation and electron injection in $Mo_2C$/CdS.

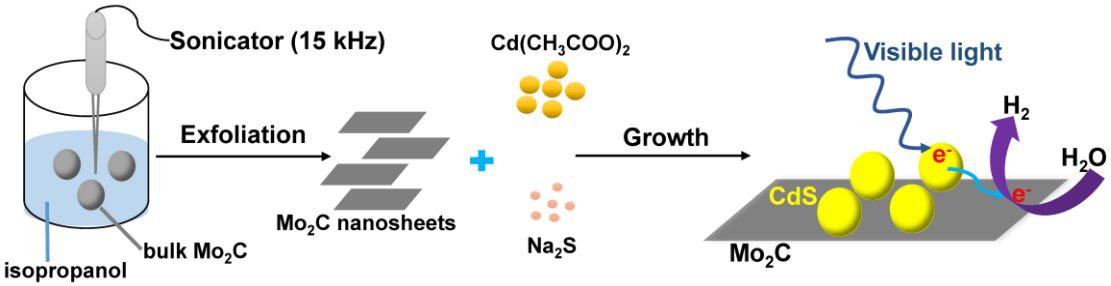


**Scheme 1.** Illustration for synthesizing exfoliated $Mo_2C$ nansheets and $Mo_2C$/CdS.

## 2. Experimental Section

**Chemicals and reagents.** Cadmium acetate ($Cd(CH_3COO)_2$), sodium sulfide ($Na_2S$), molybdenum carbide ($Mo_2C$), lactic acid (LA), dimethylformamide (DMF), isopropanol (IPA), ethanol, chloroplatinic acid hexahydrate ($H_2PtCl_6•6H_2O$), and sodium sulfate ($Na_2SO_4$) were purchased from Wako or Sigma-Aldrich, and they were used without further purification.

**Exfoliation of $Mo_2C$ nanosheets.** 30 mg of the bulk $Mo_2C$ precursor was put into a 50 mL glass bottle. Next, 30 mL of isopropanol was added as the exfoliation and dispersion solvent. The mixture, placed in an ice-bath, was sonicated for 8 h by using a tip sonicator (Misonix XL-2000) at 15 kHz. Upon sonication, the suspension of bulk $Mo_2C$ became homogeneously black in color. The suspension was centrifuged at 2 krpm for 20 min, and the 2/3 portions of the supernatants were carefully collected using a pipette. After several repetitions of such a collection, the supernatants were centrifuged at 13 krpm for 40 min to remove IPA. The obtained $Mo_2C$ was washed with ethanol and freeze-dried. $Mo_2C$ was dispersed in ethanol for further use with a concentration of 1 mg/mL.

**Synthesis of $Mo_2C$/CdS.** $Mo_2C$/CdS was prepared by the precipitation method. For the synthesis of 3 wt% $Mo_2C$/CdS, 38 mg of $Cd(CH_3COO)_2$ was dissolved in 12 mL of DI water and 11 mg of $Na_2S$ was dissolved in 4 mL of DI water separately. 0.1 mL of $Mo_2C$ suspension, prepared as detailed above, was added into the $Cd(CH_3COO)_2$ solution and was sonicated for 1 h. Next, the $Na_2S$ solution was added dropwise into

the above solution, and the mixture was vigorously stirred. The precipitate was centrifuged and washed by DI water and ethanol several times, and then freeze-dried. Other $Mo_2C$/CdSs with different ratios of $Mo_2C$ were prepared using the same method by adding different amounts of $Mo_2C$. Pure CdS was synthesized from $Cd(CH_3COO)_2$ and $Na_2S$. For the purpose of comparison, $Mo_2C$/CdS was also prepared under ultrasonication. First, 100 mg of CdS was dispersed in 30 mL of DMF and ultrasonicated for 30 min at room temperature. Following this, the $Mo_2C$ suspension was added into the above solution, and the mixture was ultrasonicated for 2 h. The mixture was collected by centrifugation and washed with ethanol several times, and then freeze-dried.

**Synthesis of Pt/CdS.** Pt/CdS was prepared using the photodeposition method. 50 mg of CdS nanoparticles were dispersed into 50 mL of DI water followed by ultrasonication for 30 min. Next, 4.2 mL of $H_2PtCl_6$•$6H_2O$ (1 g/1 L) was added into the above suspension and the mixture was kept under ultrasonication for 1 h to deposit Pt ions onto CdS. After that, the mixture was irradiated using a 365 nm LED lamp to reduce Pt ions to Pt nanoparticles. Finally, the solid sample was collected by centrifugation, and was washed with ethanol and DI water several times, and freeze-dried.

**Photocatalytic HER**. Typically, 4.0 mg of CdS-based photocatalyst was dispersed in 5.0 mL aqueous solution containing 20 vol% LA as a sacrificial electron donor. The suspension was irradiated by a Xenon lamp and generated $H_2$ was detected with a gas chromatograph as in Chapter 1. The AQE for HER at different wavelengths of the monochromatic light obtained by using band-pass filters. Experiment conditions: 4.0 mg catalyst was dispersed in 5.0 mL aqueous solution containing 20 vol% LA. The light intensities at $\lambda$ = 420, 440, 460, 480, 500, 520, 540, and 560 nm were 3.63, 3.65, 4.05, 3.83, 3.64, 3.72, 4.03, and 3.77 mW $cm^{-2}$, respectively. The irradiation area was 0.2 $cm^2$.

**Photoelectrochemical measurements.** Photoelectrochemical measurements were carried out as in Chapter 1.

**Characterization.** All samples used in the present work were characterized by XRD, TEM, EDS, UV-Vis-NIR spectrometer, XPS, and BET, as in Chapter 1 and 2.X Atomic force microscopy (AFM, SII, SPI3800/SPA400) was used for study sample structure.

**Femtosecond time-resolved diffuse reflectance measurements.** The femtosecond diffuse reflectance spectra were measured by the pump and probe method as in Chapter 1. In this chapter, the sample was excited with 420 nm laser light.

## 3. Results and Discussion

The morphologies of CdS, commercial bulk $Mo_2C$, and $Mo_2C$ were studied by means of TEM as shown in Fig. 1. High-resolution TEM (HRTEM) was used to study the interface between CdS and $Mo_2C$. It is clear that commercial bulk $Mo_2C$ possesses a 3D particle structure with a size of several micrometers (Fig. 1a). After ultrasonic exfoliation, bulk $Mo_2C$ was successfully transformed to $Mo_2C$ as shown in Fig. 1b. During the liquid-phase ultrasonic exfoliation process, the hydrodynamic force from high-energy liquid jets at the edge sites of the bulk materials is enough to overcome the interlayer van der Waals attraction, allowing efficient exfoliation transforming to nanosheets (Fig. 2a-c).[33] The HRTEM image of $Mo_2C$ shows two types of ordered lattice fringe spacings of 0.15 and 0.26 nm, corresponding to the (110) and (100) planes of $Mo_2C$, respectively (Fig. 1d).[34] CdS with particle size of ca. 10 nm shows slight aggregation (Fig. 1c). The lattice fringes with a spacing of 0.33 nm, which can be indexed to the (111) plane of CdS, were observed (Fig. 1e). The average thickness of $Mo_2C$ was estimated to be approximately 20 nm by AFM measurements as shown in Fig. 2d-e. This decrease in thickness is expected to be beneficial for the transfer of photogenerated electrons in a shorter distance and increase in the number of active sites. Fig. 1f shows a TEM image of $Mo_2C$/CdS with the close contact between CdS and $Mo_2C$. Fig. 1g clearly reveals the different lattice fringe spacings which belong to the CdS and $Mo_2C$ in $Mo_2C$/CdS, implying the formation of heterointerface between CdS and $Mo_2C$. Element mapping was further carried out to investigate the composition and spatial distribution of $Mo_2C$/CdS. EDS confirms the existence of Cd, S, and Mo as presented in Figs. 1h-j, demonstrating the successful hybridization of $Mo_2C$ on CdS. The BET surface areas of CdS and $Mo_2C$/CdS were measured by means of $N_2$ adsorption−desorption isotherms as shown in Fig. 3. The BET surface area of 3.0 wt% $Mo_2C$/CdS is calculated to be 173 $m^2 g^{-1}$ which is larger than that of bare CdS (127 $m^2 g^{-1}$), suggesting that exfoliated $Mo_2C$ nanosheets can be a useful platform for the growth of CdS nanoparticles to suppress aggregation. It is well known that high surface area is beneficial to surface reactions by offering more active sites for reactant molecules and

promoting mass transport during the photocatalytic process.

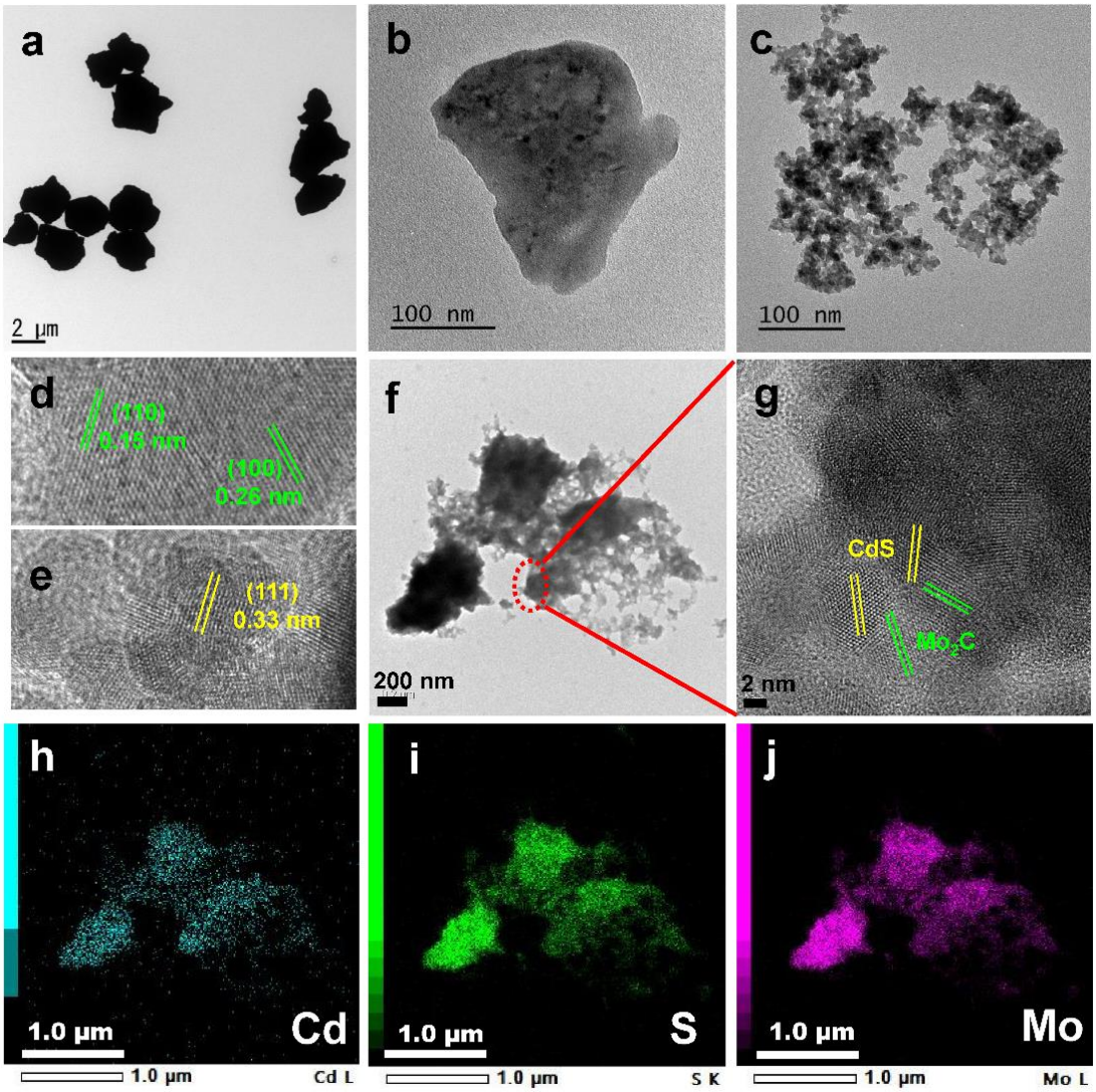


**Figure 1.** TEM images of commercial bulk $Mo_2C$ (a), $Mo_2C$ after liquid-phase ultrasonic exfoliation (b), CdS (c), and 3 wt% $Mo_2C$/CdS (f). HRTEM images of CdS (d), $Mo_2C$ (e), and selected area in (f). Element mappings of Cd (h), S (i), Mo (j) over the 3 wt% $Mo_2C$/CdS.

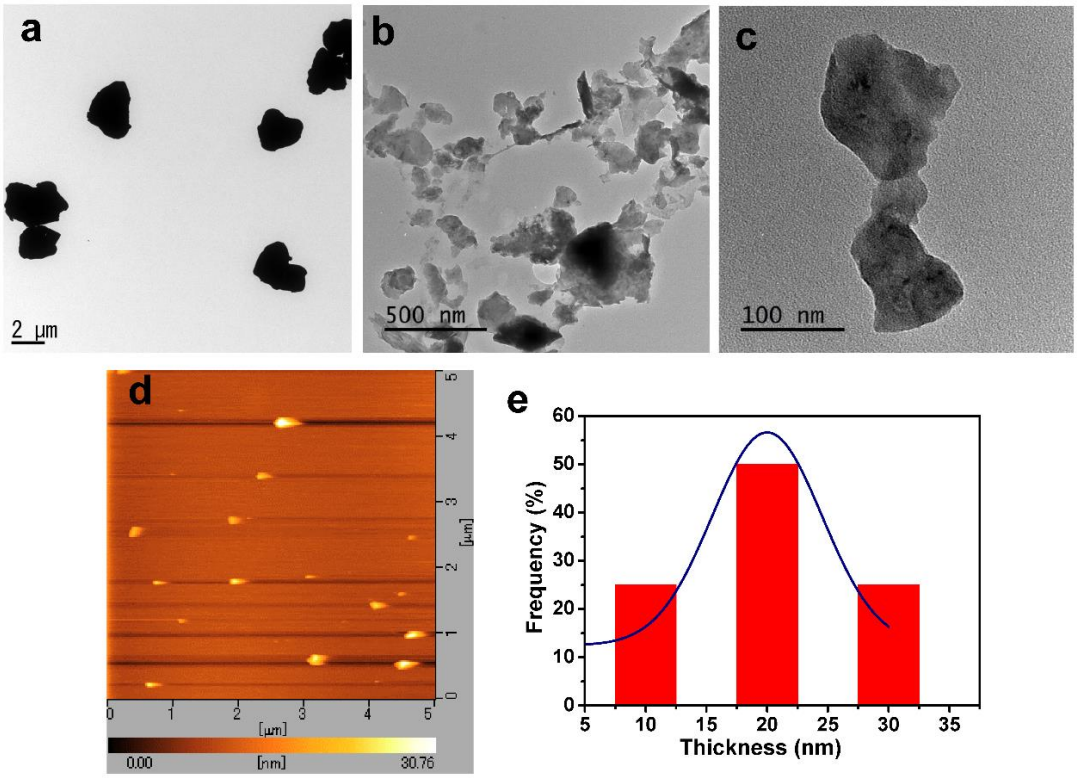


**Figure 2.** TEM images of commercial bulk $Mo_2C$ (a) and $Mo_2C$ nanosheets after liquid-phase ultrasonic exfoliation (b)-(c). AFM image of $Mo_2C$ nanosheets (d) and thickness distribution of $Mo_2C$ nanosheets (e).

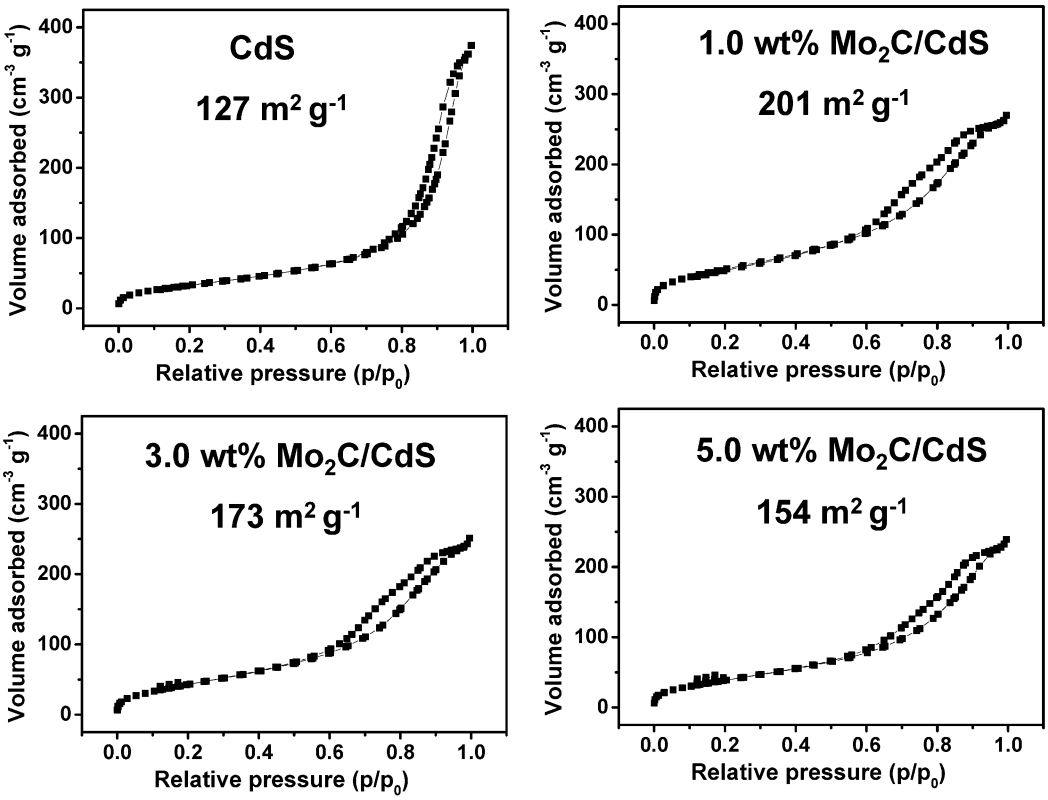


**Figure 3.** Nitrogen adsorption−desorption isotherms and BET surface areas of CdS and $Mo_2C$/CdS.

The phase identifications of prepared CdS and $Mo_2C$/CdS were carried out by XRD. Fig. 4a shows the XRD patterns of bare CdS and $Mo_2C$/CdS with different ratios of $Mo_2C$. For bare CdS, characteristic peaks at 26.6°, 44.0°, and 52.1° were observed to be assigned to (111), (220), and (311) planes of CdS (JCPDS No. 10-454), respectively.[35] The characteristic peaks at 34.4°, 37.9°, 39.3°, and 61.6° are assigned to (100), (002), (101), and (110) planes of the hexagonal β-$Mo_2C$ (JCPDS No. 35-0787), respectively.[36] After the hybridization of CdS and $Mo_2C$, $Mo_2C$/CdS still maintains the characteristic peaks of CdS. With an increase in the ratio of $Mo_2C$, the characteristic peaks of $Mo_2C$ become distinct, and there is a slight intensity decrease of the characteristic peaks of CdS, indicating that the excessive $Mo_2C$ may block X-ray irradiation and coherent scattering.[37] The UV-Vis-NIR absorption of CdS, $Mo_2C$, and $Mo_2C$/CdS was studied by UV-vis-NIR diffuse reflectance spectra (DRS) as shown in Fig. 4b. Bare CdS exhibits a strong absorption with wavelengths shorter than 520 nm due to its intrinsic band gap. Bare $Mo_2C$ shows broad and strong absorption in the region of 300–800 nm owing to the black color of $Mo_2C$.[38, 39] For $Mo_2C$/CdS, an increased absorption over the wavelength range of 550–800 nm was observed compared

with bare CdS. With increasing content of $Mo_2C$, the absorption in the Vis-NIR region increased gradually.

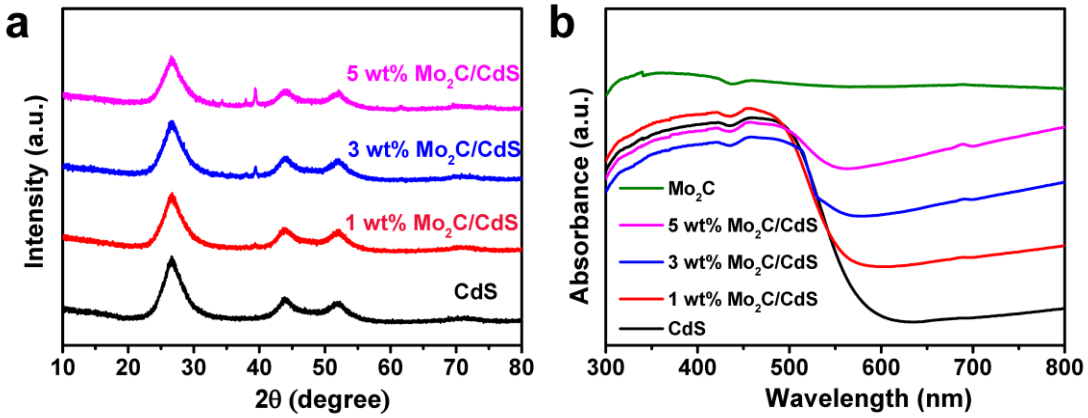


**Figure 4.** XRD patterns of CdS and $Mo_2C$/CdS (a). UV-vis-NIR DRS of CdS, $Mo_2C$, and $Mo_2C$/CdS (b).

XPS measurement was carried out to analyze the surface composition, bonding states, and interaction between CdS and $Mo_2C$ in $Mo_2C$/CdS as shown in Fig. 5. From the survey spectrum (Fig. 5a), elements of Cd, S, Mo, C, and O are clearly identified in $Mo_2C$/CdS. Fig. 5b, C, and D show the XPS spectra of Cd 3d, S 2p, and Mo 3d, respectively. For bare CdS, two peaks at binding energies of 413.1 and 406.3 eV correspond to Cd $3d_{3/2}$ and Cd $3d_{5/2}$, respectively,[40] which are the characteristic peaks of $Cd^{2+}$ in CdS. Fig. 5c shows the XPS spectrum of S 2p region, where the peaks centered at 164.0 and 162.9 eV are assigned to S $2p_{1/2}$ and S $2p_{3/2}$, respectively.[41] Upon the hybridization of CdS and $Mo_2C$, the binding energy of Cd 3d shifts to a slightly positive direction that indicates a strong interaction between CdS and $Mo_2C$.[42] In Fig. 5d, the peak at binding energy of 227.9 eV corresponds to the Mo $3d_{5/2}$ of $Mo^{2+}$ of Mo-C in $Mo_2C$.[39] The binding energy of Mo $3d_{5/2}$ in $Mo_2C$/CdS shifted to lower energy, suggesting the interactions between CdS and $Mo_2C$.[43] The intimate contact between CdS and $Mo_2C$ facilitates the transfer of photogenerated electrons from CdS to $Mo_2C$ upon Vis light irradiation. In addition, the peak located at 234.5 eV is assigned to $Mo^{5+}$, probably due to the passivating treatment of commercial $Mo_2C$.[38] It should be noted that the peaks due to $Mo^{4+}$ and $Mo^{6+}$ of Mo-O in inactive $MoO_2$ and $MoO_3$, which have been often reported in the previous works,[39, 44] were not detected in the present work. This implies that $Mo_2C$ were uncontaminated.

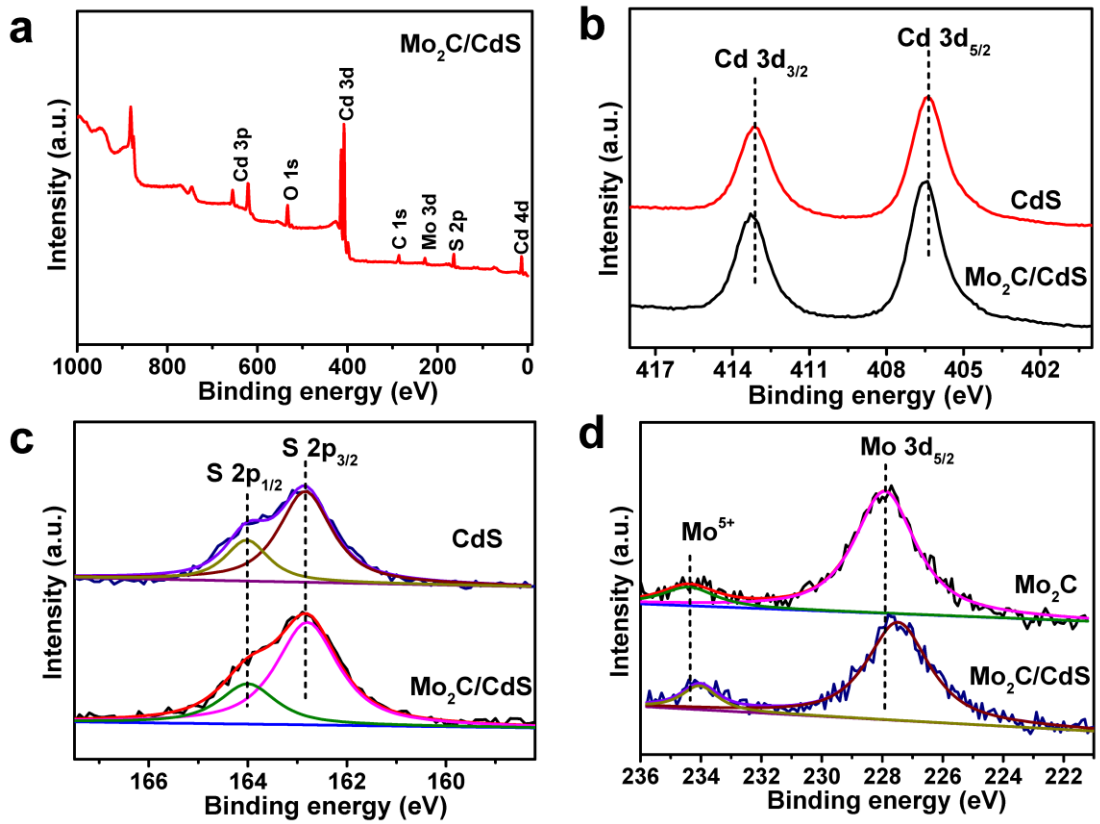


**Figure 5.** XPS spectra of CdS and $Mo_2C$/CdS: full survey (a), Cd 3d (b), S 2p (c), and Mo 3d (d).

To evaluate the photocatalytic activity of the samples, photocatalytic HER was examined by using a Xenon lamp with a 420 nm long-pass filter in the presence of lactic acid (LA) as a sacrificial reagent (Fig. 6a). As shown in Fig. 7a, only 0.47 mmol $g^{-1}$ $h^{-1}$ of $H_2$ production was detected for bare CdS mainly due to the rapid recombination of photogenerated electron-hole pairs. Bare $Mo_2C$ showed no activity for HER under the same conditions, suggesting that $Mo_2C$ merely acts as a cocatalyst for proton reduction, rather than a photocatalyst. For the comparison, bulk $Mo_2C$ hybridized on CdS was also prepared and it exhibited the photocatalytic HER rate of 1.3 mmol $g^{-1}$ $h^{-1}$ as shown in Fig. 6b. Notably, when $Mo_2C$ as a cocatalyst was hybridized on CdS, the photocatalytic HER activity was 7.7 mmol $g^{-1}$ $h^{-1}$, which is 6- and 16-folds as high as those for bulk $Mo_2C$/CdS and bare CdS, respectively. The improved activity can be ascribed to an efficient separation of the photogenerated electron-hole pairs, shortened charge diffusion distance, and more exposed active sites of $Mo_2C$ than bulk $Mo_2C$. The optimal mass ratio of $Mo_2C$ was estimated to be 3 wt%. As shown in Fig. 7b, an increase in the mass ratio of $Mo_2C$ from 0 to 3 wt% significantly improved the amount of $H_2$ production to reach the maximum value. However, further increase in the mass ratio of

$Mo_2C$ to 5 wt% results in the suppression of $H_2$ production, which is probably due to the light-screening effect and/or structural factors caused by the presence of excessive cocatalyst such as aggregations. To further validate the critical role of $Mo_2C$ in 3 wt% $Mo_2C$/CdS, 3 wt% Pt/CdS was also prepared and applied to the photocatalytic HER. Fig. 7a reveals that $Mo_2C$/CdS showed 4-fold increase compared with Pt/CdS, suggesting excellent cocatalyst property of $Mo_2C$ probably due to its sheet structure. $Mo_2C$/CdS synthesized by ultrasonic mixing in DMF solvent showed lower activity owing to the fact that contact between $Mo_2C$ and CdS was not sufficient as shown in Fig. 8a and b. It is suggested that in situ growth of CdS on $Mo_2C$ makes close contact to enhance the ET from CdS to $Mo_2C$.

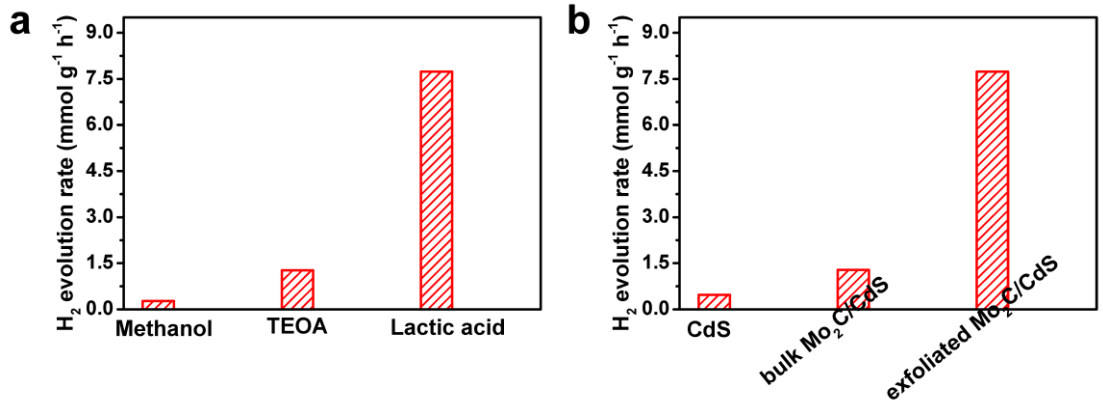


**Figure 6.** Effect of sacrificial reagents on photocatalytic $H_2$ evolution for 3 wt% $Mo_2C$/CdS (a). Comparison of the photocatalytic HER activities of CdS-based photocatalysts (b).

The photocatalytic stability of $Mo_2C$/CdS was investigated by a cycle experiment as shown in Fig. 9a. There is no noticeable decrease in photocatalytic HER activity after four cycles. The structure of $Mo_2C$/CdS after the cycle experiment was characterized by XRD as shown in Fig. 9b. There was no obvious change which indicates good stability of $Mo_2C$/CdS. The AQE of photocatalytic HER was measured at several wavelengths using monochromatic light under the optimal conditions. As shown in Fig. 7c, the AQE value was consistent with the DRS of CdS. Remarkably, the AQE of 3 wt% $Mo_2C$/CdS is 86% at 460 nm which is much higher than those of other CdS-based photocatalysts for HER activity as summarized in Table 1.

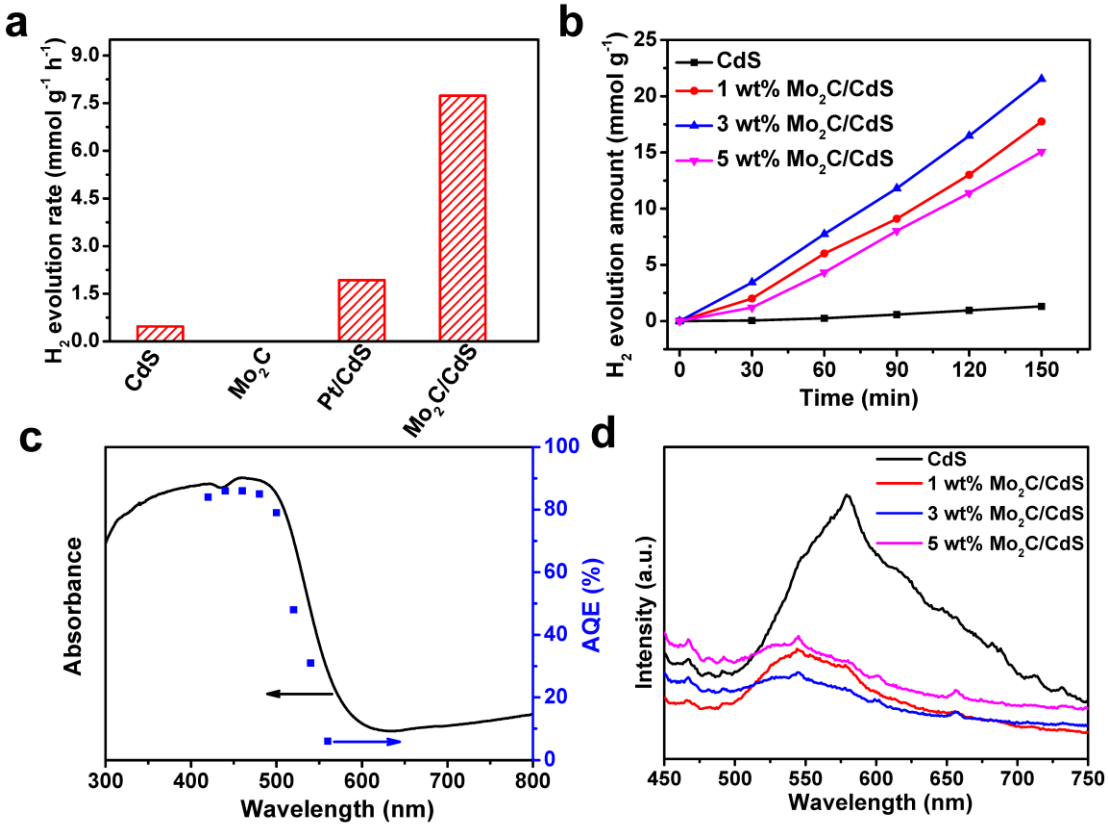


**Figure 7.** Comparison of the photocatalytic HER activities of CdS-based photocatalysts (a). Time-dependent photocatalytic HER of CdS and $Mo_2C$/CdS with different ratios of $Mo_2C$ under Vis light irradiation using LA as a sacrificial reagent (b). DRS (left axis) and AQE (right axis) of 3 wt% $Mo_2C$/CdS (c). Photoluminescence spectra of CdS and $Mo_2C$/CdS (d).

**Table 1.** Comparison of CdS-based photocatalysts for photocatalytic $H_2$ evolution.

| Photocatalyst | Sacrificial reagent | Light source, wavelength (nm) | Rate (mmol $g^{-1}$ $h^{-1}$) | AQE, excitation wavelength | Ref. |
|---|---|---|---|---|---|
| $MoS_2$/Graphene/ CdS | $NaS_2$-$Na_2SO_3$ | Xe lamp, λ ≥ 420 | 9.0 | 28.1%, 420 nm | 45 |
| Au/CdS/Pt | $NaS_2$-$Na_2SO_3$ | Xe lamp, λ ≥ 420 | 11.5 | 45.6%, 420 nm | 46 |
| $WS_2$/CdS | lactic acid | Xe lamp, λ ≥ 420 | 11.4 | 67%, 420 nm | 47 |
| $WS_2$/CdS | lactic acid | Xe lamp, λ ≥ 420 | 14.1 | 70%, 460 nm | 42 |
| $Mo_2S$/CdS | lactic acid | Xe lamp, λ ≥ 420 | 49.8 | 41.4%, 420 nm | 48 |
| $Mo_2S$/CdS | lactic acid | Xe lamp, λ ≥ 420 | 21.4 | 57.2%, 420 nm | 49 |
| $Mo_2C$/CdS | lactic acid | Xe lamp, λ ≥ 420 | 7.7 | 86%, 460 nm | present work |

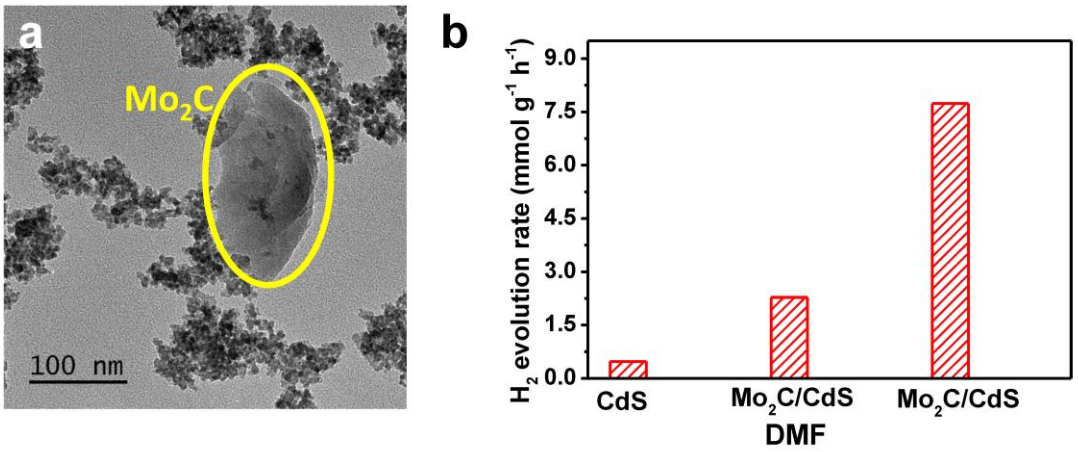


**Figure 8.** TEM images of $Mo_2C$/CdS synthesized by ultrasonic mixing in DMF solvent (a) and the comparison of photocatalytic $H_2$ evolution rate (b).

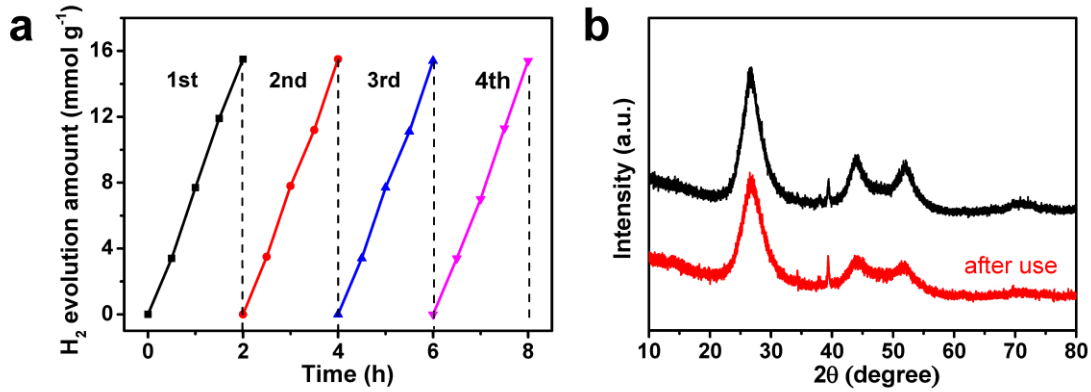


**Figure 9.** Cycle experiment of 3 wt% $Mo_2C$/CdS as a photocatalyst for $H_2$ evolution under Vis light irradiation (a). XRD patterns of 3 wt% $Mo_2C$/CdS before and after the cycle experiment (b).

PL spectra were measured to evaluate the recombination of photogenerated electron-hole pairs.[50] The PL spectra were recorded under 420 nm excitation as shown in Fig. 7d. It was found that bare CdS shows a strong emission band at 578 nm, which is attributed to the excitonic recombination. It also shows near band-edge emission in the range of 610-750 nm, which is assigned to the trap states recombination caused by the surface defects.[51] Obviously, bare CdS exhibits the highest PL intensity, demonstrating the efficient recombination of photogenerated charge carriers. It is reported that photogenerated charge carriers easily transfer to the surface defects, where electrons do not contribute to HER.[52] When CdS was hybridized with $Mo_2C$, the emission intensity decreased clearly, indicating the efficient separation of photogenerated charge carriers at the heterointerface between $Mo_2C$ and CdS in $Mo_2C$/CdS. The near band-edge emission of $Mo_2C$/CdS was quenched distinctly, suggesting an effective passivation effect for surface defect states[53, 54] which leads to efficient ET from CdS to $Mo_2C$. In addition, it was shown that the peak at 578 nm shifts to a shorter wavelength of 550 nm, demonstrating the interaction between CdS and $Mo_2C$. Similar phenomena were also reported for $MoS_2$ nanosheets/CdS and $WS_2$ nansosheets/CdS by Ye et al. [55] and Yin et al.,[56] respectively. In their works, the PL peaks of the composites shifted more distinctly with a decrease in the number of layers of the sulfides nanosheets.

To further evaluate the separation efficiency of charge carriers and interfacial charge transportation between CdS and $Mo_2C$, the photocurrent responses of CdS, $Mo_2C$/CdS and Pt/CdS were measured under Vis light irradiation. Fig. 10a shows photocurrent

responses of CdS and $Mo_2C$/CdS under 30 s Vis light irradiation through on/off cycles. When the light is on, the photogenerated electrons and holes move in the opposite directions under bias voltage, generating photocurrent density. When the light is off, this effect diminishes. The experimental results demonstrate that 3 wt% $Mo_2C$/CdS exhibits a higher transient photocurrent density than those of bare CdS and other $Mo_2C$/CdS. This result is consistent with those of PL and photocatalytic activity, suggesting the highest separation efficiency of the photogenerated electron-hole pairs for 3 wt% $Mo_2C$/CdS. Moreover, the photocurrent responses were reproducible for several on–off cycles and remained stable. The charge transfer performance in the photocatalysis can also be verified by the EIS. In the EIS spectra, faster ET generally induces a smaller semicircle arc. The equivalent circuit model for EIS plots was also built as show in the inset. In this model, $R_s$ and $R_{ct}$ represent the series resistance and the charge transfer resistance, respectively. As shown in Fig. 10b, 3 wt% $Mo_2C$/CdS shows the smallest $R_{ct}$, suggesting the efficient electron injection and fast migration under Vis light irradiation. In addition, the photocurrent response and EIS of Pt/CdS were also investigated to make a comparison with those obtained from $Mo_2C$/CdS as shown in Fig. 10c and d. $Mo_2C$/CdS shows a higher photocurrent density and a smaller arc radius than those of Pt/CdS, suggesting an enhanced electric conductivity and a decreased charge transfer resistance in $Mo_2C$/CdS than those in Pt/CdS.

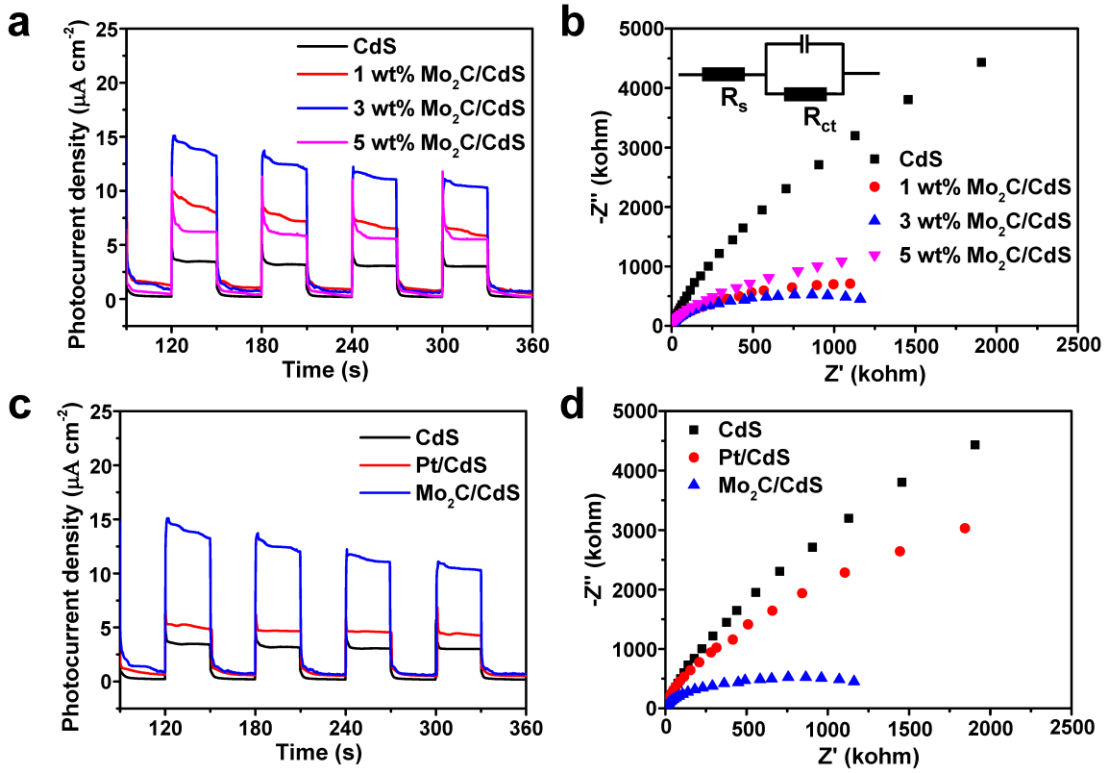


**Figure 10.** Photocurrent density curves (a) and EIS Nyquist plots (b) of CdS and $Mo_2C$/CdS under Vis light irradiation in $Na_2SO_4$ solution. The inset is the equivalent circuit model for EIS plots.

Although the photoelectrochemical experiments can validate the efficient charge transfer and PL measurements provide information on charge recombination in $Mo_2C$/CdS, the ET in photocatalysts is a critical factor for deeper understanding of the photocatalytic reactions. TDR spectroscopy has been carried out to investigate photogenerated charge carrier behaviors in photocatalysts.[57-62] The TDR spectra of all CdS-based photocatalysts were recorded at various time delays after a 420 nm laser pulse excitation as shown in Fig. 11. The spectra showed a broad and continuous absorption band in the range of 850–1200 nm which can be assigned to the free and trapped electrons in photocatalysts.[63, 64] The transient absorptions of all samples reached the maximum intensity immediately after the laser pulse and then decayed gradually. It is obvious that the signals of $Mo_2C$/CdS decreased more rapidly than those of bare CdS, particularly from 2 to 10 ps, and 3 wt% $Mo_2C$/CdS exhibited the fastest decrease (Fig. 12a).

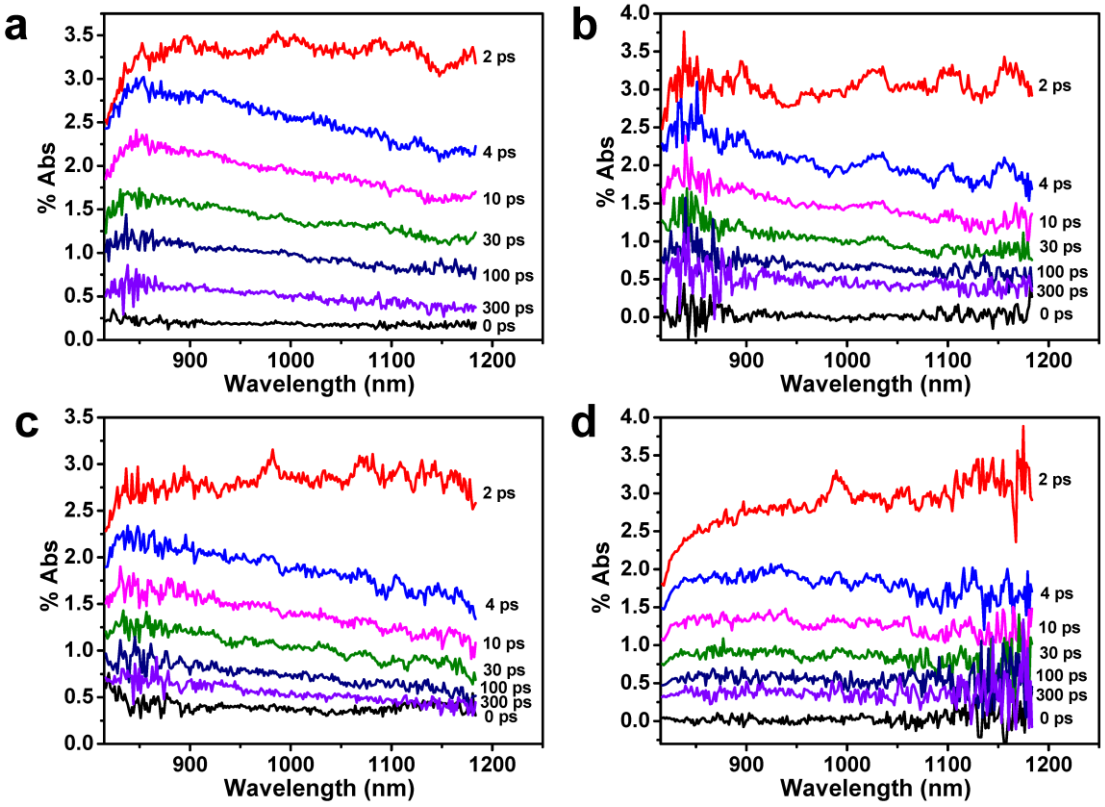


**Figure 11.** Time-resolved diffuse reflectance (TDR) spectra observed during 420 nm femtosecond laser flash photolysis of CdS (a), 1 wt% $Mo_2C$/CdS (b), 3 wt% $Mo_2C$/CdS (c), and 5 wt% $Mo_2C$/CdS (d).

The charge recombination in semiconductor photocatalyst includes radiative and nonradiative band edge electron-hole recombination as represented in Fig. 12b.[65] After the initial photoexcitation, photogenerated electrons in the conduction band of CdS could be trapped to be used for HER, although the efficiency is low because of the rapid charge recombination. The decays of exciton relaxation due to the charge recombination and trapping processes are usually analyzed by multi-decay functions.[65, 66] To elucidate the kinetics of ET, the time profiles of the transient absorption at 1000 nm for CdS-based photocatalysts were fitted using two-exponential functions (lifetimes: $\tau_1$ and $\tau_2$) and a long-lived component (i.e. constant, Fig. 12a), and their lifetimes are summarized in Table 1. For bare CdS, the decay profile was fitted with two decay lifetimes of $\tau_1$ = 6.4 ps (71%) and $\tau_2$ = 214 ps (29%). The short lifetime $\tau_1$ of CdS represents mainly the trapping process of electrons by a shallow trap state ($\tau_1 = 1/k_{ST}$, $k_{ST}$: trapping rate by shallow trap), while the long lifetime $\tau_2$ represents the relaxation of electrons into a deep trap state ($\tau_2 = 1/k_{DT}$, $k_{DT}$: trapping rate by deep trap), when radiative and ET processes from CdS for $H_2$ production are negligible (Fig. 12b). For

$Mo_2C$/CdS, $\tau_1$ and $\tau_2$ are shorter than those of bare CdS, indicating the existence of fast ET from CdS to $Mo_2C$ as expressed by following equation: $\tau_1 = 1/k_{ST} + 1/ k_{ETCB}$ and $\tau_2 = 1/k_{DT} + 1/k_{ETST}$ ($k_{ETCB}$ and $k_{ETST}$: ET rates from conduction band and shallow trap of CdS to $Mo_2C$, respectively). The average decay lifetimes of $\tau_1$ and $\tau_2$ of $Mo_2C$/CdS also decreased compared with that of bare CdS ($\tau_{av}$ = 66.6 ps), supporting the existence of ET.[67] Photogenerated electrons transferred by the ET processes are to be used for the subsequent proton reduction. Notably, the $\tau_1$, $\tau_2$, and $\tau_{av}$ values of 3 wt% $Mo_2C$/CdS are shorter than the corresponding values of 1 wt%- and 5 wt% $Mo_2C$/CdS, indicating that 3 wt% $Mo_2C$/CdS exhibits the fastest ET and more efficient electron injection from CdS to $Mo_2C$, which agrees with the fact that 3 wt% $Mo_2C$/CdS exhibits the highest HER activity. Excess amount of $Mo_2C$ in 5 wt% $Mo_2C$/CdS decelerates the ET rate probably due to the structural factor suggested before.

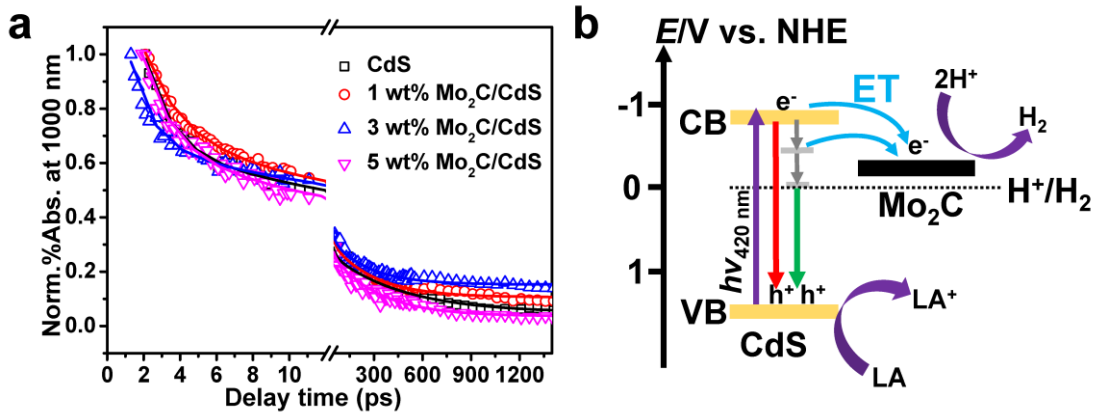


**Figure 12.** Time profiles of normalized transient absorption at 1000 nm of $Mo_2C$/CdS (a) and schematic illustration of photogenerated ET in $Mo_2C$/CdS (b).

In addition, the decay kinetics of photogenerated electrons in 3 wt% Pt/CdS and 3 wt% bulk $Mo_2C$/CdS were also measured as displayed in Fig. 13 and decay lifetimes are summarized in Table 2. The lifetimes of 3 wt% $Mo_2C$/CdS are shorter than those of 3 wt% bulk $Mo_2C$/CdS, indicating that ET in 3 wt% $Mo_2C$/CdS is faster due to strong interaction between CdS and $Mo_2C$ at heterointerface. Furthermore, the decay lifetimes of 3 wt% $Mo_2C$/CdS are shorter than those of 3 wt% Pt/CdS, suggesting that $Mo_2C$ is more effective as a cocatalyst than Pt supporting better heterointerface between $Mo_2C$ and CdS indicated above.

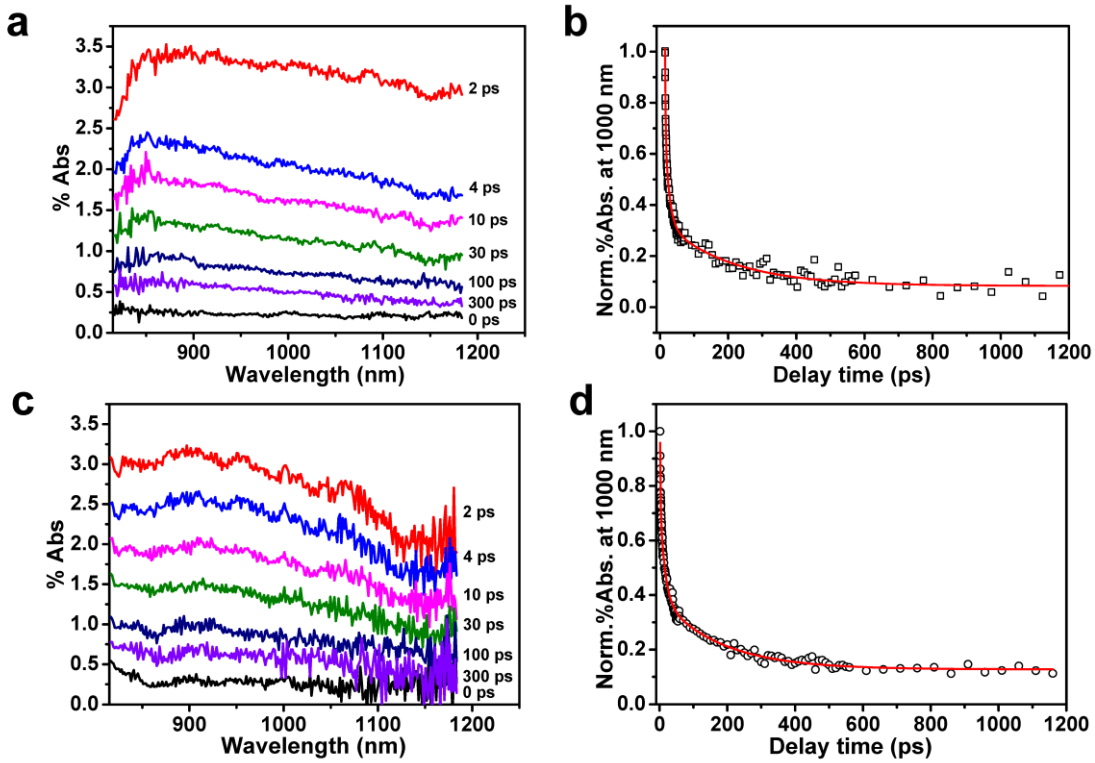


**Figure 13.** Time-resolved diffuse reflectance (TDR) spectra for 3 wt% Pt/CdS (a) and 3 wt% bulk $Mo_2C$/CdS (c). Time profiles of normalized transient absorption at 1000 nm of 3 wt% Pt/CdS (b) and 3 wt% bulk $Mo_2C$/CdS (d).

**Table 2** Lifetimes of TDR decays for CdS-based photocatalysts.

| sample | $\tau_1$ [a] (ps) | $\tau_2$ [a] (ps) | $\tau_{av}$ [b] (ps) |
|---|---|---|---|
| CdS | 6.4 (71%) | 214 (29%) | 66.6 |
| 1 wt% $Mo_2C$/CdS | 5.7 (73%) | 126 (27%) | 38.2 |
| 3 wt% $Mo_2C$/CdS | 2.4 (60%) | 54.3 (40%) | 23.2 |
| 5 wt% $Mo_2C$/CdS | 5.1 (71%) | 156 (29%) | 48.9 |
| 3 wt% Pt/CdS | 5.8 (70%) | 169 (30%) | 54.7 |
| 3 wt% bulk $Mo_2C$/CdS | 5.3 (63%) | 152 (37%) | 59.5 |

[a] $\tau_1$ and $\tau_2$ are the lifetimes of initial two decay components. [b] $\tau_{av}$ is the averaged lifetime of $\tau_1$ and $\tau_2$.

Based on the above experimental results and analysis, the possible mechanism of photocatalytic HER for $Mo_2C$/CdS is illustrated in Fig. 12b. Bare CdS shows low photocatalytic activity due to the fast recombination of photogenerated electron-hole pairs. For $Mo_2C$/CdS, $Mo_2C$ exhibits photocatalytic HER. Upon excitation, photogenerated electrons in the conduction band and shallow trap states of CdS rapidly

transfer to $Mo_2C$ before the charge recombination. Owing to the successful exfoliation from 3D particles to 2D nanosheets, $Mo_2C$ exposes more active sites and meanwhile provides a shorter distance for the injected electrons transferring to the surface active sites, leading to efficient photocatalytic HER. Holes in the valence band are consumed by LA as a sacrificial electron donor.

# 4. Conclusion

In summary, $Mo_2C$, 2D MXenes, was successfully obtained by liquid-phase ultrasonic exfoliation to work as a low-cost high-performance cocatalyst hybridized on CdS ($Mo_2C$/CdS) for efficient photocatalytic HER under Vis light irradiation. $Mo_2C$/CdS exhibited the HER activity of 7.7 mmol $g^{-1}$ $h^{-1}$, which is 6-, 16-, and 4-folds as high as those for bulk $Mo_2C$/CdS, bare CdS, and Pt/CdS, respectively. The AQE value of 3 wt% $Mo_2C$/CdS is 86% at 460 nm. $Mo_2C$ enhances the ET from CdS to $Mo_2C$ for efficient separation of the photogenerated charge carriers, facilitates charge transfer in a shortened distance, and exposes more active sites than bulk $Mo_2C$, leading to efficient photocatalytic HER. Consequently, the work presented here shows that $Mo_2C$ has a great potential as a cocatalyst for photocatalytic HER under Vis light irradiation, and that the liquid-phase ultrasonic exfoliation is a feasible method for transforming bulk materials to nanosheets.

# 5. References


1. T. Hisatomi, J. Kubota and K. Domen, *Chem. Soc. Rev.*, 2014, **43**, 7520-7535.
2. S. J. A. Moniz, S. A. Shevlin, D. J. Martin, Z. X. Guo and J. Tang, *Energy Environ. Sci.*, 2015, **8**, 731-759.
3. X. Li, J. Yu, J. Low, Y. Fang, J. Xiao and X. Chen, *J. Mater. Chem. A*, 2015, **3**, 2485-2534.
4. Y. J. Yuan, D. Chen, Z. T. Yu and Z. G. Zou, *J. Mater. Chem. A*, 2018, **6**, 11606-11630.
5. L. Cheng, Q. Xiang, Y. Liao and H. Zhang, *Energy Environ. Sci.*, 2018, **11**, 1362-1391.
6. S. T. Kochuveedu, Y. H. Jang and D. H. Kim, *Chem. Soc. Rev.*, 2013, **42**, 8467-8493.
7. J. Ran, J. Zhang, J. Yu, M. Jaroniec and S. Z. Qiao, *Chem. Soc. Rev.*, 2014, **43**,

7787-7812.

8. D. V. Esposito, S. T. Hunt, Y. C. Kimmel and J. G. Chen, *J. Am. Chem. Soc.*, 2012, **134**, 3025-3033.
9. T. F. Jaramillo, K. P. Jørgensen, J. Bonde, J. H. Nielsen, S. Horch and I. Chorkendorff, *Science*, 2007, **317**, 100-102.
10. Y. Shi and B. Zhang, *Chem. Soc. Rev.*, 2016, **45**, 1529-1541.
11. M. Naguib, M. Kurtoglu, V. Presser, J. Lu, J. Niu, M. Heon, L. Hultman, Y. Gogotsi and M. W. Barsoum, *Adv. Mater.*, 2011, **23**, 4248-4253.
12. M. Naguib, V. N. Mochalin, M. W. Barsoum and Y. Gogotsi, *Adv. Mater.*, 2014, **26**, 992-1005.
13. M. Naguib, O. Mashtalir, J. Carle, V. Presser, J. Lu, L. Hultman, Y. Gogotsi and M. W. Barsoum, *ACS Nano*, 2012, **6**, 1322-1331.
14. B. Anasori, M. R. Lukatskaya and Y. Gogotsi, *Nat. Rev. Mater.*, 2017, **2**.
15. M. Khazaei, M. Arai, T. Sasaki, C. Y. Chung, N. S. Venkataramanan, M. Estili, Y. Sakka and Y. Kawazoe, *Adv. Funct. Mater.*, 2013, **23**, 2185-2192.
16. B. Ma, J. Zhang, K. Lin, D. Li, Y. Liu and X. Yang, *ACS Sustain. Chem. Eng.*, 2019, **7**, 13569-13575.
17. B. Ma, D. Li, X. Wang and K. Lin, *ChemSusChem*, 2018, **11**, 3871-3881.
18. B. Ma, X. Li, D. Li and K. Lin, *Appl. Catal. B: Environ.*, 2019, **256**, 117865.
19. R. Michalsky, Y.-J. Zhang and A. A. Peterson, *ACS Catal.*, 2014, **4**, 1274-1278.
20. C. Lu, D. Tranca, J. Zhang, F. N. Rodri Guez Hernandez, Y. Su, X. Zhuang, F. Zhang, G. Seifert and X. Feng, *ACS Nano*, 2017, **11**, 3933-3942.
21. S. Wang, J. Wang, M. Zhu, X. Bao, B. Xiao, D. Su, H. Li and Y. Wang, *J. Am. Chem. Soc.*, 2015, **137**, 15753-15759.
22. Y. Huang, Q. Gong, X. Song, K. Feng, K. Nie, F. Zhao, Y. Wang, M. Zeng, J. Zhong and Y. Li, *ACS Nano*, 2016, **10**, 11337-11343.
23. F. X. Ma, H. B. Wu, B. Y. Xia, C. Y. Xu and X. W. Lou, *Angew. Chem. Int. Ed.*, 2015, **54**, 15395-15399.
24. L. Liao, S. Wang, J. Xiao, X. Bian, Y. Zhang, M. D. Scanlon, X. Hu, Y. Tang, B. Liu and H. H. Girault, *Energy Environ. Sci.*, 2014, **7**, 387-392.
25. Z. W. Seh, K. D. Fredrickson, B. Anasori, J. Kibsgaard, A. L. Strickler, M. R. Lukatskaya, Y. Gogotsi, T. F. Jaramillo and A. Vojvodic, *ACS Energy Lett.*, 2016, **1**, 589-594.

26. X. Li, W. Cai, J. An, S. Kim, J. Nah, D. Yang, R. Piner, A. Velamakanni, I. Jung, E. Tutuc, S. K. Banerjee, L. Colombo and R. S. Ruoff, *Science*, 2009, **324**, 1312-1314.
27. X. Hai, W. Zhou, K. Chang, H. Pang, H. Liu, L. Shi, F. Ichihara and J. Ye, *J. Mater. Chem. A*, 2017, **5**, 8591-8598.
28. L. Yin, X. Hai, K. Chang, F. Ichihara and J. Ye, *Small*, 2018, **14**, e1704153.
29. M. A. Lukowski, A. S. Daniel, F. Meng, A. Forticaux, L. Li and S. Jin, *J. Am. Chem. Soc.*, 2013, **135**, 10274-10277.
30. D. Voiry, H. Yamaguchi, J. Li, R. Silva, D. C. Alves, T. Fujita, M. Chen, T. Asefa, V. B. Shenoy, G. Eda and M. Chhowalla, *Nat. Mater.*, 2013, **12**, 850-855.
31. Y. Sun, Z. Sun, S. Gao, H. Cheng, Q. Liu, J. Piao, T. Yao, C. Wu, S. Hu, S. Wei and Y. Xie, *Nat. Commun.*, 2012, **3**, 1057.
32. J. N. Coleman, M. Lotya, A. O'Neill, S. D. Bergin, P. J. King, U. Khan, K. Young, A. Gaucher, S. De, R. J. Smith, I. V. Shvets, S. K. Arora, G. Stanton, H.-Y. Kim, K. Lee, G. T. Kim, G. S. Duesberg, T. Hallam, J. J. Boland, J. J. Wang, J. F. Donegan, J. C. Grunlan, G. Moriarty, A. Shmeliov, R. J. Nicholls, J. M. Perkins, E. M. Grieveson, K. Theuwissen, D. W. McComb, P. D. Nellist and V. Nicolosi, *Science*, 2011, **331**, 568-571.
33. X. Fan, P. Xu, Y. C. Li, D. Zhou, Y. Sun, M. A. Nguyen, M. Terrones and T. E. Mallouk, *J. Am. Chem. Soc.*, 2016, **138**, 5143-5149.
34. J. Jia, T. Xiong, L. Zhao, F. Wang, H. Liu, R. Hu, J. Zhou, W. Zhou and S. Chen, *ACS Nano*, 2017, **11**, 12509-12518.
35. L. C. A. Oliveira, H. S. Oliveira, G. Mayrink, H. S. Mansur, A. A. P. Mansur and R. L. Moreira, *Appl. Catal. B: Environ.* 2014, **152-153**, 403-412.
36. N. S. Alhajri, D. H. Anjum and K. Takanabe, *J. Mater. Chem. A*, 2014, **2**, 10548-10556.
37. H. Wang, H. Ye, B. Zhang, F. Zhao and B. Zeng, *J. Mater. Chem. A*, 2017, **5**, 10599-10608.
38. X. Yue, S. Yi, R. Wang, Z. Zhang and S. Qiu, *Nano Energy*, 2018, **47**, 463-473.
39. X. Yue, S. Yi, R. Wang, Z. Zhang and S. Qiu, *J. Mater. Chem. A*, 2017, **5**, 10591-10598.
40. R. Cheng, Y. Wen, L. Yin, F. Wang, F. Wang, K. Liu, T. A. Shifa, J. Li, C. Jiang, Z. Wang and J. He, *Adv. Mater.*, 2017, **29**.
41. F. Ma, G. Zhao, C. Li, T. Wang, Y. Wu, J. Lv, Y. Zhong and X. Hao,

*CrystEngComm*, 2016, **18**, 631-637.

42. K. Zhang, M. Fujitsuka, Y. Du and T. Majima, *ACS Appl. Mater. Interfaces*, 2018, **10**, 20458-20466.
43. Y. Yang, Y. Zhang, Z. Fang, L. Zhang, Z. Zheng, Z. Wang, W. Feng, S. Weng, S. Zhang and P. Liu, *ACS Appl. Mater. Interfaces*, 2017, **9**, 6950-6958.
44. Y. X. Pan, J. B. Peng, S. Xin, Y. You, Y. L. Men, F. Zhang, M. Y. Duan, Y. Cui, Z. Q. Sun and J. Song, *ACS Sustain. Chem. Eng.*, 2017, **5**, 5449-5456.
45. K. Chang, Z. Mei, T. Wang, Q. Kang, S. Ouyang and J. Ye, *ACS Nano*, 2014, **8**, 7078-7087.
46. G. Yu, X. Wang, J. Cao, S. Wu, W. Yan and G. Liu, *Chem. Commun.*, 2016, **52**, 2394-2397.
47. D. Xu, P. Xu, Y. Zhu, W. Peng, Y. Li, G. Zhang, F. Zhang, T. E. Mallouk and X. Fan, *ACS Appl. Mater. Interfaces*, 2018, **10**, 2810-2818.
48. X. L. Yin, L. L. Li, W. J. Jiang, Y. Zhang, X. Zhang, L. J. Wan and J. S. Hu, *ACS Appl. Mater. Interfaces*, 2016, **8**, 15258-15266.
49. X. Hai, K. Chang, H. Pang, M. Li, P. Li, H. Liu, L. Shi and J. Ye, *J. Am. Chem. Soc.*, 2016, **138**, 14962-14969.
50. X. Wang, Z. Feng, J. Shi, G. Jia, S. Shen, J. Zhou and C. Li, *Phys. Chem. Chem. Phys.*, 2010, **12**, 7083-7090.
51. D. P. Kumar, S. Hong, D. A. Reddy and T. K. Kim, *J. Mater. Chem. A*, 2016, **4**, 18551-18558.
52. D. Kong, H. Wang, J. J. Cha, M. Pasta, K. J. Koski, J. Yao and Y. Cui, *Nano Lett.*, 2013, **13**, 1341-1347.
53. S. Liu, M. Q. Yang, Z. R. Tang and Y. J. Xu, *Nanoscale*, 2014, **6**, 7193-7198.
54. P. Parkinson, H. J. Joyce, Q. Gao, H. H. Tan, X. Zhang, J. Zou, C. Jagadish, L. M. Herz and M. B. Johnston, *Nano Lett*, 2009, **9**, 3349-3353.
55. K. Chang, M. Li, T. Wang, S. Ouyang, P. Li, L. Liu and J. Ye, *Adv. Energy Mater.*, 2015, **5**, 1402279.
56. J. He, L. Chen, Z. Q. Yi, C. T. Au and S. F. Yin, *Ind. Eng. Chem. Res*, 2016, **55**, 8327-8333.
57. M. Zhu, S. Kim, L. Mao, M. Fujitsuka, J. Zhang, X. Wang and T. Majima, *J. Am. Chem. Soc.*, 2017, **139**, 13234-13242.
58. R. Godin, Y. Wang, M. A. Zwijnenburg, J. Tang and J. R. Durrant, *J. Am. Chem.*

*Soc.*, 2017, **139**, 5216-5224.

59. J. K. Utterback, A. N. Grennell, M. B. Wilker, O. M. Pearce, J. D. Eaves and G. Dukovic, *Nat. Chem.*, 2016, **8**, 1061-1066.
60. D. Ruan, S. Kim, M. Fujitsuka and T. Majima, *Appl. Catal. B: Environ.*, 2018, **238**, 638-646.
61. A. J. Cowan, C. J. Barnett, S. R. Pendlebury, M. Barroso, K. Sivula, M. Gratzel, J. R. Durrant and D. R. Klug, *J. Am. Chem. Soc.*, 2011, **133**, 10134-10140.
62. D. Ruan, J. Xue, M. Fujitsuka and T. Majima, *Chem. Commun.*, 2019, **55**, 6014-6017.
63. A. Yamakata, M. Kawaguchi, N. Nishimura, T. Minegishi, J. Kubota and K. Domen, *J. Phys. Chem. C*, 2014, **118**, 23897-23906.
64. R. B. Singh, H. Matsuzaki, Y. Suzuki, K. Seki, T. Minegishi, T. Hisatomi, K. Domen and A. Furube, *J. Am. Chem. Soc.*, 2014, **136**, 17324-17331.
65. D. A. Wheeler and J. Z. Zhang, *Adv. Mater.*, 2013, **25**, 2878-2896.
66. W. Bi, L. Zhang, Z. Sun, X. Li, T. Jin, X. Wu, Q. Zhang, Y. Luo, C. Wu and Y. Xie, *ACS Catal.*, 2016, **6**, 4253-4257.
67. P. Yu, X. Wen, Y. C. Lee, W.-C. Lee, C. C. Kang and J. Tang, *J. Phys. Chem. Lett.*, 2013, **4**, 3596-3601.

# General Conclusion

Throughout this dissertation, the photocatalytic activities of Vis to NIR light response photocatalysts have been studied. In addition, the charge transfer dynamics was thoroughly explored using single-particle confocal fluorescence microscopy and femtosecond TDR spectroscopy.

In Chapter 1, g-$C_3N_4$ with nanosheet structure was prepared by using mixture of melamine (M) and urea (U) as the precursors for the photocatalytic $H_2$ production. The use of U increased the surface area, mesoporous structure, and defects of nitrogen vacancies acting as trap states in g-$C_3N_4$. The as-obtained g-$C_3N_4$-$M_1U_2$ (1 and 2 denote the weight ratios of M and U, respectively) exhibited the photocatalytic $H_2$ production rate of 3.1 mmol $g^{-1}$ $h^{-1}$ under $\lambda \geq 400$ nm light irradiation and AQE of 74% at $\lambda = 400$ nm. Single-particle PL, originated from charge recombination of photogenerated charge carriers, showed longer lifetime of charge carriers in g-$C_3N_4$-$M_1U_2$ than that in g-$C_3N_4$-M. Femtosecond time-resolved diffuse reflectance measurement was performed to observe the photogenerated electrons trapping in g-$C_3N_4$-$M_xU_y$. The results show that the electron trapping by the defects as trap states occurs faster in g-$C_3N_4$-$M_xU_y$ than in g-$C_3N_4$-M. It is suggested that the use of U increases the defects as electron trap states, leading efficient photocatalytic $H_2$ production.

In Chapter 2, Au TNP/g-$C_3N_4$, prepared by successfully loading Au TNPs on the surface of the g-$C_3N_4$ nanosheet, shows photocatalytic $H_2$ production under NIR light ($\lambda \geq 780$ nm) irradiation. FDTD simulations confirm a stronger electromagnetic field in Au TNP/g-$C_3N_4$ than in Au TNPs, which would increase the density of plasmon-induced hot electrons and facilitate interfacial ET from Au TNPs to g-$C_3N_4$ which are responsible for efficient plasmon-induced photocatalytic $H_2$ generation. TA measurements revealed plasmon-induced hot ET from Au TNPs to g-$C_3N_4$.

In Chapter 3, highly exfoliated 2D $Mo_2C$ nanosheets with a thickness of 20 nm were prepared by liquid-phase ultrasonic exfoliation for the first time. As a photocatalyst free of noble metals, $Mo_2C$ was hybridized on CdS nanoparticles with a diameter of 10 nm to be the composite $Mo_2C$/CdS, which was used for photocatalytic $H_2$ production under Vis light irradiation. Under optimized experimental conditions, $Mo_2C$/CdS exhibits a remarkable $H_2$ production rate of 7.7 mmol $g^{-1}$ $h^{-1}$ which is 6-, 16-, and 4-folds as high as those for bulk $Mo_2C$/CdS, pure CdS, and Pt/CdS,

respectively. The AQE of 3 wt% $Mo_2C$/CdS is 86% at 460 nm. The significantly enhanced activity is attributed to the rapid transfer of photogenerated electrons from CdS to $Mo_2C$ at the heterointerface and shortened migration distance of the electrons to the active sites in $Mo_2C$ as well as the presence of more active sites of $Mo_2C$ than bulk $Mo_2C$. Photoluminescence, photoelectrochemical measurements, and femtosecond time-resolved diffuse reflectance spectroscopy results demonstrated the efficient charge separation and rapid electron transport in $Mo_2C$/CdS.

To conclude, this thesis introduced three kinds of photocatalysts that can harvest Vis or NIR light for $H_2$ production. The work in Chapter 1 developed a new strategy, a-template-free method, for the synthesis of defects rich g-$C_3N_4$ with high surface area for Vis-light-driven $H_2$ production. The work in Chapter 2 realized NIR-light-response for $H_2$ production due to the utilization of SPR effect of Au nanostructures. The work in Chapter 3 explored the cost-effective cocatalyst for $H_2$ production and found that the $Mo_2C$ nanosheets show high activity than that of noble metal Pt due to the fast electron trapping processes. In each case, information on charge carrier dynamics in photocatalysts as well as morphology information provided deep understanding of the mechanisms in photocatalysis and will facilitate further design of active photocatalysts.

# List of Publications

1. Daming Ruan, Sooyeon Kim, Mamoru Fujitsuka, and Tetsuro Majima, Defects rich g-$C_3N_4$ with mesoporous structure for efficient photocatalytic $H_2$ production under visible light irradiation. *Applied Catalysis B: Environmental*, **2018**, 238, 638-646.

2. Daming Ruan, Jiawei Xue, Mamoru Fujitsuka, and Tetsuro Majima, Ultrafast spectroscopic study of plasmon-induced hot electron transfer under NIR excitation in Au triangular nanoprism/g-$C_3N_4$ for photocatalytic $H_2$ production. *Chemical Communications*, **2019**, 55, 6014-6017.

3. Daming Ruan, Mamoru Fujitsuka, and Tetsuro Majima, Exfoliated $Mo_2C$ nanosheets hybridized on CdS with fast electron transfer for efficient photocatalytic $H_2$ production under visible light irradiation. *Applied Catalysis B: Environmental*. **2020**, 264, 118541.

# Acknowledgements

First of all, I would like to thank Professor Tetsuro Majima, one of my supervisors, for accepting me as a PhD student in Osaka University.

I would like to express my sincerest gratefulness to Associate Professor Mamoru Fujitsuka who has been my supervisor in the last two years during my PhD study for his insightful suggestions and constant encouragement both in my research and in my life. His conscientious academic spirit and modest, open-minded personality inspire me both in academic study and daily life. He gives me much help and advice during the whole processes of my paper writing and doctoral defense which makes me complete my PhD course.

I deeply appreciate Professor Akira Sugimoto, Professor Mikiji Miyata, Associate Professor Kiyohiko Kawai, and Assistant Professor Sooyeon Kim for their kind help in my research. Particularly, I am greatly indebted to Associate Professor Yasuko Osakada for helping me a lot during the three years. Furthermore, I also thank Professor Toshiyuki Kida and Professor Shigeyuki Masaoka for their suggestions and help in preparation of this thesis.

I would like to thank the members in our research group, including Dr. Zaizhu Lou, Dr. Mingshan Zhu, Dr. Zhichao Sun, Dr. Peng Zhang, Dr. Chao Lu, Dr. Ossama Elbanna, Dr. Xiaowei Shi, Dr. Aihua Yan, Dr. Jing Xu, Dr. Ke Zhang, Dr. Xiaoyan Cai, Dr. Liang Mao, Miss Jie Xu, Mr. Jiawei Xue, Mr. Bo Zhuang, Mr. Yang Zhou, Miss Xinxi Li, Miss Shuya Fan, Mr. Zeyu Fan, Mr. Zuoyue Liu, Mr. Shunichi Miyamoto, Mr. Ryohei Suzuki, Mr. Hiroki Kawakami, Miss Haruna Kubo, and Miss Sanae Tominaga for their encouragement and help in my study and life in Japan. In addition, I sincere thank China Scholarship Council (CSC) for the financial support in these three years.

Finally, I express to thank my dear parents for their endless support and encouragement during my doctoral study.

RUAN DAMING

January 2020